PHOTOPRODUCTION OF NEUTRAL PIONS FROM PROTONS AT CENTER OF MASS ANGLES OF 60°, 90° AND 120° FROM .6 TO 1.2 BEV

Thesis by

Robert Ernest Diebold

In Partial Fulfillment of the Requirements

For the Degree of

Doctor of Philosophy

California Institute of Technology

Pasadena, California

1963

ACKNOWLEDGMENTS

The experiment was supervised by Dr. Robert L. Walker. I am deeply indebted to him for his suggestions, interest, and encouragement, all of which have contributed greatly to the success of the experiment.

The interest and support of Dr. Ricardo Gomez and Mr. R. Talman during the acquisition of the 60° data is deeply appreciated. They set up and maintained the lead glass Cherenkov counter and associated electronics. Together with Dr. Walker they helped with the taking and analyzing of the data during this phase of the experiment.

The interest of Dr. R. F. Bacher is appreciated. Comments and suggestions made by the various staff members and graduate students of the laboratory are gratefully acknowledged.

The active assistance of Mr. Frank Wolverton in the accumulation of the 90° and 120° data is deeply appreciated.

The success of the majority of modern high energy experiments depends on a vast number of people and this experiment was no exception. The synchroton crew under the able supervision of Larry Loucks kept the machine in running condition and helped move experimental equipment and shielding. Earl Emery expertly maintained the liquid hydrogen target. The beam tuners kept the machine running at its best hour after hour. Al Neubieser and various staff members and graduate students kept the machine electronics in operating condition. Most of the equipment used in this experiment was designed and tested by previous graduate students with the aid of their advisors.

The financial support of the National Science Foundation in the form of predoctoral fellowships is sincerely appreciated. The partial support of the United States Atomic Energy Commission is gratefully acknowledged.

ABSTRACT

Measurements of the differential cross section for the process $\gamma + p \rightarrow \pi^{o} + p$ have been made at three pion center of mass angles: 60°, 90°, and 120°. Values were obtained at intervals of .05 Bev (incident laboratory photon energy, k) from approximately 0.6 to 1.2 Bev.

Most of the data were obtained by detecting only the recoil protons with a large, wedge-shaped, single focusing magnetic spectrometer and associated equipment. For $\theta'_{\pi^{o}} = 60°$ and $k \leq .94$ Bev the π^{o} decays were also required, the decay photons being detected by a lead glass total absorption counter.

Although the experimental resolution was considerably narrower than that of most of the previous experiments, its averaging effect was still appreciable in certain regions. Using a six parameter fit, the data at each angle were unfolded in an effort to eliminate the effects of resolution and to obtain the true cross sections as a function of energy.

The results compare reasonably well with those of previous experiments once differences in resolution and systematic errors are taken into account. The results did not agree with the predictions of the Peierls resonance model. The positions and widths of the two cross section peaks in this energy region are quite similar to those observed in π^{-} p scattering.

TABLE OF CONTENTS

APPENDICES

LIST OF FIGURES

FIGURE PAGE

LIST OF TABLES

I. INTRODUCTION

The photoproduction of single pi mesons from protons has long been a fruitful source of information about the pi-nucleon interaction. The interactions between the incoming photon and the proton with its pion cloud are reasonably well understood, and the photoproduction results can thus be used to analyze the interactions between the outgoing particles.

The interactions of the initial particles in single neutral pion production are somewhat less complicated than those of charged pion production. In particular, for π^+ production the photon can interact directly with a virtual π^+ in the meson cloud of the proton. The term corresponding to this interaction gives a pole in the differential cross section at the unphysical center of mass angle, θ_π', which satisfies $\cos \theta_\pi' = 1/\beta_\pi'$ where β_π' is the center of mass meson velocity. The data of J. Boyden (1) show the effect of this term at forward pion angles. Although of intrinsic interest, the term does tend to mask the other effects.

While the π^o photoproduction matrix element does not contain such a pion exchange term (also known as the photoelectric or retardation term), it does contain exchange terms for neutral vector mesons. These terms lead to poles in the differential cross section similar to the one described above. In the region above the third resonance such terms appear to become important (2) in which case the interpretation is again made complicated.

For incident laboratory photon energies less than k = .5 Bev, the most conspicuous feature of the photoproduction data is a strong

peaking or resonance near .3 Bev (3,4). The results of elastic scattering of charged pions from protons show a similar resonance shape (5). The magnitudes of the total cross sections for the different charge states indicate that this peaking is due to a resonance in the I = 3/2, J = 3/2 state. The behavior of the total cross sections near threshold indicates $\ell = 1$ (p-wave). The angular distributions of both the scattering (6) and photoproduction (3,4) data agree with this choice.

The pi-nucleon scattering and π^o photoproduction data in the region of the resonance have been fit quite well by Gell-Mann and Watson (7) with a one-level resonance formula. The analysis of the π^+ photoproduction is complicated not only by the retardation term, but by a sizeable s-wave contribution. The retardation term interferes with the resonant term in such a way as to lower the position of the maximum by about .02 Bev from that of π^o production; the s-wave radically changes the shape of the total cross section near threshold.

The resonance has been interpreted with the dispersion theory of Chew, Goldberger, Low, and Nambu (CGLN) (8). This theory assumes that the resonance dominates the dispersion integrals. The theory does not make possible a determination of the actual location of the resonance, which must be taken from experiment, but once the (3,3) phase shift is known the s-, d-, and small p-wave phase shifts may be calculated directly.

At higher energies the π^-p total cross sections indicate two peaks with I = 1/2 (9,10), similar to peaks previously observed in photoproduction (1,11-17). Because of the success in interpreting the low

energy peaks as a resonant state with definite quantum numbers, similar interpretations of the high energy peaks have been attempted. These attempts have been limited to phenomenalogical models because the approximations made by the CGLN theory are not valid above the region of the first resonance, and no other similar theory has been presented which explains the high energy phenomena on a quantitative basis.

A. Phenomenalogical Models

One of the more successful of the phenomenalogical models is that of Peierls (18) who assumed that the three peaks are each the result of a definite state going through a resonance. He took the states to be $P_{3/2}$, $D_{3/2}$, and $F_{5/2}$, the first one with $I = 3/2$ and the others with $I = 1/2$; he assumed that only these three states are important for π^o photoproduction (for π^+ photoproduction he included the retardation and nucleon Born terms). His assignments satisfy a number of non-trivial conditions with regard to the photoproduction angular distributions, the total elastic cross section for $\pi^- p$ scattering (10), and the polarization of the recoil proton in π^o photoproduction (19). In a more detailed analysis Maloy (19) also included a small amount of non resonant s-wave in the π^o photoproduction matrix element.

Such models have been unable to fit the data in a quantitative fashion, but are only able to indicate the qualitative features. The reasons why the models are unable to give quantitative fits fall into two general categories: 1) not enough terms are included or the wrong multipoles are being emphasized; 2) the systematic errors of the experiments give misleading results.

There are a great number of terms which may need to be included in the analysis of the single π^o photoproduction data. For example, the $\pi^+ p$ data (9,10) indicate a broad peak in the I = 3/2 cross section with a maximum at approximately T_π = 1.35 Bev (corresponding to k = 1.50 Bev or W = 1.92 Bev). This peak has a shoulder at $T_\pi \sim .8$ Bev ($k \sim .95$ Bev, $W \sim 1.63$ Bev) which has been interpreted by Carruthers (20) to be a $D_{3/2}$ resonance. Perhaps these states are important in the photoproduction processes. Other terms such as the nucleon Born terms (perhaps modified by Regge considerations to give reasonable amplitudes) and the vector meson pole terms may also be important.

B. Previous π^o Photoproduction Experiments

Although a large number of single π^o experiments (2,11-17) have been previously performed in the region of the second and third resonances (table 1 contains a summary of the experiments), a good understanding of the behavior of the cross section was not obtained. The experiments generally had wide resolutions and didn't agree well with one another as a result of the wide resolution and various systematic errors. Berkelman and Waggoner (15) plot the results of some of the experiments as a function of angle for several photon energies; the various points fluctuate considerably more than one would expect on a statistical basis.

There are several possible types of systematic errors which are probably present in the various data in differing amounts. At forward π^o angles the recoil proton has relatively little energy, and those experiments which detected only the recoil proton (11,13,14,15) may have had difficulty in avoiding unwanted protons which scattered in the target.

Table 1

Summary of the High Energy π^0 Photoproduction Experiments

Experiment	θ_{π^0}	k (Bev)	E_o - k (Bev)	Resolution $\frac{\Delta k}{k}$	Method of Detection
Vette (11) Caltech	32° to 147° (~ 12 angles per energy)	.49, .59, .69, .79, .94	~ .13 (.23 for the k = .49 pts.)	~ .11	Protons momentum analyzed; detected in 3-counter telescope with pulse height discrimination.
DeWire, et al. (12) Cornell	50°, 90°, 125°	.45 to 1.14 (every .10 Bev)		.9 to 2.2 (Δ k = .1)	Proton telescope plus γ-ray Cherenkov with charged particle anticoincidence. Protons not stopped for k ≥ .95.
Stein and Rogers (13) Cornell	60°, 90°, 120°	.50 to .90 (every .10 Bev)	.12	~ .13	Proton telescope with CS_2 Cherenkov counter in anti-coincidence.
Worlock (14) Caltech	51°, 72°, 92°, 114°, 137°	.6, .7, .8	.12	.06 at 51° to .21 to 137°	Proton telescope with lucite Cherenkov counter in anti-coincidence.
Berkelman and Waggoner (15) Cornell	25° to 50° (~ 5 angles per energy)	.50, .59, .70, .80, .95 (and lower)	.1 to .4	.12 to .22	Proton telescope measuring protons of several ranges simultaneously.
Cortellessa and Reale (16) Frascati	56°, 90°	.6 to .8 (8 pts. each angle)	.2 to .4 (E_o = 1.0)	.06 to .08	Proton telescope plus γ-ray Cherenkov with charged particle anticoincidence.
Deutsch, et al. (17) Frascati	90°	.62 to .81 (14 pts.)		.03	Proton telescope with spark chamber and lucite Cherenkov counter; γ-rays checked.
Talman, et al. (2) Caltech	0° to 47° (7 pts.) 0° to 57° (8) 0° to 100° (17)	.75 (also several .92 points at 1.16 50°)	.12	.15	Two large lead glass Cherenkovs to detect both decay photons; protons also detected for some 1.16 pts.
This Experiment Caltech	60° 90° 120°	.6 to 1.2 (every .05)	.10 .05 .05	.11 .07 .05	See Sections II and III.

This sort of thing could account for the large cross sections found by Vette in this region and for Berkelman and Waggoner's large fluctuations from point to point (the experiment of Talman, which detected both of the π^o decay γ-rays, tends to agree with the lower values of Berkelman and Waggoner).

At forward proton angles, where the proton has a large kinetic energy, the experiments which stop the proton in a counter telescope (12 for $k \leq .95$ Bev, 13,14,16) need large absorption corrections. The corrective factor becomes as large as 2.5 for some of the points, and a small error in the absorption cross section could be serious for these points.

The kinematics for pi pair production become more unfavorable for single π^o experiments with increasing pion angle (see fig. A11), and at backward pion angles the pi pair corrections can become large unless the bremsstrahlung end point energy, E_o, is kept close to the photon energy being studied. Since the available experimental data on multiple pion production (21,22) are statistically poor and only available for $k \leq 1.0$ Bev, the corrections are necessarily crude. Vette and Worlock assumed that pi pairs are produced in proportion to the available phase space. Under this assumption they assigned an error of 25 or 30% to their corrections; the more recent data of Chasan (22), however, indicates that the recoil protons from charged pi pair photoproduction are not distributed statistically, but rather differ from the statistical model predictions by a factor of two in some regions. The data on neutral pi pair production is even more sketchy. Worlock and Vette each did separate experiments to try to determine this contribution. The results led

Worlock to assume the pi pair cross sections to be twice those assumed by Vette. At $\theta'_{\pi^o} = 135°$ corrections of ~ 30% were made; at 147° Vette had to make a 25 to 70% correction for the various points. The corrections depend strongly on $E_o - k$ which varies greatly from point to point and experiment to experiment. This makes it not only difficult to compare different experiments, but to even get a good angular distribution from any one experiment which has to make such large and uncertain corrections. Those experiments which require at least one of the decay photons (2,12,16) are liable only to multiple π^o contamination.

The early π^o experiments at high energies had broad experimental resolutions which gave both false angular distributions (different resolution widths were used for different angles) and a misleading picture of the shapes of the resonances. Until a year or two ago it was generally thought that the second resonance was more of a broad plateau than a peak in the total cross section (15). The experiment of Cortellessa and Reale (16), using narrow resolution, obtained a rather narrow peak as has that of Deutsch, et al. (17) more recently. This experiment also gave a narrow peak, although differing considerably from that of Cortellessa and Reale.

C. Purpose and Brief Description of This Experiment

This experiment was performed in order to better determine the shape of the π^o photoproduction cross section as a function of energy. It was hoped that good values for the resonant energies and widths of the two I = 1/2 peaks would be obtained, and that the better knowledge of the energy dependence might help identify the resonant partial waves

responsible for the two peaks, if indeed the peaks are resonances. This can be done in two ways: 1) One can better separate the contribution to the differential cross section by a particular resonance from those of the nonresonant background; the angular dependence of this contribution can then be compared with that of various proposed states. 2) One can compare the effects of the interference terms between the multipoles assumed for the resonances with the data. One such effect would be the angular dependence of the position of the peaks in the differential cross section. Such observations could be used to check the relative phases and signs of the different amplitudes with those determined by polarization measurements.

For $\theta'_{\pi^o} = 60°$ and $k \leq .94$ Bev both the proton and π^o decay were detected. This was done for two reasons: 1) to determine the contamination from sources such as wide angle scattering of protons; 2) to see if the different shape of Cortellessa's curve could be the result of the photoproduction of some unknown particle. The higher momentum points were obtained by detecting only the recoil proton.

Reasonably good resolution was obtained by using a narrow momentum defining counter; nevertheless, the counting rates were found to have been affected a slight amount by the resolution, particularly at the backward proton angle. This was corrected for by assuming the cross sections to have a certain general shape; this shape was then used to "unfold" the cross section (Section V).

II. EXPERIMENTAL EQUIPMENT

A. General

The photon beam used in this experiment was obtained from the Caltech electron synchrotron which typically accelerated 3×10^9 electrons per pulse (once per second).

The experimental area is shown in Figure 1 as it was during the latter part of the experiment. The lead glass Cherenkov counter and associated shielding which were used early in the experiment are also shown. The other experiments in progress changed from time to time, altering the general appearance of the area. With possibly two exceptions, these changes did not affect this experiment. The first of these is that the position of the beam monitor was back nearly to the rear concrete wall early in the experiment; the second is that the sweeping magnet was not present during the early stages of the experiment. In both cases the net effect was to increase the background counting rates in the individual counters and thus to increase the possibility of accidental coincidences. The effect of the beam monitor position was not noticed, but electrons from the sweeping magnet did at times give false coincidences (see Appendix VI).

B. Photon Beam

Once per second electrons were accelerated in the synchrotron and then allowed to strike the radiator (31 mils of tantalum) at a radius of 3.70 meters over a period of 40 msec. This collision produced a bremsstrahlung photon beam in the direction of motion of the electrons at collision. During this dumping process the electron energy E_o was

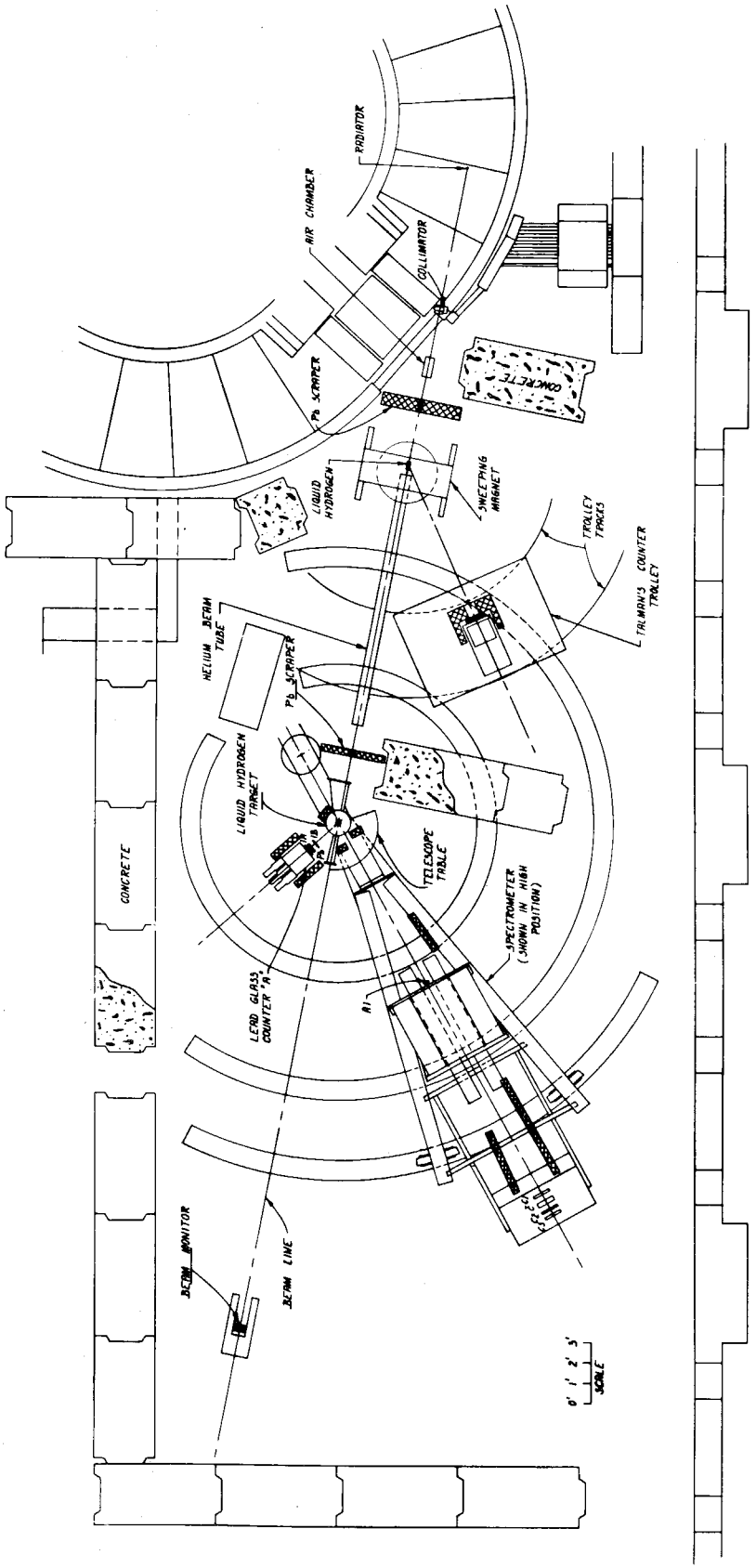

Plan View of the Experimental Area

Figure 1

held constant. The value of E_o was obtained from the radial position of the radiator and the value of magnetic field in the synchrotron at the time of collision. The latter quantity was obtained by integrating the current induced by the magnetic field of the synchrotron in a coil of wire at the radius of the radiator. The uncertainties of this determination of the field and of the exact electron orbits leads to an estimated uncertainty of .4% in E_o.

The photon beam was collimated into a rectangular shape on leaving the synchrotron; it then passed through two lead scrapers which did not further collimate the beam, but rather stopped the extraneous particles traveling close to the beam. At the position of the target used in this experiment the beam as defined by the collimator was 41 mm broad and 49 mm high. The horizontal position of the center of the beam was found to change slightly with E_o, the change being approximately 2 mm at the target position per 0.1 Bev change in E_o. The spacial distribution of the beam was measured by Boyden (23); he fitted his measurements with a complicated function which depended only on the ratio r/E_o, where r is the radial distance from the beam center at the liquid hydrogen target. This distribution is shown in Figure 2a.

The photon spectrum may be represented by

$$N(k)\,dk = \frac{U}{E_o}\,\frac{B(k,\,E_o)}{k}\,dk$$

where

$N(k)\,dk$ = the number of photons with energies lying between k and k + dk per unit quantity of beam,

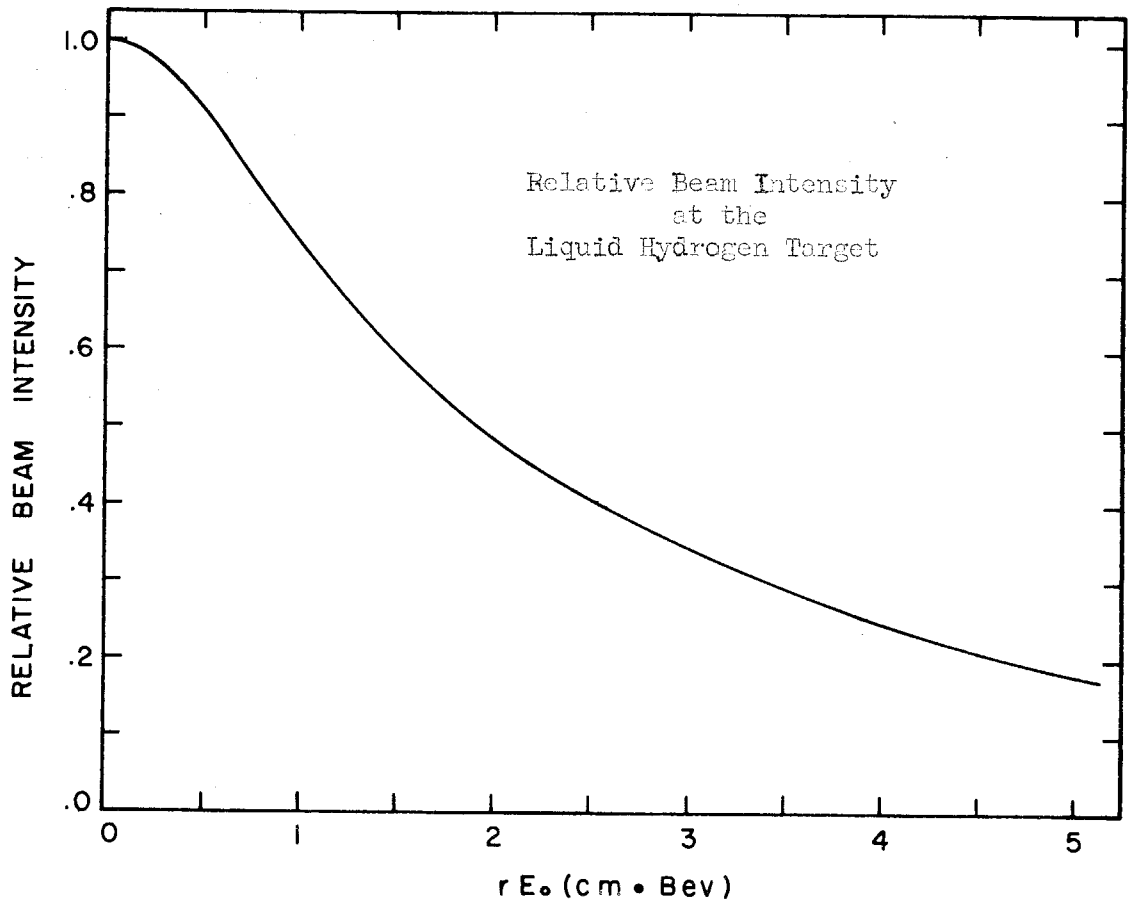
Relative Beam Intensity
at the
Liquid Hydrogen Target
RELATIVE BEAM INTENSITY
1.0
.8
.6
.4
.2
.0
0
1
2
3
4
5
r E₀ (c m • Bev)

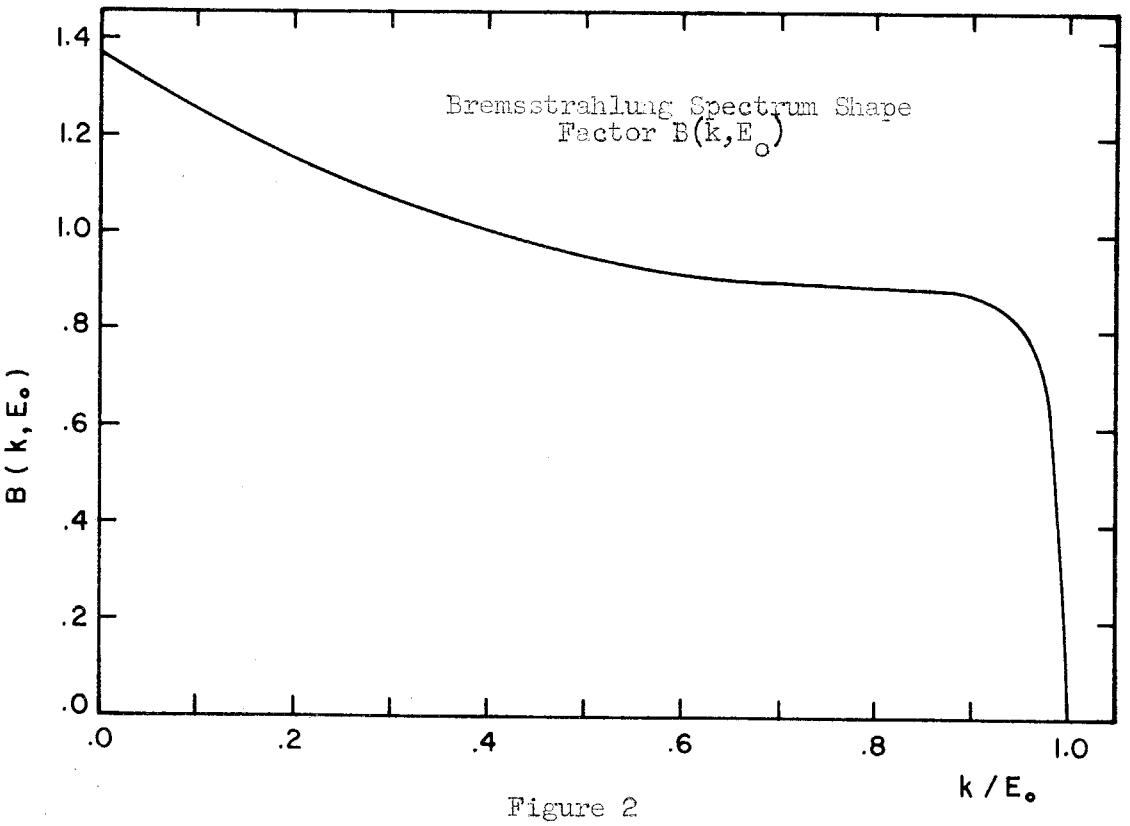
Bremsstrahlung Spectrum Shape
Factor B(k,E₀)
B (k, E₀)
1.4
1.2
1.0
.8
.6
.4
.2
.0
.0
.2
.4
.6
.8
1.0
k / E₀

Figure 2

U = the total energy in the beam per unit quantity of beam, and

$B(k,E_o)$ = the factor describing the deviation of the spectrum from a $1/k$ dependence.

Since the constant U is the total energy, B satisfies the condition:

$$\int_o^1 B(k,E_o)d(k/E_o) = 1 .$$

The factor B has been measured for $k/E_o \geq .7$ by Boyden (1) using a pair spectrometer to look at the electron pairs produced in a converter by the beam. He found B to be a function of k/E_o only and intermediate between that expected for a thin radiator and for the .2 radiation length radiator used. The results of these measurements were used in the analysis of this experiment for $k/E_o \geq .7$. For the few cases in which lower values of k were used, a parabolic shape was fitted to Boyden's curve at .7 and adjusted to satisfy the integral condition on B. The result is shown in Figure 2b.

The common unit of beam is the BIP (Beam Integrator Pulse). During this experiment a BIP was the amount of beam necessary to produce $.2106 \times 10^{-6}$ coulombs output from the beam monitor. For convenience the standard unit of beam used in the analysis was 100 BIPS, giving the dimensions of U as Bev/100 BIPS and making the integrator constant $M = .2106 \times 10^{-4}$ coulombs/100 BIPS.

The primary standard used to give an absolute value of U was a Wilson-type quantameter (24). Secondary standards were calibrated against the quantameter and used to monitor the beam during the experiment. For details see Appendix XI.

C. Liquid Hydrogen Target

The target used in this experiment is the same as that shown by Vette (11), but with certain modifications. A 1/16" thick "foghorn" shaped aluminum shield (see fig. 3) has replaced the 360° mylar window. Also the thickness of the mylar cup holding the hydrogen is 5 instead of 3 mils. The inside diameter of the mylar cup was measured at room temperature with a differential pressure of one atmosphere; a value of 7.59 cm was determined. The temperature drop from room temperature to liquid hydrogen temperature contracts the diameter by 1.3 $\pm$ .5% giving a diameter of 7.49 cm.

The liquid hydrogen in the beam was kept at a pressure 1/2 psi above atmospheric, giving a density of .0707 gm/cm^3. The background runs were taken with hydrogen gas at the same temperature and pressure; the gas had a density of .0015 gm/cm^3. A mass spectrometer analysis of the hydrogen by Petroleum Analytic Research Corporation gave the following molecular percentages:

H_2	99.89%
HD	.10
D_2	.01

Using the spacial beam distribution described earlier in this section, the average or "effective" path-length of the photons in the liquid hydrogen was calculated by a program coded by J. Boyden and modified by J. Kilner. It was found that the effective length varied from $\bar{\ell}$ = 7.13 cm for E_o = .7 Bev to 7.16 cm for 1.3 Bev. An average value of 7.15 cm was taken.

Figure 3. Experimental Equipment

3a. Spectrometer in medium energy position with the decay photon equipment. The view shows both sets of equipment at right angles to the beam line; for the 60° points, at which both sets of equipment were used, the spectrometer was 56° and the decay photon equipment 38° from the beam direction.

3b. Spectrometer in high energy position. The view shows the spectrometer at 0° with respect to the beam; in actual practice it was used at approximately 27°, 41°, and 56°.

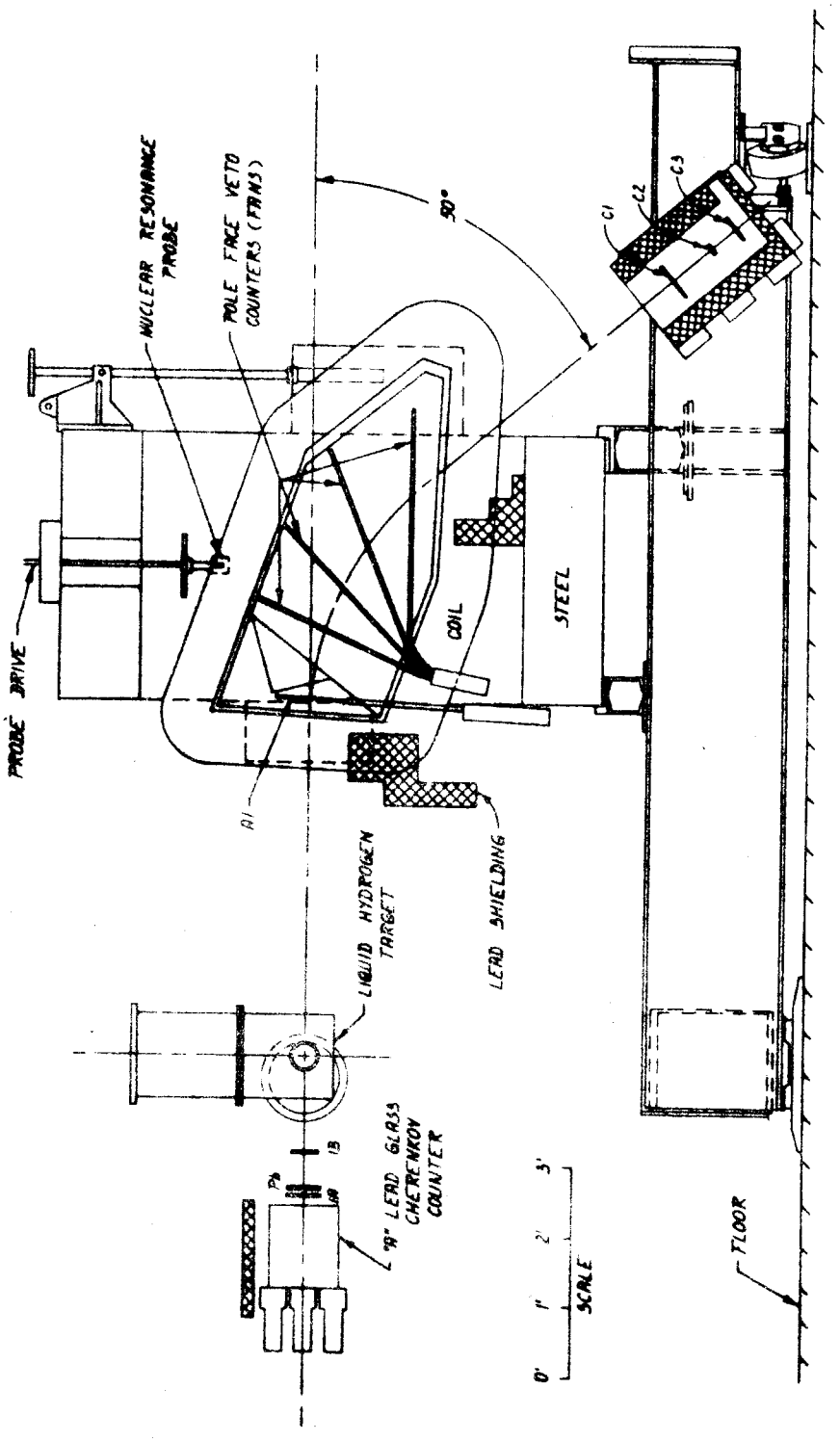

Spectrometer in Medium Energy Position with Decay Photon Equipment

Figure 3a

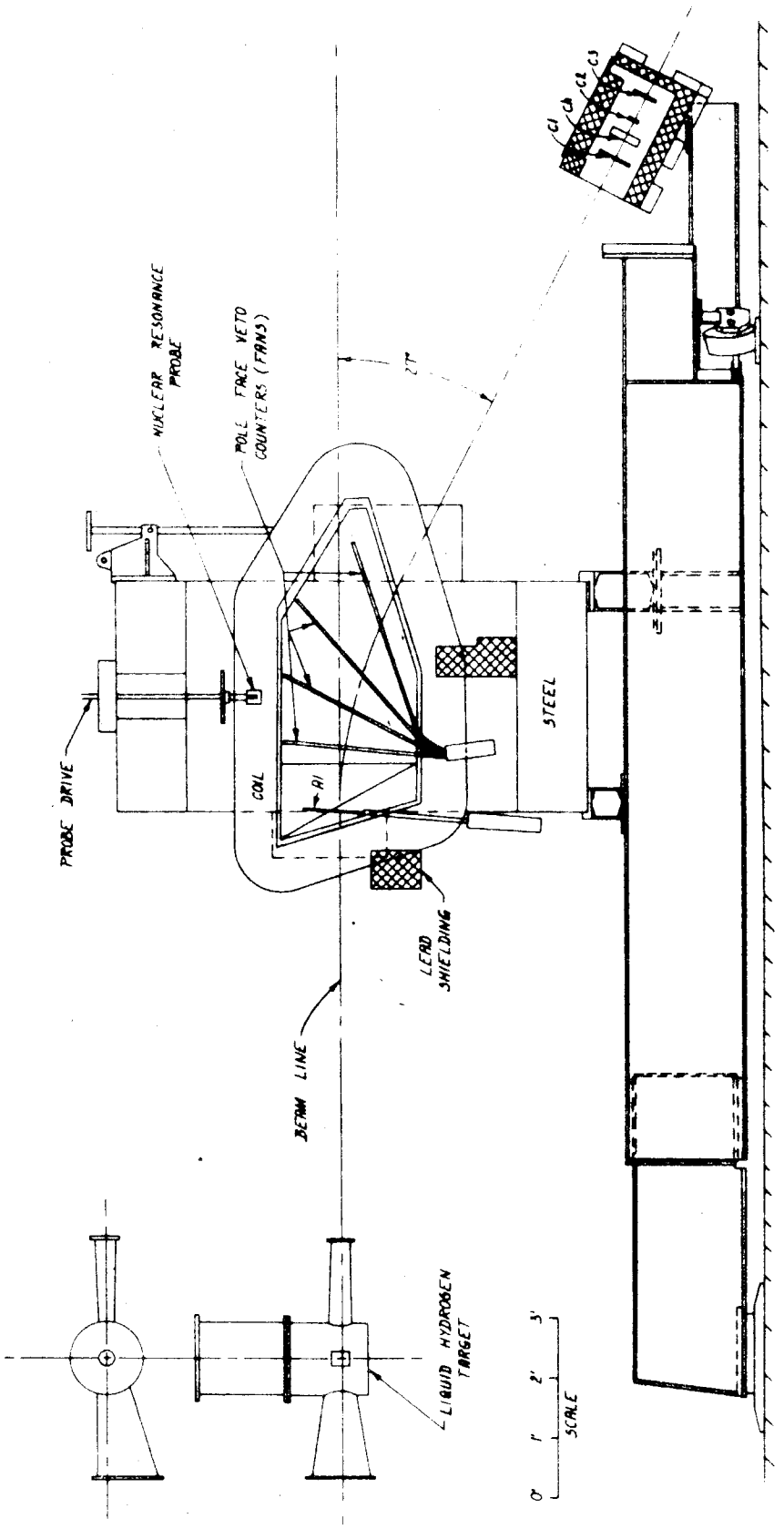

Spectrometer in High Energy Position

Figure 3b

D. Magnetic Spectrometer System

The recoil protons were momentum analyzed and detected by a large, wedge-shaped, single focusing magnetic spectrometer and associated equipment. Two different configurations were used and are shown in Figure 3. In the first of these, the medium energy (ME) position, particles with momentum $\lesssim .62$ Bev/c can be analyzed; the second is the high energy (HE) position which is obtained by modifying the ME position and can handle momenta $\lesssim 1.17$ Bev/c.

Donoho (25) discusses the design of the spectrometer and gives parameters relating to it (many of which have been made obsolete by improvements, however). Some of the more interesting parameters are given in Table 2.

The characteristics of the counters used with the spectrometer are also outlined in Table 2. The positioning of the counter A1 is important.* The central ray referred to in the table is the path traced

---

*Counter A1 was positioned as follows:

ME Position--the coordinates of the center of the counter were:
horizontal direction--2-3/8" farther from the target than the front edge of the main pole face;
vertical direction--15-1/8" below the top corner of the main pole face, or 1/8" above the center of the lower bolt hole in the pole face.

HE Position
horizontal direction--the plane containing the front face of A1 intersects the top edge of the pole tips 5-1/8" from the front top corner of the pole tips;
vertical direction--the top of A1 was 3-7/8" below the top of the pole tips.

For both positions the top edge of the aluminum bracket was flush against the lower return yoke of magnet; the bottom edge was shimmed to position the counter as described above. The counter was centered between the two pole faces.

Table 2

Characteristics of the Spectrometer System

Magnet	$\Delta\Omega$	$\frac{\Delta p}{p}$	$\Delta\Omega \frac{\Delta p}{p}$	Radius of Curvature	Angle of Deflection	Magnification
MEM	.00612 SR	.0427	2.61×10^{-4} SR	139 cm	50°	.75
HEM	.00197 SR	.0419	$.823 \times 10^{-4}$ SR	267 cm	27°	.89

Counter	Type	Distance (cm) from Target* ME	HE	Dimensions (cm) H x W x T	Uses
A1	polystyrene (CH) base scintillator	155	273	31.4 x 8.23 x .622	1. limit acceptance in vertical direction 2. assure passage of particle through magnet 3. time of flight
Fans	"	252 (rear fan)	381	80. x 1.27 x 1.90 (two arrays of four rods each)	1. eliminate particles scattered from pole faces 2. limit acceptance in horizontal direction
C1	"	398	641	14.6 x 27.9 x 1.0	dE/dx particle selection
Ch	lucite ($C_5H_8O_2$)	not used	652	15.2 x 27.9 x 3.81	velocity particle selection
C2	CH base scintillator	419	661	5.1 x 27.9 x 1.98	1. dE/dx particle selection 2. define momentum interval accepted 3. time of flight
C3	"	433	676	14.6 x 27.9 x 2.0	1. dE/dx particle selection 2. partially limit acceptance in horizontal direction (HE position only)

* Along central ray

by a particle emitted in a horizontal direction from the center of the target and with momentum such that it passes through the center of counter C2. The solid angle is limited by counter A1, the fan counters, and (HE position only) counter C3. Counter C2 limits the momentum acceptance of the system. More details concerning the uses of the various counters in the selection of protons are given in Section III and in the appendices.

The spectrometer constants $\Delta\,\Omega\,\frac{\Delta p}{p}$ for the two positions have been obtained by changing Dixon's (26) values to take into account the difference in C2 width. It was assumed that the average value for $\Delta\,\Omega$ is independent of the momentum interval width. Dixon's values of $\frac{\Delta p}{p}$ were multiplied by the ratio of the narrow C2 counter width used in this experiment to that of the wide one used by Dixon (a factor of .42). The preliminary results of recent measurements made by Peck (27) indicate that $\frac{\Delta p}{p}$ is linear with counter width. The limiting effect by C3 on $\Delta\,\Omega$ in the HE position is combined with the absorption correction (see Appendix V).

Large amounts of shielding were used during parts of this experiment, especially during the HE runs when the rates in the individual counters increased because of the sweeping magnet being in use. To reduce the empty target background a vertical lead slit 13 cm across was formed by erecting two stacks of lead bricks next to the outer shield of the target as shown in Figure 1 (for the $\theta'_{\pi o} = 120°$ points there was no room for the stack next to the beam). At the $\theta'_{\pi o} = 60°$, k = .8 Bev point this slit was found to reduce the empty target background by 30 ± 10%. The long light pipe of counter A1 was shielded from the large number of particles coming from the target, some of which might have given small light pulses increasing the single rate of the counter. Lead was also

placed under the pole faces to help prevent unwanted particles originating in the target region from reaching the rear counters. This shielding is shown in Figure 3. In the latter half of the experiment lead walls were also erected at the rear of the magnet to reduce the single rates in the rear counters, and another wall was placed in front of the magnet to shield counter A1. Concrete blocks were finally placed in the path of the great numbers of electrons being swept toward the experiment by the sweeping magnet. See Figure 1 for details.

E. Decay Photon Detection System

This system consisted of two scintillation counters, a lead converter, a large lead glass total absorption Cherenkov counter, and associated shielding. The system was used only for the $\theta'_{\pi^o} = 60°$ points with $k \leq .94$. Some of the characteristics of the system are given in Table 3; a sketch of the equipment is shown in Figure 3a.

For the energies involved in this experiment the output of the lead glass counter for an incident photon or electron is proportional to the energy of the particle. The spread in output pulses for a particular energy is proportional to the square root of the energy; at 1 Bev the rms deviation corresponds to .06 Bev. Further details are given by Ruderman, et al. (28).

The decay photons in similar π^o photoproduction experiments (12, 16) have been limited by an aperture system consisting of an opening in a lead wall, backed by a scintillation counter placed in anticoincidence. The scintillation counter not only rejects unwanted charged particles passing through the opening, but also helps define the aperture limits by

Table 3

Characteristics of the Decay Photon Detection System

Symbol	Description	Distance (cm) from Target	Dimensions (cm) H x W x T	Uses
1B	polystyrene (CH) base scintillator	44	11.4 x 16.5 x 1.4	used only in setting up and testing of the system
1/2" Pb	lead converter	58	15.8 x 19.7 x 1.18	1. convert large fraction of the γ-rays to electron showers which can be detected by 1A 2. reduce 1A singles rate
1A	CH base scintillator	60	16.5 x 20.3 x 1.6	placed in coincidence with A to detect π^o decay photons
A	lead glass Cherenkov counter	65 (front edge)	30.5 x 35.6 x 35.6	1. detection of π^o decay photons a. in coincidence with 1A b. by itself 2. check on energy distributions of decay photons

rejecting photons which strike the edge of the aperture and produce electron showers. If such photons are not rejected, the limits are poorly defined and the efficiencies difficult to determine.

It was found that under the experimental conditions used in this experiment the singles rate in such a counter was so high that accidental vetoing would have been a problem, even with several centimeters of paraffin as protection against the large flux of low energy particles. This rate could have been cut down by using a smaller aperture, but this would have resulted in a serious decrease of efficiency. Another method considered was to place small counters along the edges of the opening in the lead wall. The aperture would then be well defined although charged particles would no longer be eliminated. This method was abandoned because of the large probability of having one of the π^{o} decay photons pass through the opening only to be vetoed by the second photon striking the edge and producing a shower.

In order to avoid these difficulties and to obtain large efficiencies no aperture was used, the photon limits being determined by the size of the Cherenkov counter. Such limits are still poorly defined since a photon striking the edge of the counter may or may not produce an appreciable shower in the counter. Such edge effects were not serious, however, because the pion decay at these high energies ($T \gtrsim .4$ Bev) is strongly peaked in the forward direction and most of the decays result in a photon passing through the central region of the counter.

Consistency checks were made with counters 1A and 1B to show that the charged particle contamination was small. Measurements were made of

the charged particle contribution at E_o = 1.2 Bev for the point θ'_{π^o} = 60°, k = .8 Bev (see Appendix VII). The number of charged particles observed agreed with that expected from charged pi pair production.

Lead walls were built up the sides and across the top of the Cherenkov counter to protect it from the laboratory background. A stack of lead bricks was placed next to the target to protect the counters from particles scattering off the scraper directly in front of the target.

F. Electronics

A block diagram of the electronics used to analyze the counter outputs from the spectrometer system is shown in Figure 4 for the HE position runs which included the lucite Cherenkov counter.

The fast time of flight coincidence circuit between A1 and C2 had 50 cm clipping stubs which gave a time resolution of 8 nsec (full width at half height). Particles whose times were off by 8 nsec had an efficiency of 4%. The efficiency for particles having the correct timing was found to be 99.4 $\pm$ .2%. This measurement was made using a smaller counter in front of A1 positioned such that a particle passing through it and the rear counter necessarily passed through A1 also; this small counter was placed in fast (~ 10 nsec) coincidence with C1. Because the inefficiency of .6% may have been the result of a few pions or electrons which were accepted by the rest of the system, but rejected by the time of flight circuit, no correction was made for this measured inefficiency.

A particle accepted by the time of flight circuit and giving sufficient pulse heights in C1, C2, and C3 to be accepted by the discriminators, but which did not pass through any of the fan counters, gave an output pulse

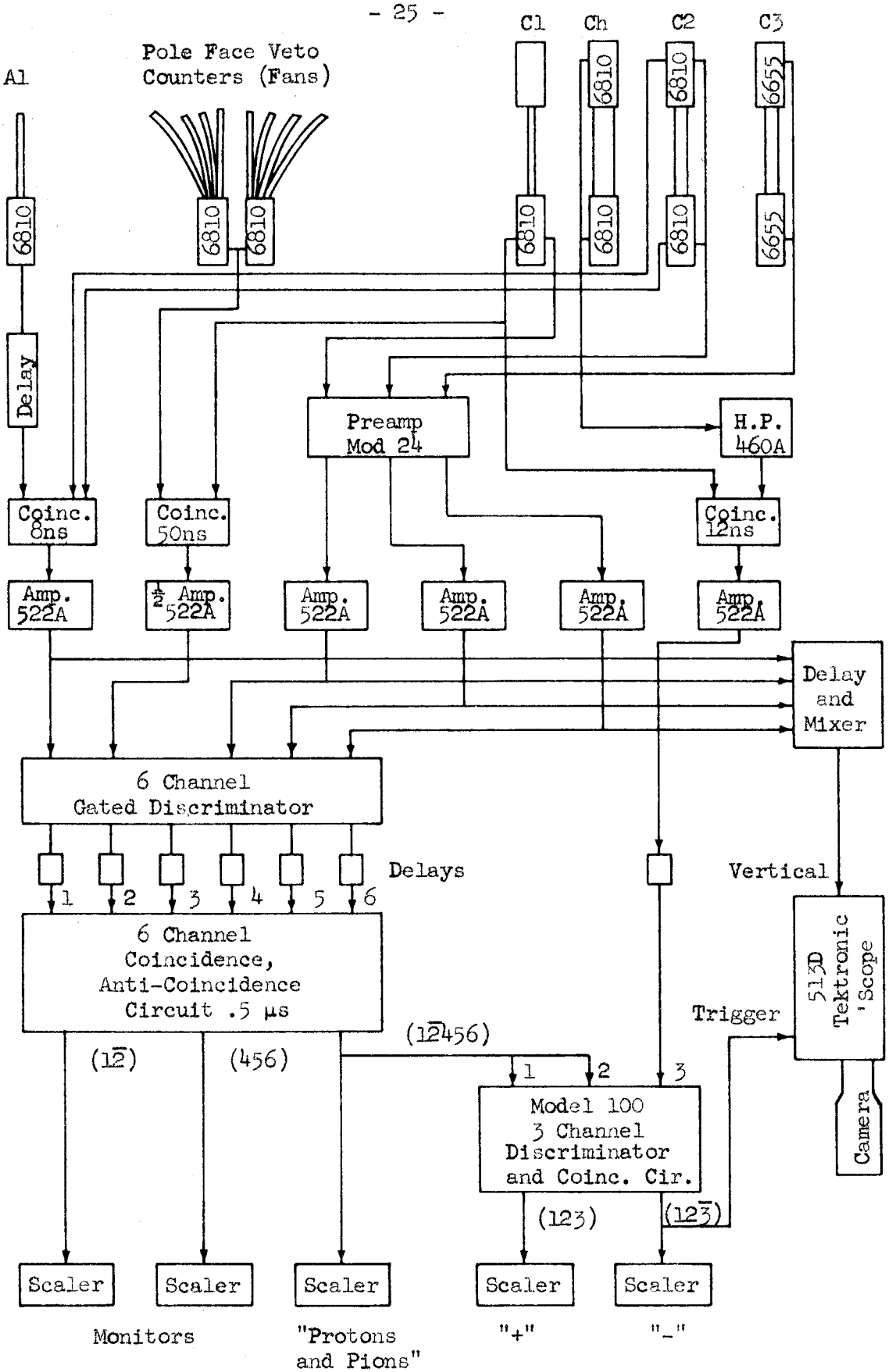

Spectrometer System Electronics

Figure 4

from the six channel coincidence circuit. In the ME position such a particle was labeled "proton." In the HE position this pulse was fed into a second slow coincidence circuit with the output of the Cherenkov circuit. This coincidence circuit gave a "+" count if the first slow coincidence pulse was accompanied by a Cherenkov pulse or a "-" count if not. The circuit was imperfect in that it occasionally gave both types of pulses for a particle whose Cherenkov output was close to the discrimination level of 35v.

The logic used for the decay photon detection and for combining the photon and proton information is shown by the block diagram, Figure 5. Counter 1B was not normally used and its associated electronics are not shown. A twenty channel pulse height analyzer was used to record the total absorption counter pulse height spectra. Three different counting rates were monitored: proton; proton + γ-ray; and proton plus converted γ-ray.

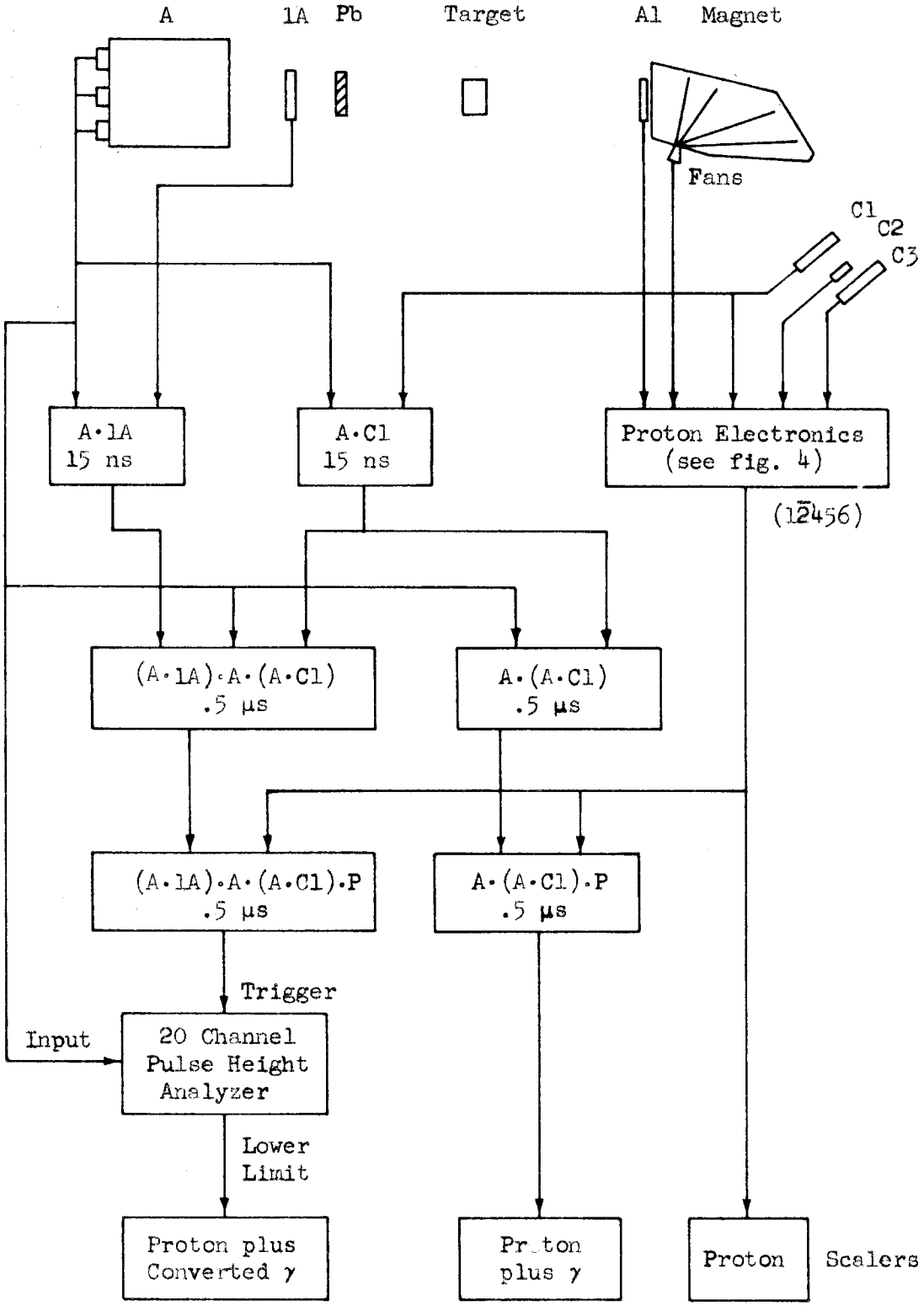

Decay Photon Logic

Figure 5

III. EXPERIMENTAL PROCEDURE

A. Proton Detection

Three methods were used to aid in the separation of the protons from the other particles passing through the spectrometer system: 1) time of flight between A1 and C2; 2) pulse heights in C1, C2, C3; and 3) for the HE position runs only, the output from the lucite Cherenkov counter.

The major contamination came from positive pions; in a few instances electrons were also important. Relevant proton and pion properties are given in Table 4 for selected momenta. For $p < .8$ Bev/c a clean separation between protons and pions could be made with either the pulse height or the time of flight information. As the momentum increased above .8 Bev/c, the different particles became more and more difficult to separate. At the highest momentum point, 1.17 Bev/c, only half the pions were rejected by the time of flight measurement; the three pulse height discriminations rejected another 10%.

Polaroid pictures of scope traces showing proton pulse heights in counters C1, C2, and C3 were used to set the biases on the pulse heights from these counters. The minimum proton pulse heights from the three counters were found and the biases set safely below the minima at each momentum studied. Pictures were taken during the runs and the pulse heights examined as a check that the equipment was not drifting or otherwise malfunctioning in such a manner that the biases were cutting into the proton pulses.

The proper time of flight delays were found by running delay curves for several particle velocities at each magnet position. The

Table 4

Properties of Protons and Pions for Particular Momenta

Momentum	ME Position .4	ME Position .5	ME Position .6	HE Position .6	HE Position .8	HE Position 1.0	HE Position 1.17	Bev/c
T_p	.082	.125	.175	.175	.295	.433	.562	Bev
T_π	.284	.389	.476	.476	.672	.870	1.038	
β_p	.39	.47	.54	.54	.65	.73	.78	
β_π	.94	.96	.97	.97	.98	.99	.99	
t_p	22	19	16	24	20	18	16	nsec
t_π	9	9	9	13	13	13	13	
$t_p - t_\pi$	13	10	7	11	7	5	3	
$-(dE/dx)_p$	8.6	6.2	4.9	4.9	3.6	2.9	2.6	Mev/$\frac{gm}{cm^2}$
$-(dE/dx)_\pi$	2.0	2.0	2.0	2.0	2.1	2.1	2.2	
$\frac{(dE/dx)_p}{(dE/dx)_\pi}$	4.3	3.1	2.4	2.4	1.7	1.4	1.2	

T = kinetic energy

β = velocity (c = 1)

t = time for particle to pass from A1 to C2 along central ray

variations of the delays with momentum were consistent with those calculated using the A1-C2 distance.

The lucite Cherenkov counter was used to better discriminate against the pion and electron contamination at high momenta. Brody (29) describes its design and construction in detail. In this experiment it was put in fast coincidence with C1. The level of discrimination on the output of the coincidence circuit was placed at a moderately high (35v) level. This made the counter less efficient than that measured by Brody: the efficiency for detecting protons with $p < .8$ Bev/c dropped from Brody's 2% to less than $\frac{1}{2}$%, while that for pions dropped from 98% to 90%. For more details of the Cherenkov efficiency and its use see Appendix VI.

B. Photon Detection

The photons were detected by two methods. The first of these consisted of merely accepting any particle which made a pulse in the large lead glass counter in coincidence with a proton passing through the spectrometer. The second required a pulse from the smaller scintillation counter, 1A, as well as the lead glass counter and proton system.

The geometric efficiencies of the two counters for detecting at least one of the π^0 decay photons were calculated by R. Talman with a Monte Carlo program. The results are shown in Figure 6 for the points at which the decay was detected; the error flags show the statistical inaccuracy of the calculations. The lead glass counter was quite efficient because of its large size.

The bias on the lead glass counter output was set low enough to accept all decay photons which made a shower in the glass; its total

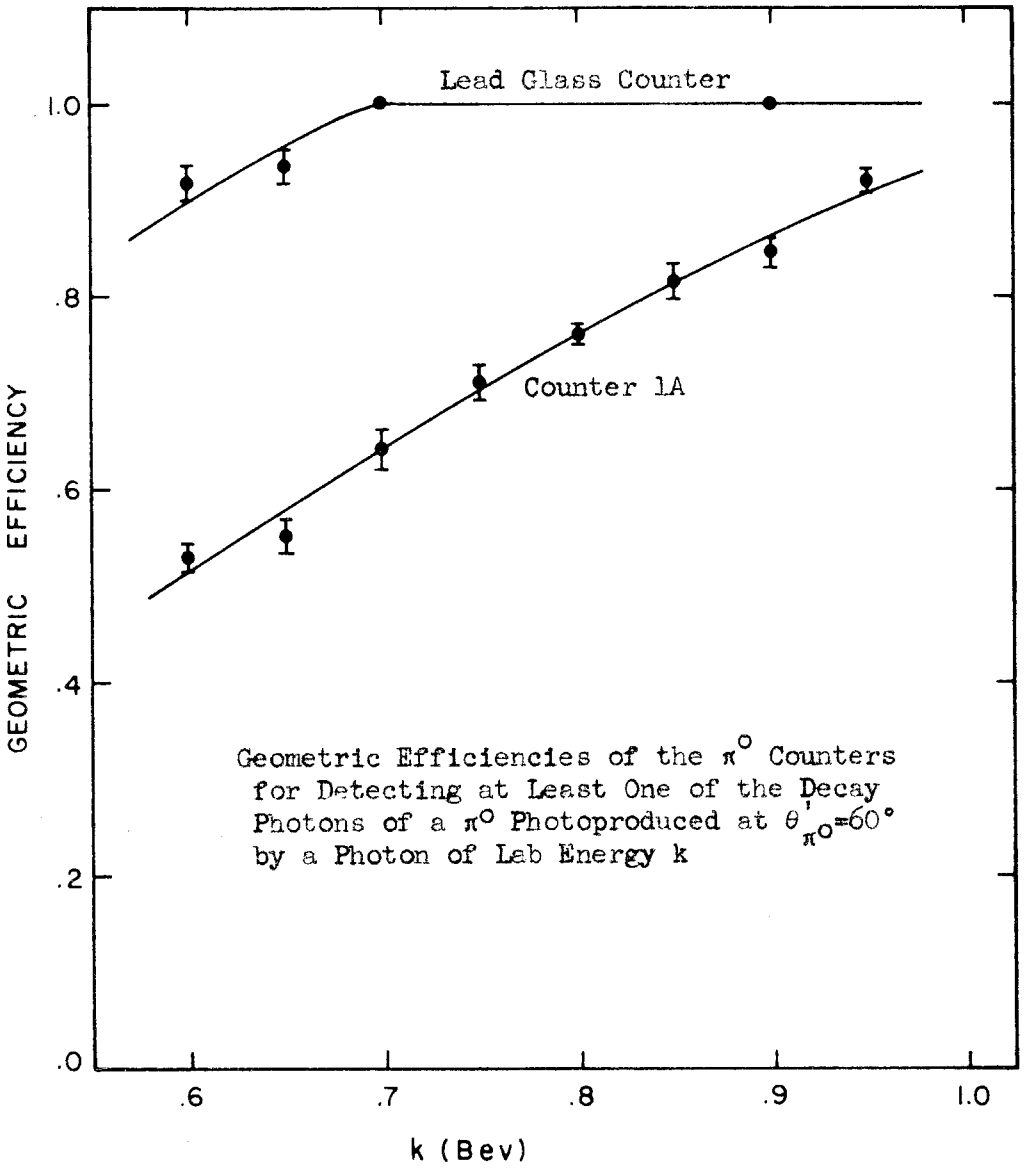
Lead Glass Counter
Counter 1A
GEOMETRIC EFFICIENCY
1.0
.8
.6
.4
.2
.0
.6
.7
.8
.9
1.0
k (Bev)
Geometric Efficiencies of the π° Counters for Detecting at Least One of the Decay Photons of a π° Photoproduced at θ'π°=60° by a Photon of Lab Energy k

Figure 6

efficiency was therefore just the geometric efficiency. The efficiency for 1A to detect the decay of the π^o depended not only on the geometry, but also on the efficiency of the 2.29 radiation length lead converter placed in front of 1A. This efficiency was calculated to be .786 $\pm$ .003. The calculation took into account the small contributions from the other material placed between the point of production and counter 1A, and from the contribution from the π^o decay: $\pi^o \rightarrow \gamma + e^+ + e^-$ which occurs in about 1% of the decays. The electron pair production cross sections needed for the calculation were taken from a theoretical formula of Davies, et al. (30) which is in agreement with experiment. A crude calculation indicated that the probability of a shower, once initiated, being entirely photons at the scintillation counter was ~ .7%. This effect was included in the efficiency given above.

Because of the inefficiency of counter 1A, the π^o cross sections were obtained from the proton plus lead glass counter rates which had better statistical accuracy; the counting rates which included counter 1A were used in a consistency check with the proton plus lead glass rates. The check was made by calculating the converter efficiency η from the two γ-ray plus proton rates under the assumption that only π^o decays were being detected. If this assumption were wrong, one might expect to obtain strange values for η.

The results are shown in Figure 7 for the cross section points at which the π^o decay was detected, and also for the points taken as a function of E_o with the apparatus set to observe π^o photoproduction at .8 Bev. The expected value of .786 is also shown for comparison. The error flags on the points reflect the counting statistics and the uncertainties in the geometric efficiency; the fact that the two counting

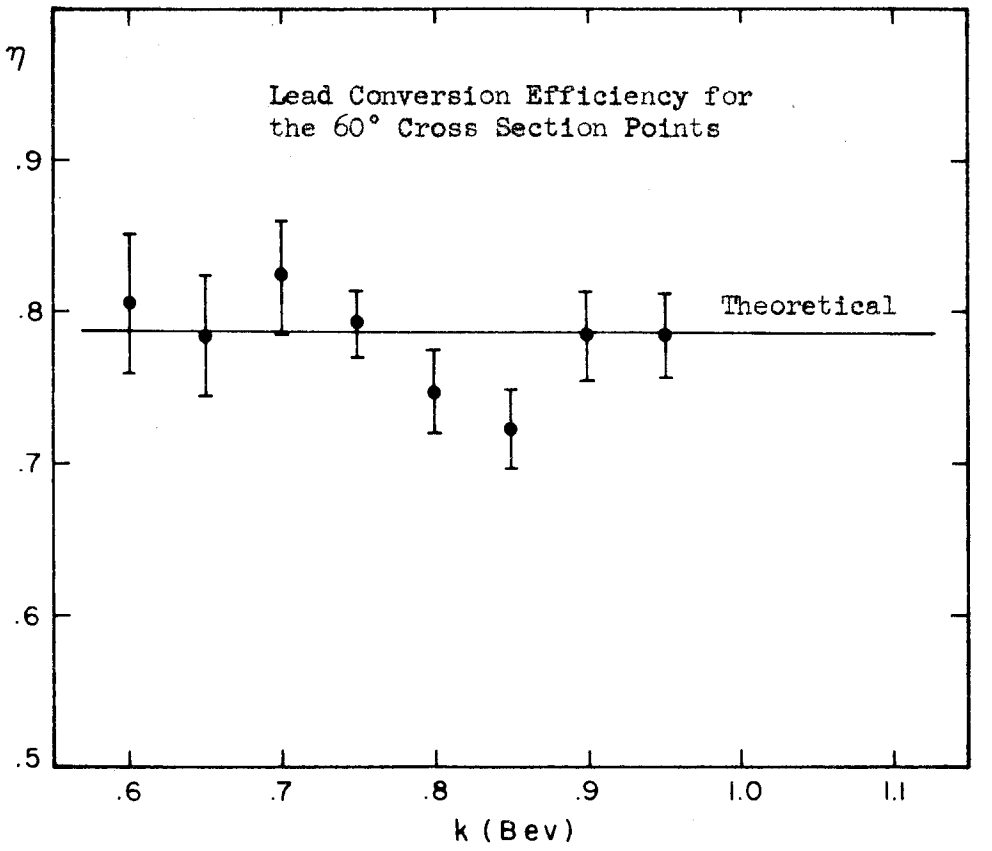
η
Lead Conversion Efficiency for
the 60° Cross Section Points
Theoretical
.9
.8
.7
.6
.5
.6
.7
.8
.9
1.0
1.1
k (Bev)

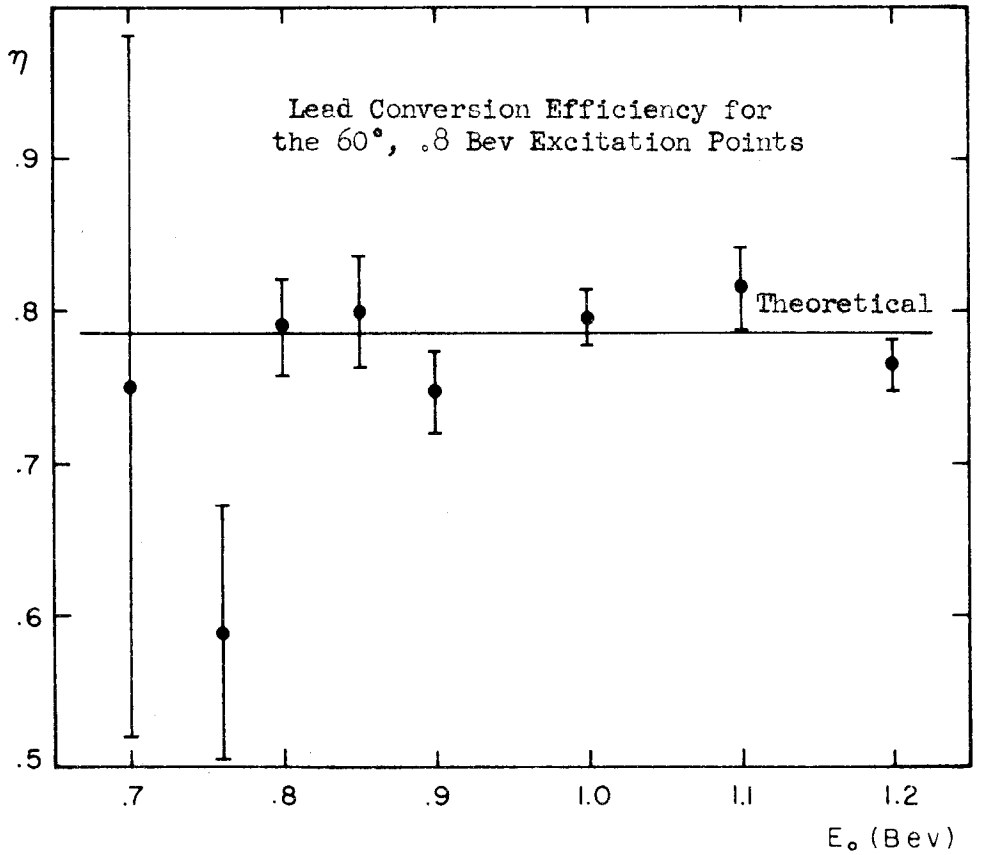
η
Lead Conversion Efficiency for
the 60°, .8 Bev Excitation Points
Theoretical
.9
.8
.7
.6
.5
.7
.8
.9
1.0
1.1
1.2
E₀ (Bev)

Figure 7

rates being compared are not statistically independent was taken into account. The probability that larger fluctuations from .786 occur for the cross section points is 30%.

The average for all the points is $\eta = .779 \pm .007$ which is not inconsistent with the system detecting the decays of photoproduced π^o's only. As is discussed in Appendix VII, however, there was contamination from pi pair photoproduction at the large E_o values of the excitation curve. A crude calculation shows that just above the threshold for pair production ($\sim$ 1.00 Bev for this point) the probability is almost 100% that 1A will see at least one of the pions. Taking into account the geometric efficiencies assumed in the calculation, this corresponds to $\eta = 1.3$ for charged pi pairs. Further above the threshold more laboratory solid angle is available to the pions and the effective η drops to $\sim .5$ for charged pairs produced by 1.2 Bev photons. Averaging the effect of charged pairs with that for π^o production gave $\eta = .816$ at $E_o = 1.1$ Bev; this was observed experimentally (see fig. 7b). At $E_o = 1.2$ Bev the crude calculation gave $\eta = .789$, i.e., the efficiency for detecting charged pi pairs is almost exactly the same as for single π^o's for this end point energy; the experimental point is a standard deviation lower than expected.

Runs were made without the lead converter and the total absorption counter output spectrum was compared with that computed by Talman's Monte Carlo program for the energy of the decay photons from photoproduced π^o's. The experimental spectrum so obtained was consistent with the calculated one. The lead converter was found to lower the pulse heights of the total absorption counter by an amount corresponding to $\sim .1$ Bev.

IV. DATA REDUCTION

A. Cross Section Formulas

The counting rate of recoil protons from single π^o photoproduction can be expressed as a multiple integral over the target volume, photon energy, and laboratory solid angle:

$$C = \int\cdots\int\sigma(k,\theta')\ n_H\ N(k)\ n(x,y)\ A\ \left(\frac{\partial\Omega'}{\partial\Omega}\right)_k d\Omega dk dx dy dz$$

where

C = number of protons/100 BIPS giving a proton signature,

$\sigma(k,\theta')d\Omega'$ = differential cross section for single π^o photoproduction from hydrogen by a photon of energy k, producing a recoil proton in $d\Omega'$ at θ' (primed quantities refer to the c.m. system),

n_H = number of protons per unit volume,

$N(k)dk$ = number of photons per 100 BIPS with energies between k and k + dk (see Section IIB),

$n(x,y)$ = relative beam intensity at point x,y in a plane perpendicular to the beam at the target,

A = correction for proton absorption and for counter C3 inefficiency (see Appendix V),

$\left(\frac{\partial\Omega'}{\partial\Omega}\right)_k$ = solid angle transformation factor, and

z = distance from target center in the direction of the beam.

The limits of integration are determined by the limits of the target-beam interaction volume and by the spectrometer acceptance limits.

The multiple integral is quite complicated and would require a great deal of programming and computer time if it were carried out in detail for each experimental point. Instead, several approximations and a transformation of variables were made. The errors inherent in these approximations are less than the errors due to the uncertainties in the various quantities and limits. The approximations and the transformation may be represented schematically as:

$$\int n(x,y)dxdydz \rightarrow \overline{\ell}$$

$$\int d\Omega \rightarrow \Delta\Omega$$

$$\int dk \rightarrow \left(\frac{\partial k}{\partial p}\right)_\theta \frac{\partial p}{\partial p_o} p_o \frac{\Delta p_o}{p_o}$$

where

$\overline{\ell}$ = effective length of the hydrogen target (see Section IIC),

$\Delta\Omega$ = solid angle of spectrometer averaged over particle momentum,

p_o = central momentum of the spectrometer,

p = proton momentum at production, and

Δp_o = effective width of the momentum interval accepted by the spectrometer.

The multiple integral thus reduces to

$$C = \overline{\sigma(k,\theta')}\, N_H N(k) A \left(\frac{\partial\Omega'}{\partial\Omega}\right)_k \left(\frac{\partial k}{\partial p}\right)_\theta \frac{\partial p}{\partial p_o} p_o \left(\frac{\Delta p_o}{p_o} \Delta\Omega\right).$$

The fact that $\sigma(k,\theta')$ has been averaged over the photon energies determined by the experimental resolution is shown explicitly by the "——"; σ does vary rapidly enough with k that this averaging effect becomes important as is shown in Section V. N_H is the effective number of hydrogen nuclei/cm^2 in the target; for the full target

$$N_H = \frac{N_o}{M}\left(\rho_H \bar{\ell} + \delta_{H,Mylar}\right)$$

$$= 3.04 \times 10^{23} \text{ free protons/cm}^2$$

N_o = Avogadro's number,

M = atomic weight of hydrogen,

ρ_H = density of liquid hydrogen, and

$\delta_{H,Mylar}$ = gm/cm^2 of hydrogen in the molecular structure of the Mylar cup.

The factor $\frac{\Delta p_o}{p_o} \Delta\Omega$ is a constant for each spectrometer position; values are listed in Table 2.

The above equation can be used to obtain $\bar{\sigma}$ from C:

$$\overline{\sigma(k,\theta')} = C/\kappa$$

where

$$\kappa = N_H N(k) A \left(\frac{\partial\Omega'}{\partial\Omega}\right)_k \left(\frac{\partial k}{\partial p}\right)_\theta \frac{\partial p}{\partial p_o} p_o \left(\frac{\Delta p_o}{p_o} \Delta\Omega\right).$$

See Table A2 for the evaluation of the various factors at each experimental point.

B. Counting Rate Corrections

Several corrections to the proton counting rate had to be made to take into account the contributions from the various competing processes.

The largest correction to the foreground proton rate, F, was the background from the complex nuclei of the target. Usually this contamination is corrected for by subtracting the empty target counting rate from that of the full target. The empty target rate generally varies smoothly with energy and angle because it comes mainly from complex nuclei (the Fermi momenta of the nucleons in the complex nuclei tend to smooth out any rapid fluctuations). For this reason empty target runs are often taken at only every second or third point and the results interpolated for the intermediate points. However, the nominally empty target of this experiment still had a small amount of hydrogen ($\sim$ 3% of the full target), both as gas and as a constituent of the Mylar walls of the cup. That part of the empty target counting rate coming from this residual hydrogen can fluctuate rapidly. To eliminate this effect the full and empty counting rates were used to compute C_x, the counting rate from the complex nuclei of the target. This quantity was then interpolated to give the contamination at points for which no empty target run was made. The formula for C_x is developed in Appendix III. In general, the results of this formalism did not differ appreciably from those obtained by the simple subtraction of rates; there were a few instances, however, in which interpolation of the empty target rates would have been misleading. C_x was about 50% of the rate from hydrogen for the $\theta'_{\pi^0} = 60°$ points; requiring a γ-ray in coincidence reduced this to 1 or 2%. At 90° and 120° the complex nuclei rates were typically 15% of the hydrogen rates.

The contributions from two other contaminations were also subtracted from F. The first is the "below threshold background" discussed in Appendix VIII. This contamination is presumably the result of wide angle nuclear scattering, although the specific mechanisms studied in Appendix VIII appear to be unable to account completely for the contamination observed experimentally. At $\theta'_{\pi^o} = 60°$ it was 10 to 20% of the single π^o rate if only protons were detected; requiring one of the π^o decay photons reduced this to .5%. At the other angles it was typically 2 or 3% (protons only). The final contamination correction was for pi pair production and is discussed in detail in Appendix VII. It was $\lesssim$ 1% of the single π^o rate.

The foreground rate and the three corrections just discussed are shown in Table A1 for each of the experimental points; also shown is the corrected proton rate, C.

Corrections were not made for Compton scattering from protons. The existing experimental data above the first resonance (31,32) are quite meager and appear to be not consistent, possibly indicating systematic errors. An attempt to calculate the cross section by assuming that only a few terms are important has been made by Berkelman (33). His results indicate that above the first resonance the cross section depends strongly on the π^o lifetime. At k = .6 Bev, for example, if one assumes a π^o lifetime of 2×10^{-16} sec (the result of emulsion experiments), the differential Compton scattering cross section is expected to be less than .03μb/SR at all angles (cf. $\sigma(\gamma + p \rightarrow \pi^o + p) \sim$ 2.5μb/SR). If the lifetime is only 10^{-17} sec, the cross section is expected to be strongly peaked in the backward direction with a value of .12μb/SR at $\theta'_{\gamma} = 120°$.

Experiments are in progress at both Cornell and Frascati which will hopefully give a better indication of the Compton cross section. Because of the similarity of kinematics, the constant κ relating cross section to counting rate is nearly the same (to within $\sim 15\%$) for Compton scattering as for single π^o production at the angles studied by this experiment. The single π^o production cross section can thus be obtained approximately by simply subtracting the Compton scattering cross section, once known, from the results obtained by this experiment. The accuracy of the experiments of the next few years will probably be such that a more precise subtraction will not be called for.

The cross sections of this experiment are thus very nearly the sum of the single π^o production and Compton scattering cross sections, the latter presumably being at most a few per cent of the total.

C. Errors

Neither the corrections just discussed nor the various factors of κ are known precisely. The uncertainties in these quantities combine with counting statistics to give an uncertainty in the cross sections. These errors (considered as standard deviations) are conveniently grouped as to their variation with photon energy. Only quantities with errors $\geq 1\%$ are listed:

1. Errors in the absolute cross section which are constant or slowly varying.

   a. $N(k)$ 4%

   b. $\frac{\Delta p_o}{p_o} \Delta \Omega$ 3%

   c. N_H 1%

2. Random and rapidly varying errors.

   a. Counting statistics typically 6%

   b. C_X (target background) typically 3%

   c. C_{BTh} (below threshold background) .5 to 5%

   d. C_{Pr} (pi pair contamination) ≤1%

   e. A (15% of 1-a) ~1%

The errors 2a-d are given for each experimental point in Table A1. Combining these errors in the usual way gives the standard deviation of C which is shown in the same table; it is this deviation which is shown by the error flags in the figures of the next section. The flags thus indicate the amount by which the curve shapes may be in error. If the results are used as a measure of the absolute cross sections, care must be taken to fold in the additional 5% uncertainty of the factors listed in part 1.

If a comparison of these results with those of other experiments is desired, however, one need not always fold in the complete 5% of part 1. For example, Cornell uses a similar beam monitoring standard which has been found to agree with the Caltech standard to within 1/2%; thus, that part of the uncertainty in N(k) which depends on beam monitoring need not be considered when comparing Cornell and Caltech results, and only an additional 4% error from part 1 need be folded into the error flags.

There is a systematic uncertainty of .4% in the photon energy or .25% in total center of mass energy (see Appendix IV for details).

V. RESULTS AND DISCUSSION

A. Unfolded Fits

The values obtained for $\overline{\sigma(\theta')}$ are listed in Table A2. As previously mentioned, this experiment actually measured the sum of the cross sections for single π^o photoproduction and Compton scattering; also the errors listed indicate only the random and rapidly fluctuating errors (standard deviations). These values have been plotted in Figures 8a-c as a function of the total center of mass energy W; also shown is a scale of incident photon energy k.

Typical experimental resolutions are shown at the bottoms of the figures. They were calculated from the properties of the spectrometer, the geometric arrangement of the target-beam interaction volume, and the slowing and scattering properties of protons. Details are given in Appendix IX. Note that the 60° points have considerably wider resolutions than do the other points because of unfavorable kinematic conditions (see fig. A10). A convenient way to characterize the resolution widths is with the dimensionless parameter

$$w = \Delta k/k$$

where

Δk = the full width of the resolution function at half maximum, and

k = the median photon energy.

For a particular spectrometer position and center of mass angle, w was constant to within 5% for this experiment; average values are listed in Table 5.

Figure 8. Results with Unfolded Fit

8a. $\theta'_{\pi^0} = 60°$

8b. $\theta'_{\pi^0} = 90°$

8c. $\theta'_{\pi^0} = 120°$

The experimental results are shown as the points. The error flags represent the random and rapidly fluctuating errors; not shown is the 5% uncertainty in absolute normalization. The solid curves show the results of a calculation made to eliminate the effects of experimental resolution. The dashed curves show the effects of the experimental resolution on the solid curves; they are only shown where the averaging had an appreciable effect. Typical resolution functions are shown at the bottoms of the drawings. The goodness of each fit is indicated by the chi-squared probability, P_{χ^2}.

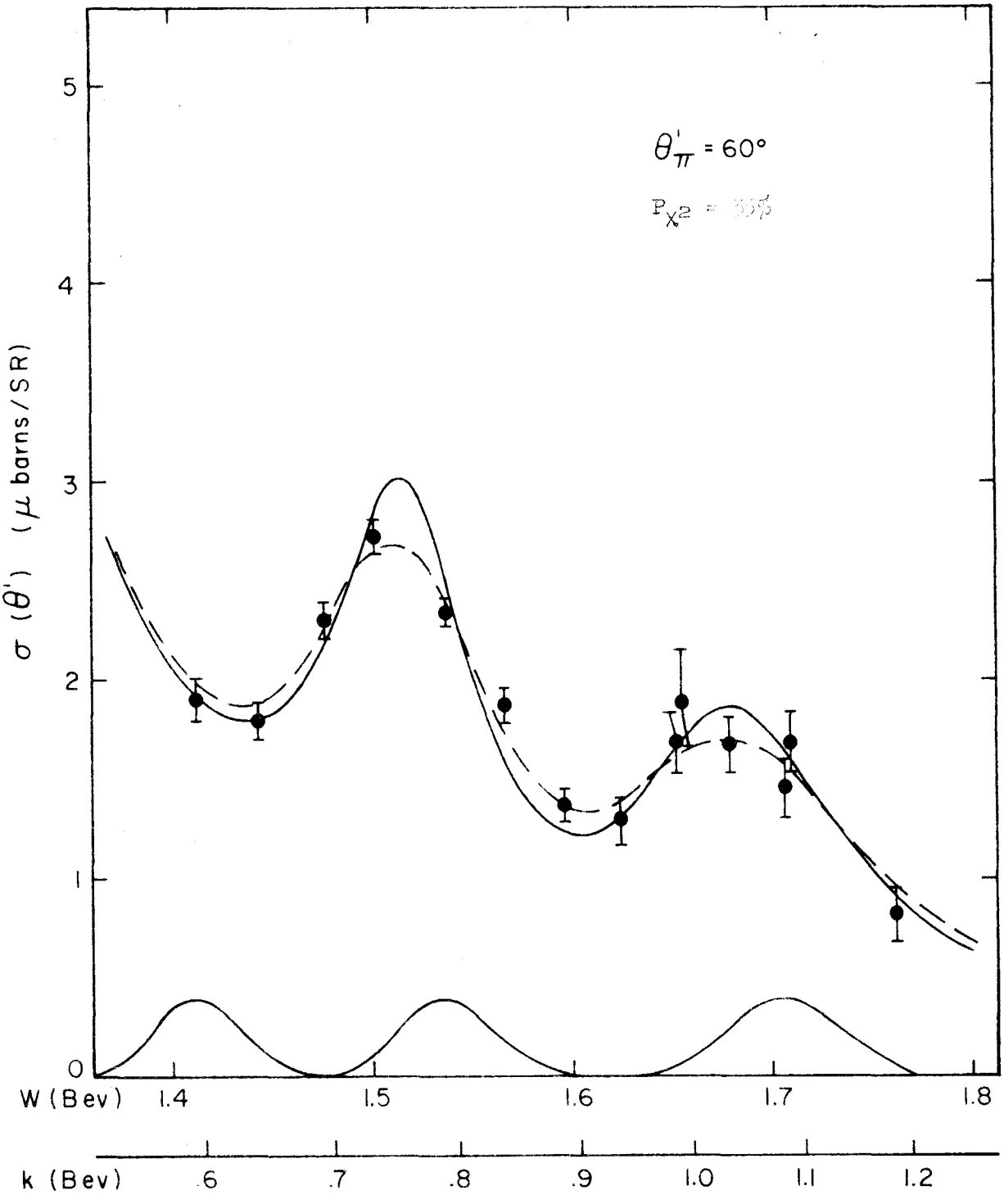

60° Unfolded Fit

Figure 8a

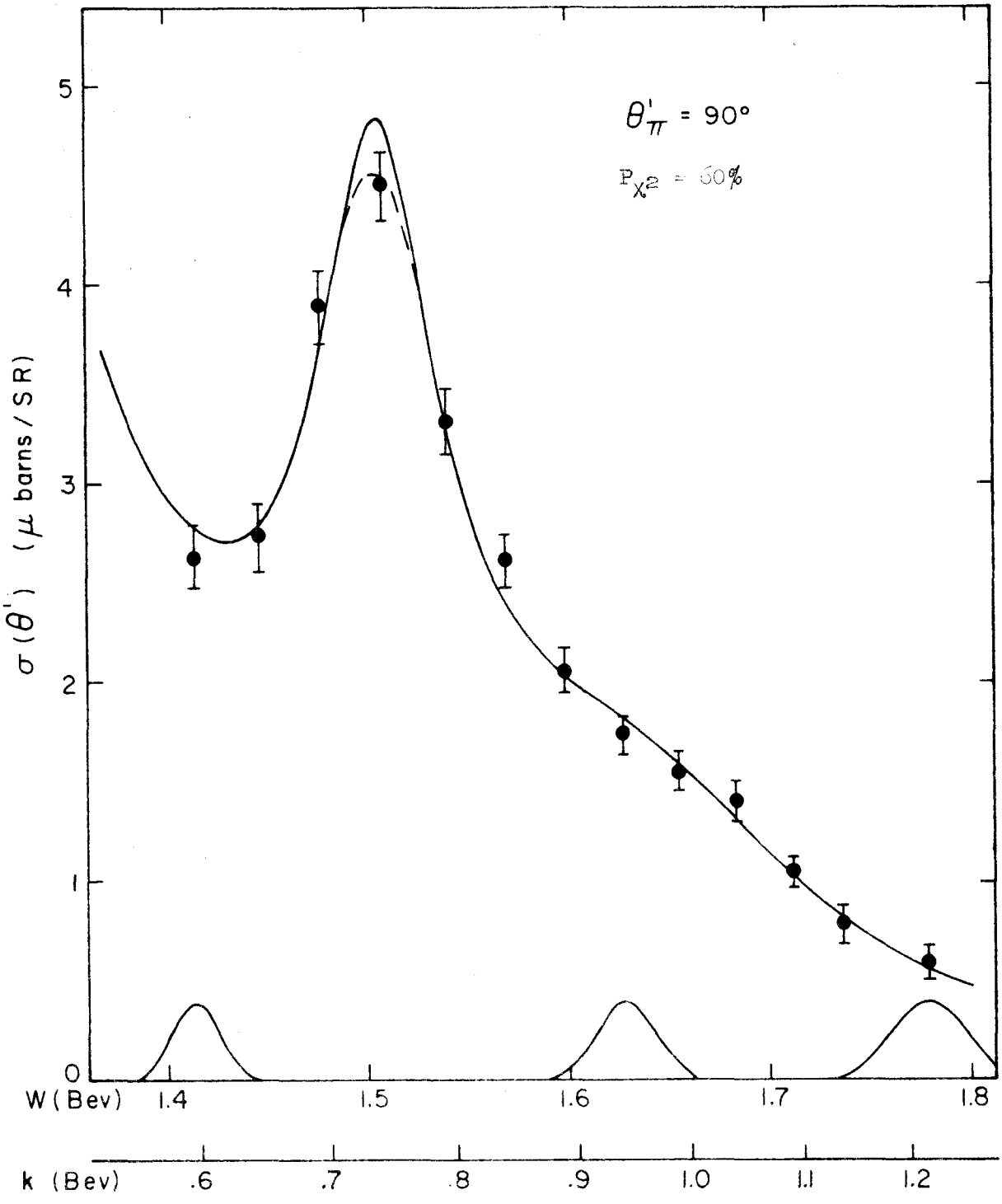

90° Unfolded Fit

Figure 8b

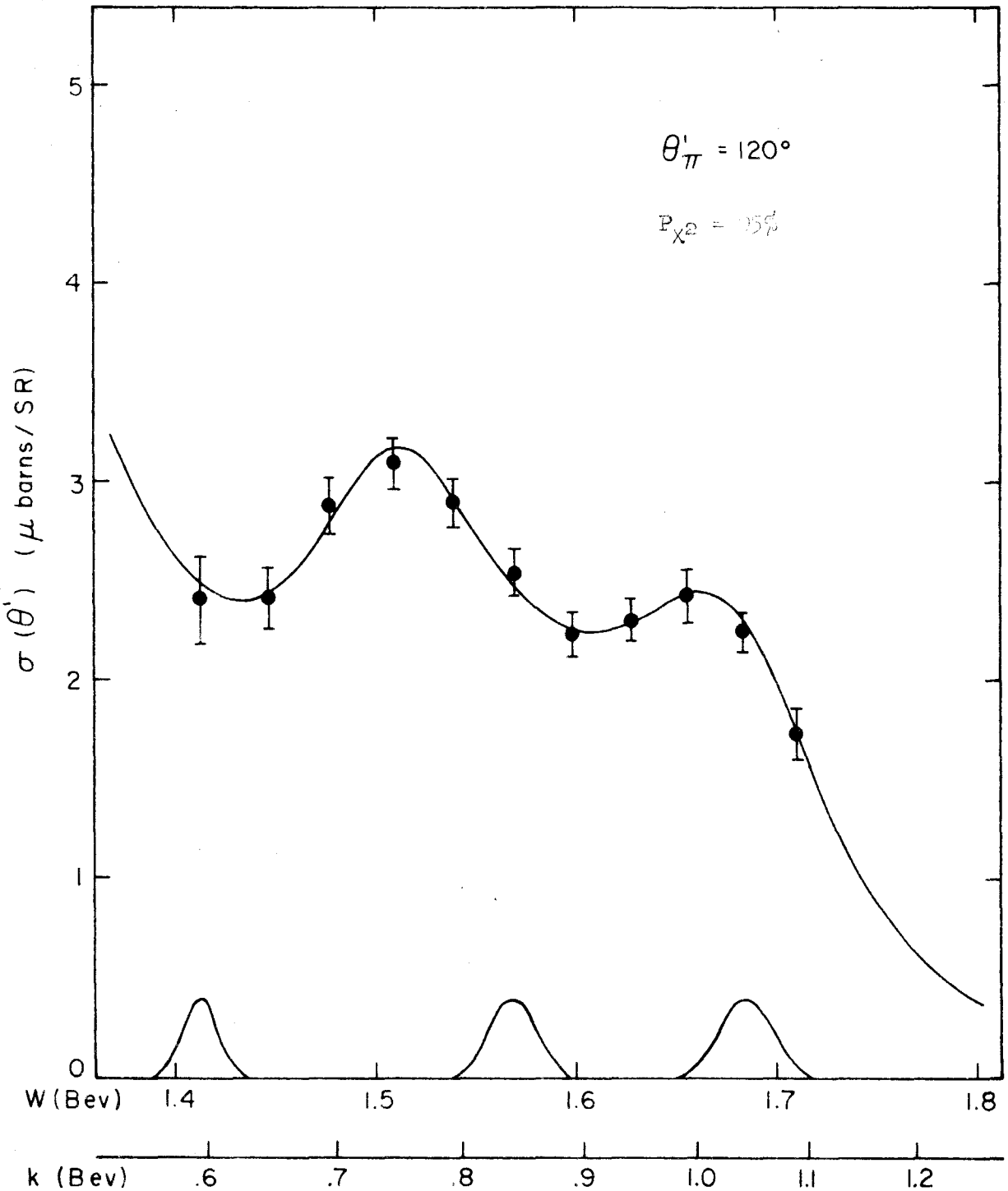

120° Unfolded Fit

Figure 8c

Table 5

Reduced Resolution Widths for This Experiment

θ'_{π^0}	Spectrometer Position	$\bar{w}$
60°	M	.116
60°	H	.093
90°	M and H	.065
120°	H	.053

An attempt was made to eliminate the smearing effects of the resolution by assuming that the cross sections at each of the three angles could be approximated by a general shape with six free parameters. At each angle these parameters were adjusted to give the best statistical fit to the data.

The general shape which was used for this "unfolding" process was the superposition of three resonances and their interference terms. The shapes of the resonance terms were assumed to have the form of the single level formulas of Feshbach, et al. (34) who derive a Breit-Wigner type of formula, but with nonrelativistic angular momentum barrier penetration factors which result in the "resonance width" being a function of energy. For details see Appendix X.

The quantum numbers for the three resonances were taken to be those of Peierls (18) and are listed in Table 6.

Table 6

Peierls' Assignments for the Resonances

Resonance	Multipole	Parity	ℓ_j	I
1st	M1	+	$P_{3/2}$	3/2
2nd	E1	-	$D_{3/2}$	1/2
3rd	E2	+	$F_{5/2}$	1/2

The phases are assumed to go from 0° to 180° as the energy increases, passing through 90° at the resonant energy, and the signs of the amplitudes are taken to be positive. These assignments give the recoil proton polarization in the direction observed experimentally. The quantum numbers together with the phases determine the relative amount of interference terms at the various angles.

The parameters of the first resonance were obtained from the low energy data; the formula of Feshbach was then used to extrapolate the first resonance contribution to the higher energies considered in this experiment. The parameters of the second and third resonances were used to fit the data of each angle individually. This gave six parameters (the position, width, and strength of each of the two resonances) which were adjusted to reduce χ^2 where

$$\chi^2 = \sum_i \left[\frac{\overline{s_i(\theta')} - \overline{\sigma_i(\theta')}}{\Delta_i} \right]^2$$

$\overline{s_i(\theta')}$ = the differential cross section as obtained from the above formalism averaged over energy in the same manner as the experimental averaging for the i^{th} point,

$\overline{\sigma_i(\theta')}$ = the differential cross section obtained experimentally at the i^{th} point, and

Δ_i = the standard deviation of $\overline{\sigma_i(\theta')}$.

Values for χ^2 were obtained for several values of the parameters; these values were used to estimate the location of a minimum in χ^2 (Newton's method). This new location was then used as a center about which to vary the parameters to estimate a still better location, and so on.

The unfolded fits corresponding to minimum χ^2's are shown in Figures 8a-c as the solid lines. The resonance positions and widths of these fits are shown in Table 7 (part F of this section). Averaging over the fits in the same manner as the experimental averaging gave the dashed curves (shown only where the averaging had appreciable effect). When comparing the fits to the data, reference should be made to the dashed rather than solid curves. The three fits taken together were statistically better than average with $P_{\chi^2} = 70\%$. The statistical goodness of each fit is given in the figures.

As can be seen in Figure 8a, the large resolution of the 60° points did smear out the cross section appreciably. The smearing at the other angles is not important except in the region of the sharp 90° second resonance peak.

The best values for the differential cross sections at the three angles are felt to be those obtained by the fits just described, in spite of the fact that they do depend slightly on the particular form of the fitting functions used. Not only do these fits "unfold" the effects of resolution, but they also tend to smooth out the random statistical fluctuations.

If the cross sections were to actually be of the form assumed, the average standard deviation of the fit from the true value at the points measured would be $\sim\sqrt{\frac{6}{n}}$ times the average standard deviation of the experimental points, where n is the number of points taken at the particular angle. Due to the uncertainty in the shape, however, the errors shown on the experimental points are probably better indications of the rapidly fluctuating uncertainties.

B. Contour Map of the Differential Cross Section

The cross sections obtained at the three angles were fit in $\cos\theta'$ with parabolas. In the region of the second resonance the large 90° cross section drives the fit negative at both 0° and 180°, indicating the need for fourth order terms in this region. Fourth order terms have been found to be important at the third resonance by previous experiments. For these reasons angular distribution fits could not be determined by this experiment.

Rather than show explicitly the angular distributions obtained at the 11 energies measured by this experiment, a different scheme has been used to display the angular distribution as a function of energy. Figure 9 shows lines of constant differential cross section as a function

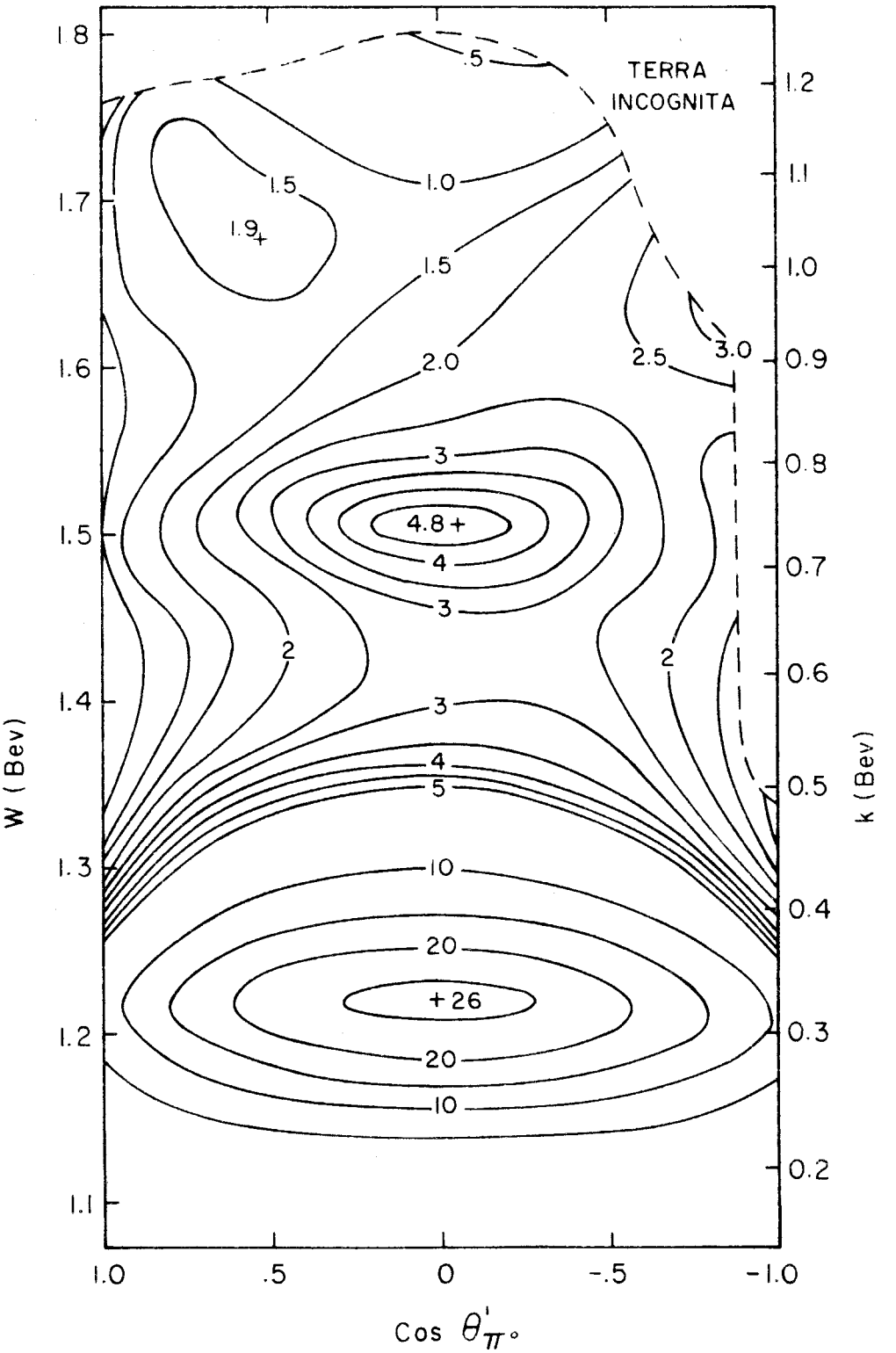

Figure 3

Lines of Constant Differential Cross Section

for $\gamma + p \rightarrow \pi^o + p$

of the total center of mass energy and $\cos\theta'_{\pi^0}$. Note that the interval changes from 5 to 0.5μb/SR in going from the first to second resonance.

The positions of the lines in the region of this experiment were determined by the unfolded (solid line) fit described in Part A of this section. The results of the numerous other experiments were used to extend the lines to other angles at the energies of this experiment and to give the behavior at the first resonance.

The choice of which data to use and how to interpret it was somewhat arbitrary; the deciding factor was often an artistic one. A careful examination of the various possible systematic errors and the effects of wide resolution was not made for the other experiments; these effects were taken into account, however, although in a subjective manner. This points out a disadvantage of such a representation; one cannot easily indicate either the uncertainties in the cross section or the agreement (or lack of it) between different experiments.

It is interesting to note that while the appearances of the first and second resonances are quite similar, the third resonance is considerably different. It shows up as two peaks instead of one (the second peak presumably being in the unmeasured region or possibly in the unphysical region).

C. Peierls Fit

An attempt was made to fit all the data of the experiment with seven free parameters by using the assumption of Peierls plus an s-wave term. This fitting was similar to that discussed in Part A of this section with two exceptions: a small amount of electric dipole s-wave

was included with a phase of 0° (the amplitude was the seventh free parameter); and all the data were fit at once instead of each angle separately.

The angular distributions thus become of interest. If we let the amplitudes take the form

$$A_j = a_j e^{i\delta_j}$$

where $j = 0$ refers to the s-wave ($\delta_0 = 0°$) and $j = 1$, 2 or 3 refers to the j^{th} resonance, and let σ_{ij} refer to the term in the cross section proportional to $a_i a_j$, then (18)

$$\sigma_{00} = a_0^2$$

$$\sigma_{01} = 2xa_0a_1\cos\delta_1$$

$$\sigma_{02} = -(1 - 3x^2)a_0a_2\cos\delta_2$$

$$\sigma_{03} = \sqrt{3}x(5x^2 - 3)a_0a_3\cos\delta_3$$

$$\sigma_{11} = \tfrac{1}{2}(5 - 3x^2)a_1^2$$

$$\sigma_{12} = 2xa_1a_2\cos(\delta_1 - \delta_2)$$

$$\sigma_{13} = -\sqrt{3}(1 - 3x^2)a_1a_3\cos(\delta_1 - \delta_3)$$

$$\sigma_{22} = \tfrac{1}{2}(5 - 3x^2)a_2^2$$

$$\sigma_{23} = 2\sqrt{3}x(3 - 2x^2)a_2a_3\cos(\delta_2 - \delta_3)$$

$$\sigma_{33} = \tfrac{3}{2}(1 + 6x^2 - 5x^4)a_3^2$$

where $x = \cos\theta'_{\pi^0}$. The model being used states that the differential cross section is just the sum of the 10 σ_{ij}'s listed above. The values

for a_i and δ_i, $i = 1,2,3$, are obtained from the resonance formulas discussed in Appendix X. In order to give the experimentally determined direction of polarization for the recoil proton and the appropriate interference signs all a_i's are positive and $0° \leq \delta_i \leq 180°$.

The fitting procedure was the same as for the individual angle fits, the experimental resolution again being taken into account.

The results are shown in Figures 10a-c with the same code as for Figures 8a-c. The fit is quite poor at 90° in the region of the second resonance and for all angles at the highest energies measured. Statistically the fit is highly improbable: $\chi^2 = 150$ for 33 degrees of freedom.

The poorness of the 90° fit at the second resonance can be attributed to the fact that fourth order terms in $\cos\theta'_{\pi^0}$ are needed in this region whereas the only source of fourth order terms in the Peierls' model is the third resonance term σ_{33}, which is expected to be small in this region.

The 60° σ_{ij}'s are shown in Figure 11. The σ_{ij}'s at other angles can be obtained from those at 60° by taking into account the functions of x given above in the explicit representation of the σ_{ij}'s. The interference terms between the resonances give a fore-aft asymmetry in the regions of the resonances which was not observed experimentally. The s-wave was introduced to give interference terms which would counteract this effect. It did quite well in this respect at the lower energies, but at the third resonance the phase shifts become such that the sum of the s-wave interference terms change sign, giving a poor fit on the high energy side of this resonance.

Figure 10. Peierls Model Fit

10a. $\theta'_{\pi^0} = 60°$

10b. $\theta'_{\pi^0} = 90°$

10c. $\theta'_{\pi^0} = 120°$

The experimental results are shown as the points. The error flags represent the random and rapidly fluctuating errors; not shown is the 5% uncertainty in absolute normalization. The solid curves show the results of an attempt to fit the data using the assumptions of Peierls plus an s-wave term. The dashed curve in Figure 10a shows the effect of the experimental resolution at 60°. Typical resolution functions are shown at the bottoms of the drawings.

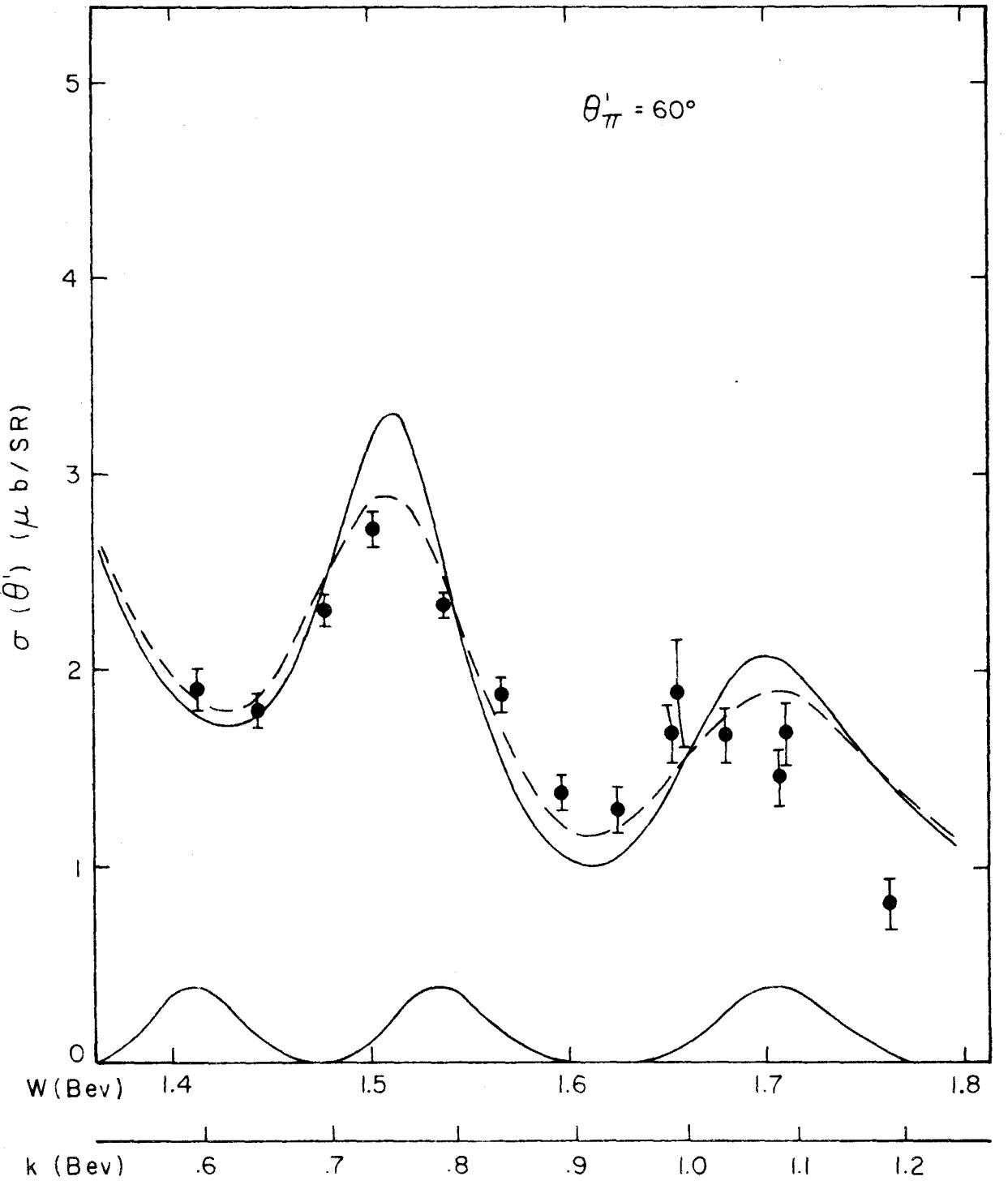

60° Pionic Fit

Figure 10a

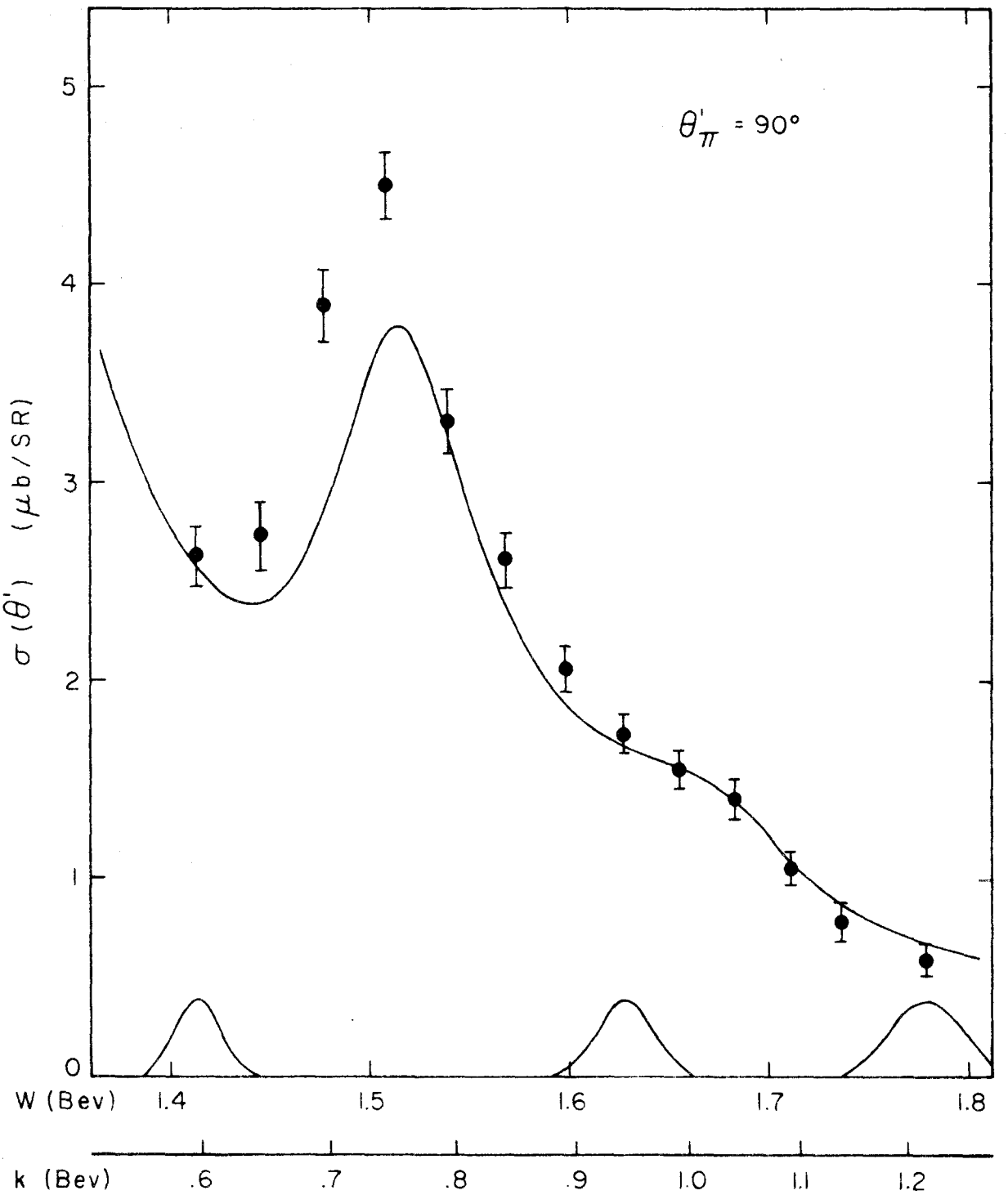

90° Polarlo Fit

Figure 19b

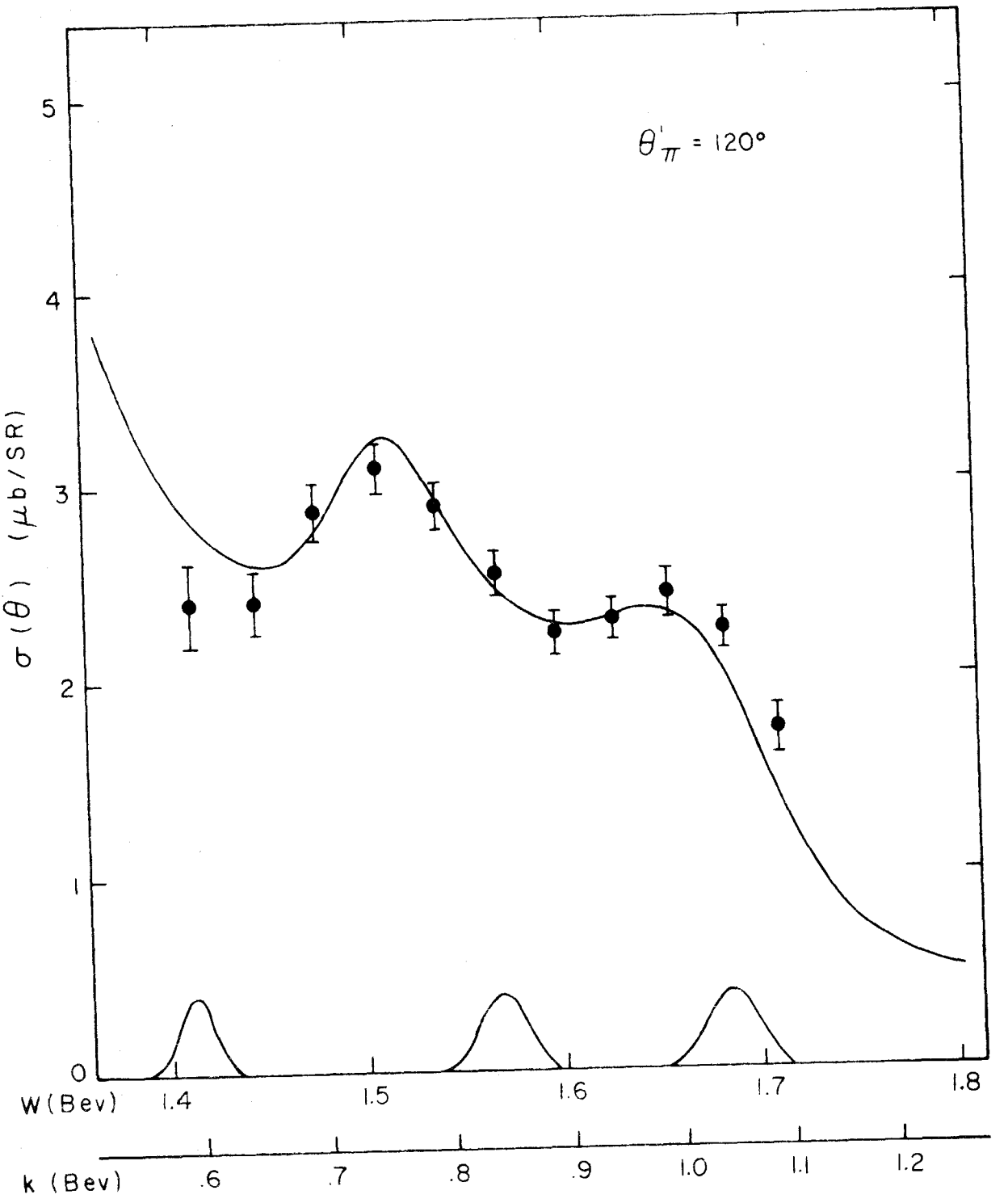

120° Peierls Fit

Figure 10c

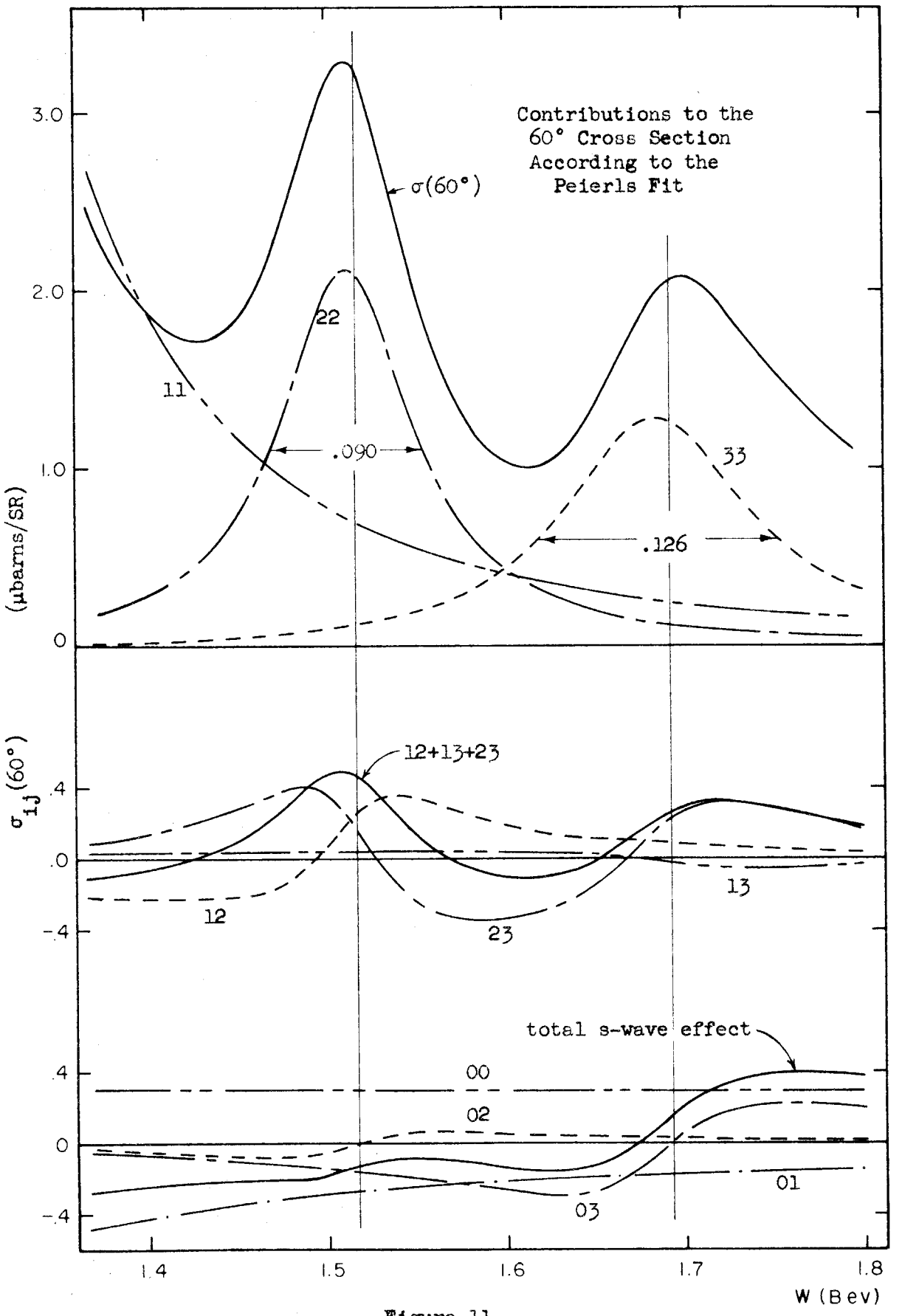
Contributions to the
60° Cross Section
According to the
Peierls Fit
σ(60°)
22
11
.090
33
.126
3.0
2.0
1.0
0
(μbarns/SR)
12+13+23
12
13
23
.4
.0
-.4
total s-wave effect
00
02
01
03
.4
0
-.4
1.4
1.5
1.6
1.7
1.8
W (Bev)

Figure 11

The predictions made by this fit for more forward and backward angles do not agree well with the experiments which have made measurements in these regions. In particular it does not give the small cross sections near 0° observed by Talman, et al. (2). The model predicts the polarization at 90° to be in the direction observed experimentally (the matrix element signs were chosen with this in mind), but it predicts a polarization considerably larger than that observed. In the regions of the second and third resonance peaks the model predicts $P(90°) \sim .88$.

D. Total Cross Section

Too few angles were measured by this experiment to yield reasonable angular distributions without further information. Large third and fourth order terms in $\cos\theta'$ are known to be important in this region, requiring a knowledge of the differential cross section at five or more angles. To supplement the information obtained by this experiment, estimates of σ (30°) and σ (150°) were obtained from Figure 9; in the high energy region σ (150°) was obtained by extrapolating the countours into the unknown region. Estimates of the errors were obtained by examining the stated errors of the previous experiments and the spread between the results of different experiments in the regions of interest.

If the differential cross section is expanded in the series

$$\sigma(\theta) = \sum_{i=o}^{n} a_i (\cos\theta'_{\pi o})^i,$$

then the total cross section is just

$$\sigma_T = a_o + \frac{1}{3} a_2 + \frac{1}{5} a_4 + \cdots .$$

Using the differential cross sections at the five c.m. angles 30°, 60°, 90°, 120°, and 150°, $\sigma(\theta)$ was fit with a quartic in $\cos\theta'_{\pi^0}$ (i.e., n=4). The coefficients, a_i, are linear combinations of the $\sigma(\theta'_i)$ which, when inserted in the equation for σ_T yield

$$\sigma_T = 4\pi \left[\frac{7\sigma\ (30°) + 9\sigma\ (60°) + 13\sigma\ (90°) + 9\sigma\ (120°) + 7\sigma\ (150°)}{45} \right].$$

This equation was used to compute the solid curve of Figure 12; the differential cross sections at 30° and 150° were obtained as described above, while those at 60°, 90°, and 120° were obtained from the unfolded fits of this experiment (solid curves of fig. 8). The greatest contribution to the uncertainty of this determination is the large error associated with σ (150°). Since σ (150°) has only been measured (or extraolated from the measurements) every .1 Bev, the error flags have been shown at .1 Bev intervals.

The dashed curve was computed from the results of the Peierls fit. The chief disagreement between the two methods lies in the region between the two resonances.

Figure 13 compares the total cross section of the Peierls fit with that of the first resonance. The curve in the first resonance region is the total cross section as computed with the formula of Gell-Mann and Watson (7); this is the formula which was used to extrapolate the first resonance contributions for the various fits described earlier in this section. The points are those of McDonald, et al. (3) and are shown to indicate the success of the formula in fitting the experimental data in the first resonance region.

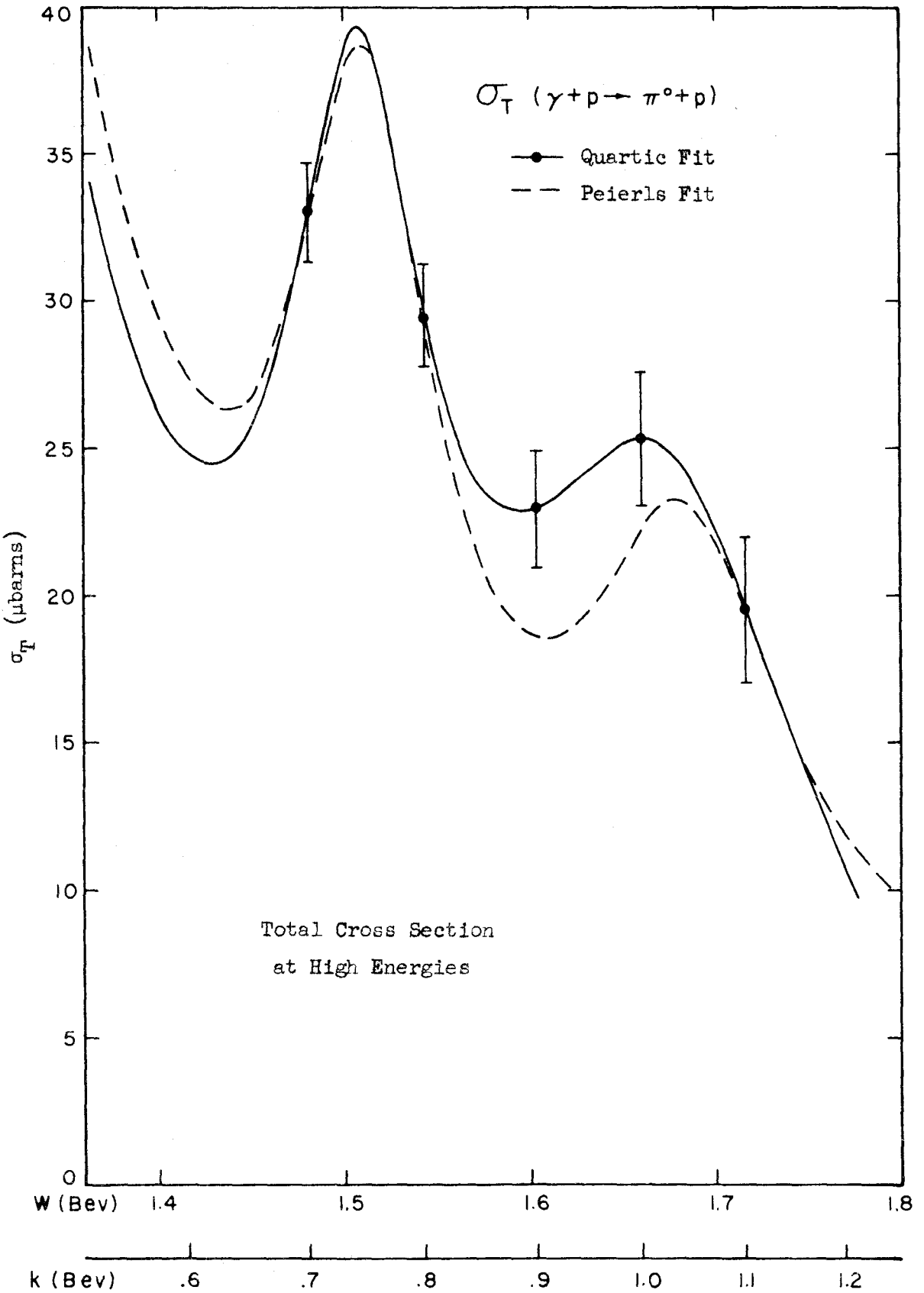
σ_T (γ+p→ π^0+p)
Quartic Fit
Peierls Fit
Total Cross Section
at High Energies
σ_T (μbarns)
40
35
30
25
20
15
10
5
0
W (Bev)
1.4
1.5
1.6
1.7
1.8
k (Bev)
.6
.7
.8
.9
1.0
1.1
1.2

Figure 12

Figure 13. Total Cross Section for $W \leq 1.8$ Bev

The points are those obtained experimentally by McDonald, et al. (3). In the region of the first resonance the curve was obtained from the formula of Gell-Mann and Watson (7) which was used in the fittings to extrapolate the first resonance; at higher energies the curve was computed from the Peierls model fit (dashed curve of fig. 12).

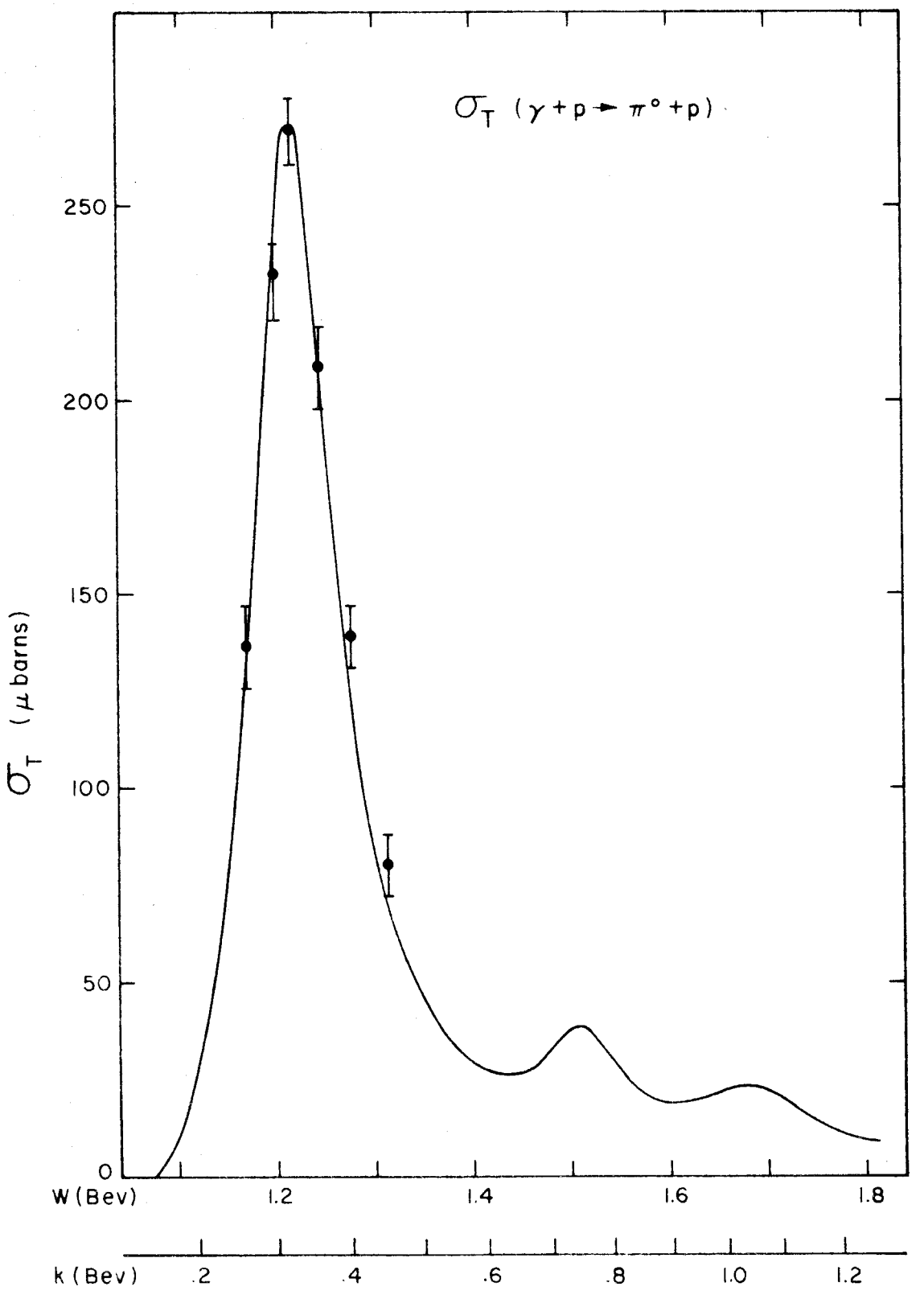
σ_T ($\gamma + p \rightarrow \pi^\circ + p$)
σ_T (μ barns)
0
50
100
150
200
250
W (Bev)
1.2
1.4
1.6
1.8
k (Bev)
.2
.4
.6
.8
1.0
1.2

Figure 15

The difference between the strength of the first resonance and those of the other two is exaggerated by a factor of two by the isotopic spin Clebsch-Gordon coefficients.

E. Comparison with Previous Experiments

The 90° results of earlier experiments performed at Caltech and Cornell are shown in Figure 14. The solid line is the unfolded fit for the 90° data of this experiment; the other curves show the cross sections expected from experiments with various resolution widths if the solid line is taken as the true cross section. The results of the previous experiments, while in substantial agreement with this experiment, are 5 or 10% higher. This discrepancy may be the result of errors in the absolute calibration of the beam, etc., or errors in the absorption and contamination corrections. The one previous experiment which detected both recoil proton and decay photon, and is, therefore, less susceptible to some of the systematic errors, follows the results of this experiment quite closely (taking into account resolution).

The 90° results of the two experiments at Frascati are shown in Figure 15 with the same curves as shown in Figure 14. The data of Cortellessa and Reale do not agree with this experiment or with the other experiments. The spark chamber results are in fair agreement with this experiment, although they too are high by 5 to 10%.

The 60° data is in slightly better agreement with the earlier experiments than is the 90° data. At 120° the previous results are higher than those of this experiment by about 15%. Some of this may be

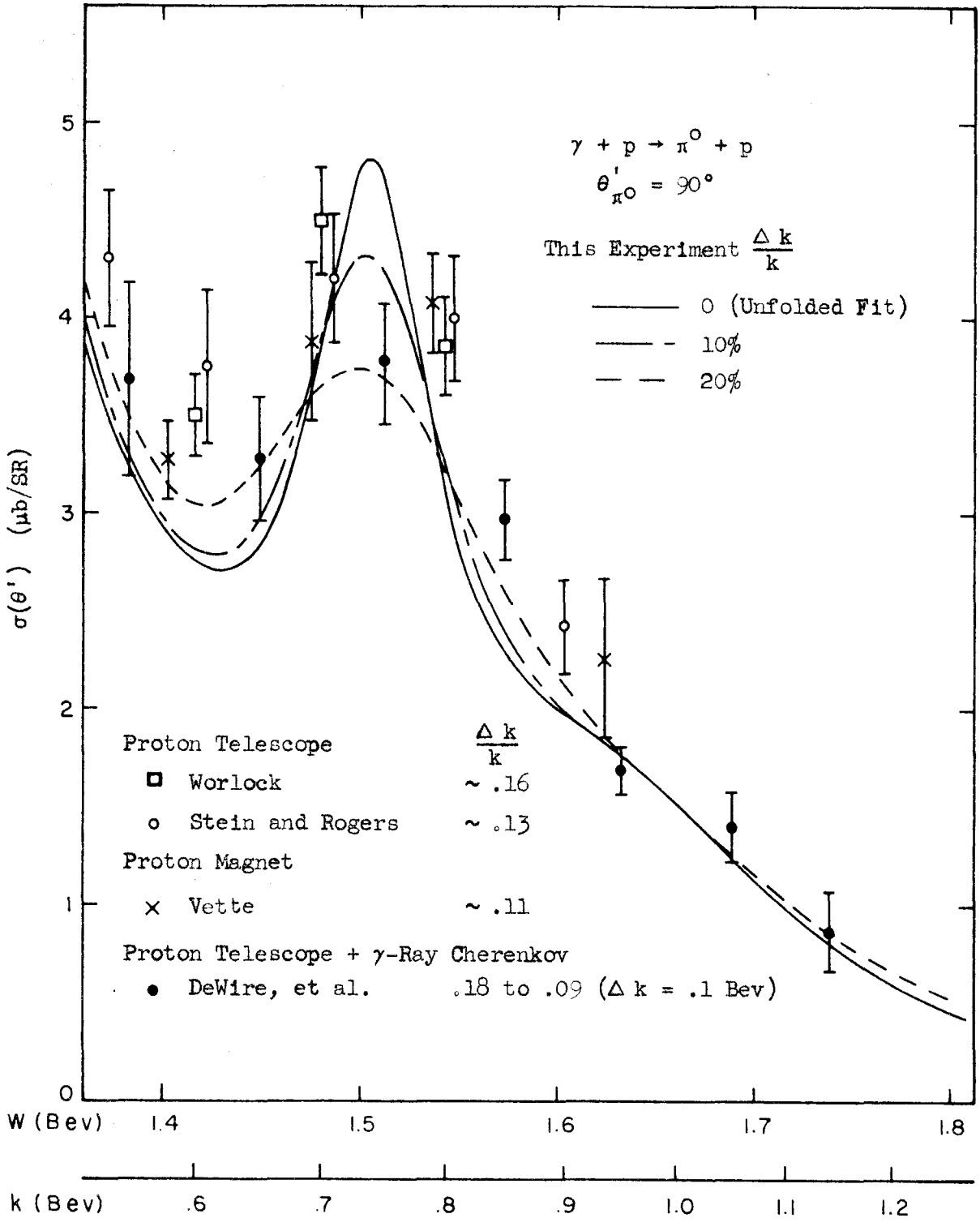

Comparison at 90° with Previous Cornell and Caltech Results

Figure 14

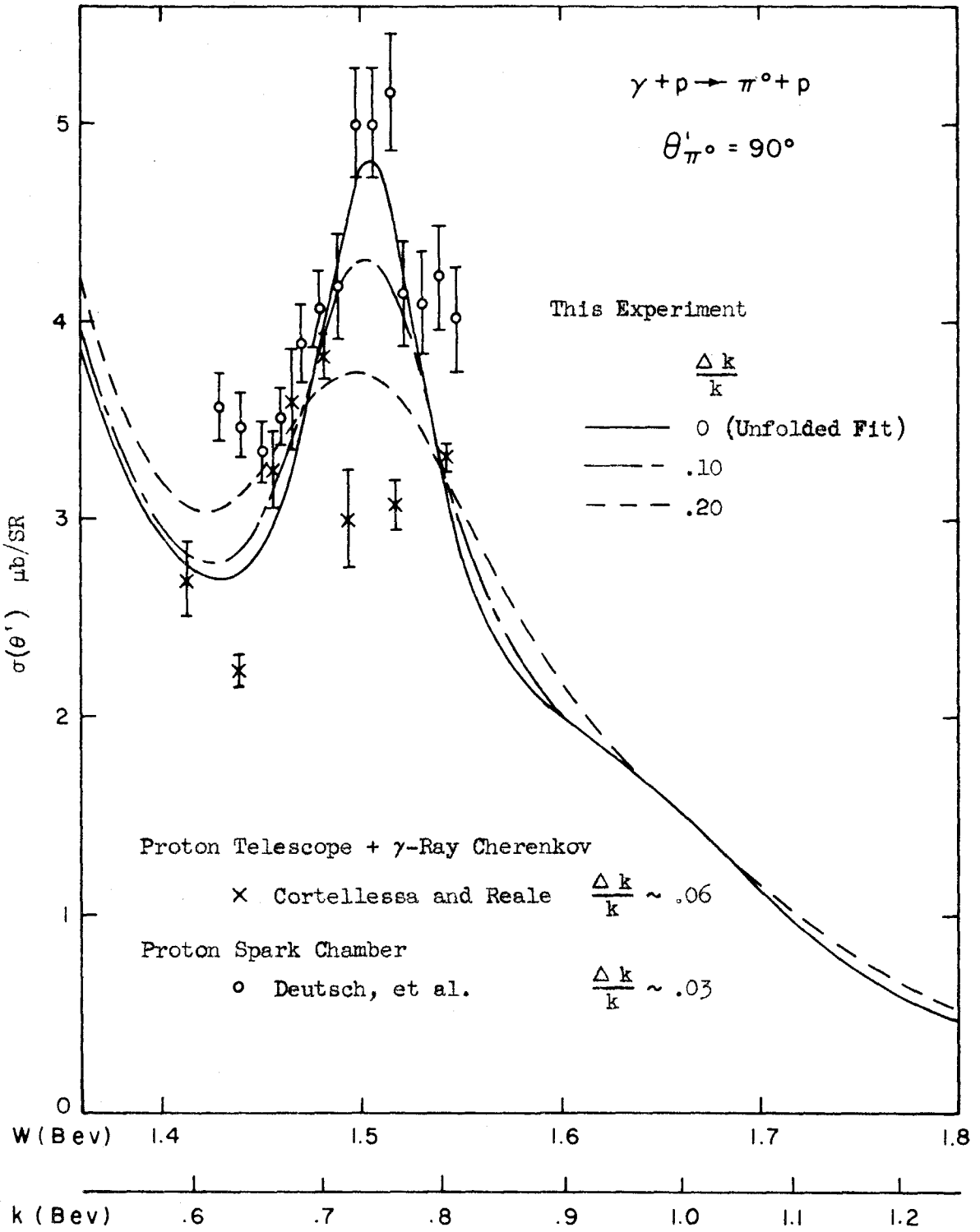

Comparison at 90° with Frascati Results

Figure 15

the result of systematic errors in the earlier experiments such as errors in the corrections for pi pair production or for nuclear absorption in proton telescope absorber.

F. Comparison with Pi-Nucleon Scattering

It was hoped that the positions and widths of the resonances could be obtained from the total cross section. The interference effects of the simple multipole terms vanish when integrated over all angles as a result of the orthogonality properties of the spherical harmonics (terms describing the virtual exchange of particles, however, can affect the total cross section).

The quartic fit total cross section was not used, however, to determine the resonance parameters because it depended on the 30° and 150° cross sections measured by other experiments with large errors. In particular, the third resonance position and width is quite poorly determined by the quartic fit because of the large uncertainty in σ_{150}.

The results of the various fits were examined instead. The resonant energy positions and full widths at half maximum obtained by the various fits are shown in Table 7.

Table 7

Resonance Parameters Obtained by the Various Fits

Fit		W_2	ΔW_2	W_3	ΔW_3
single angle	60°	1.522	.087	1.684	.130
	90°	1.509	.074	1.683	.223
	120°	1.520	.120	1.700	.132
Peierls		1.517	.090	1.692	.126

The large value of ΔW_3 for the single angle 90° fit is the result of the statistical fluctuations masking the weak contribution made to the cross section by the third resonance at this angle. For all but ΔW_3, the values obtained by the Peierls fit lie close to the average of the single angle fits. If this fit had been successful, the resonant positions obtained by it could have been used with errors determined almost completely by the systematic errors in the determination of W (Appendix IV). Since the fit was unsuccessful, the spread in values obtained by the various fits were folded with the systematic errors to give the uncertainties. Table 8 lists the "best" values

Table 8

Summary of the Resonance Parameters

Reaction	1st Res.	2nd Res.	3rd Res.	
$\gamma + p \rightarrow \pi^o + p$	1.238 ± .005	1.517 ± .006	1.692 ± .008	W_{res}
$\pi^\pm + p \rightarrow \pi^\pm + p$	1.232 ± .008	1.522 ± .008	1.698 ± .010	W_{res}
$\gamma + p \rightarrow \pi^o + p$	.112 ± .010	.090 ± .014	.130 ± .018	ΔW
$\pi^\pm + p \rightarrow \pi^\pm + p$	.106 ± .006	.087 ± .012	.100 ± .012	ΔW

obtained by this experiment with their errors. For completeness the first resonance parameters, as obtained by fitting the early experiments with the formula of Gell-Mann and Watson (7), are also shown. These parameters are compared with those obtained from pi-nucleon scattering. The first resonance pi-nucleon parameters were obtained by averaging the

results obtained by the fit of Gell-Mann and Watson to the early pi-nucleon scattering data with those obtained from the more recent data of Lindenbaum and Yuan (5). The parameters for the second and third resonances were obtained by averaging the Saclay (9) and Berkeley (10) results.* The agreement between the parameters as determined by the two types of reactions is quite good with the possible exception of the third resonance width.

We now examine the effects of virtual particle exchange terms. Since these terms contain all angular momentum states, they can interfere with the resonant states and cause the resonant peaks in the total cross sections to shift in energy. The difference between the positions of the π^o and π^+ photoproduction peaks was first calculated for the pion exchange term (see Appendix XIII for a general discussion of the effect and details of the calculation). The results are shown in Table 9 and compared with the observed differences; the agreement is quite good. Calculations of the effects of the ω exchange term were made using Talman's values for the coupling constants (2); as shown in Table 9 this term affects the relative positions of the photoproduction peaks by only one or two Mev.

---

*The position of the high energy pi-nucleon scattering peaks are simply listed in the original papers as the peak energies or energies about which the peaks are centered; in order to compare with the results of this experiment which are listed in terms of resonant energy, the average difference between the resonant and peak energy obtained in the analysis of this experiment was added onto the energies listed by the original papers. The difference between the resonant and peak energies is principally due to the factor $k'^{-2} \alpha \lambda^2$ in the cross section equations.

Table 9

Results of the Virtual Particle Exchange Calculations

Resonance	π exchange $[W_{\pi^o} - W_{\pi^+}]$ calc.	π exchange $[W_{\pi^o} - W_{\pi^+}]$ obsvd.	π exchange $[W_{\pi^o} - W_{\pi N}]$ calc.	π exchange $[W_{\pi^o} - W_{\pi N}]$ obsvd.	ω exchange $[W_{\pi^o} - W_{\pi^+}]$ calc.
1	15	16 ± 6	5	6 ± 10	-2
2	21	21 ± 8	14	-5 ± 10	-2
3	19	17 ± 14	13	-6 ± 13	-1

all energies in Mev

W_{π^o} = position of the π^o photoproduction total cross section peak, etc.

The Watson theorem is useful in relating the photoproduction and scattering peaks; it states that the phases of the photoproduction elements of the S-matrix are just the pi-nucleon phase shifts. On the basis of this theorem both of the photoproduction peaks are expected to be shifted in energy from the pi-nucleon peak (the theorem does not affect the separation of the photoproduction peaks). See Appendix XIII for details. Experimentally the π^o photoproduction peaks are consistent with having the same positions as the scattering peaks, and except for the first resonance the positions of the π^o peaks are not consistent with the predictions based on the Watson theorem (see table 9). Since this theorem is valid only at low energies where multiple pion production is not important ($k \leq .4$ Bev), this inconsistency is not surprising.

Several approximations and assumptions were made in calculating the effects of the virtual particle terms; perhaps the most dubious of

these was the assumption that the second and third resonances were the simple resonances of Peierls (see Section VI for a brief discussion of the possible nature of these "resonances").

VI. CONCLUSIONS AND SUGGESTIONS

This experiment shows the need for using narrow resolution and taking data at frequent intervals of energy if a good understanding of the variation of cross section with energy is to be obtained. Narrow resolution is also needed if good angular distributions are desired, not only because of the basic smearing out of detail, but also because the smearing effects are likely to be different at the different angles due to variation of the resolution width with angle.

The lack of data over a wider angular range limited the conclusions and results which could be extracted from the experiment. Being unable to obtain an angular distribution with the data of this experiment resulted in an uncertainty in the total cross section which prevented the comparison with pi-nucleon scattering from being as precise as desired. The lack of a good angular distribution also prevented not only phase shift analyses, but even an analysis which might have indicated the important terms of the cross section.

There was sufficient data, however, to severely test specific models. The simple model of Peierls was the only one studied in detail. Even with the aid of a small amount of s-wave this model was unable to fit the data well; in particular it could not fit the large 90° cross section in the second resonance region. Thus it would seem that this simple model is inadequate and a different model must be found. There is a great multitude of terms from which one may choose to explain the behavior: simple multipole terms, pole terms from virtual meson exchange, nucleon Born terms, etc.

Some indications of pole terms being important have been found in two different experiments. A recent experiment at Illinois (35) carefully measured single π^+ photoproduction below the first resonance. The results do not agree with the predictions of the CGLN theory; the discrepancy can be explained by assuming the ρ pole term to be important. The results depend strongly on the small amplitude phase shifts which are not all well known, however. Talman (2) finds that his small angle data, together with the wide angle data of other experiments, can be fit qualitiatively if he assumes an ω pole term contributes strongly to the cross section. Similar fits can also be made, however, using the multipoles of Peierls plus an s-wave term if one does not constrain the amplitudes to be those obtained by the resonance formulas. Thus, it would seem that while pole terms may be needed, even at low energies, great care must be taken because their effects may be counterfeited by simple multipole terms, and vice versa.

The nucleon Born terms, which are believed by theoreticians to be important, do not appear to be present in single π^o photoproduction in the energy region of this experiment. In particular, the term corresponding to the proton anomalous magnetic moment gives a cross section at backward pion angles which is an order of magnitude larger than experimentally observed. Possibly the magnitudes of these terms can be reduced by theoretical arguments based on Regge poles. It is interesting to note that the fore-aft asymmetry caused by Peierls' interference terms, which was then corrected for in a rather unsatisfactory manner (didn't work above the third resonance) by s-wave interference, could have been better corrected for by the asymmetry of the Born terms (reduced by an appropriate factor).

A recent $\pi^- p$ elastic scattering experiment at Berkeley (36) has produced several angular distributions in the region of the second and third resonances. Sixth order terms in $\cos\theta'$ are necessary to fit the data. Their analysis indicates that there is probably no single term giving a predominant contribution to the peak commonly known as the second resonance. A phase shift analysis gave many sets of possible phases for the various amplitudes; in none of these sets does the $D_{3/2}$ (Peierls' choice for the second resonance) phase become greater than 30°. Their data also indicate a mixture of parity for the third resonance, with both $D_{5/2}$ and $F_{5/2}$ states contributing. On the basis of this scattering experiment it would seem that these two higher energy peaks in the cross sections are not the simple resonances as thought previously; the names "second resonance" and "third resonance" are thus misleading, and one must interpret the term "resonance" when so used as merely denoting a peak in the cross section.

In order to further interpret the pi-nucleon interactions at these energies several angular distributions for single π^o production would be useful. If sufficiently detailed, these distributions could also be used to give information on the various coupling constants of the ρ and ω particles and the importance of the Born terms.

For these reasons experiments similar to the one described in this thesis should be performed at other angles. In particular the backward pion angle region should be investigated. In this region the proton comes out at forward angles in the laboratory with a very high momentum. This high momentum has advantages and disadvantages: for example, the beam cannot produce other particles from hydrogen with such momentum

(see fig. A12); on the other hand the spectrometer must be redesigned and particle separation becomes difficult. It should be possible to obtain data at very small proton angles, perhaps even at the interesting angle of 0° (the contributions to the cross sections at 0° and 180° are considerably simplified, making them more amenable to analysis). Intermediate angles could also be studied to give a good angular distribution.

For $\theta'_{\pi^o} < 45°$ the protons have such low energies that the reaction is probably more profitably studied by observing the π^o decay products, as did Talman, but with a narrower resolution.

The experimental conditions can be considerably improved for future experiments. The mylar cup of the hydrogen target can be made thinner, reducing the empty target background. The target could also be redesigned to give less slowing and multiple scattering of the protons. Investigations should be made of the below threshold background; hopefully, it can be reduced considerably once its source is understood. Narrower resolution without loss of counting rate can be obtained by using several thin momentum defining counters simultaneously. Faster electronics will help both in the separation of particles and in the elimination of accidentals. The higher beam intensity expected in the near future can be used to reduce the uncertainties due to counting statistics and to obtain more data points in the same amount of running time.

APPENDIX I

Tables of Results

Table A1 lists the proton counting rates and corrections, where

F = full target counts (proton plus γ-ray for points 1 - 9; proton only for points 10 - 40)/100 BIPS,

C_X = counts/100 BIPS from the complex nuclei of the target structure,

C_{BTh} = estimated counts/100 BIPS from the below threshold or wide angle nuclear scattering background,

C_{Pr} = estimated counts/100 BIPS from pi pair production, and

$C = F - C_X - C_{BTh} - C_{Pr}$.

Table A2 lists the various factors used to obtain the differential cross sections from the counting rates; it also lists C as defined above and the resulting experimental cross sections. The symbols have the following meanings:

PT = arbitrary designation of each experimental point (same as for table A1),

MAG = position of the magnetic spectrometer,

ANG = θ'_{π^o} (degrees),

W = median total center of mass energy (Bev),

k = median incident laboratory photon energy (Bev),

E_o = bremsstrahlung end point energy (Bev),

U = total energy in beam (10^{11}Bev/100 BIPS),

$\overline{B}$ = average value of photon spectrum factor $B(k,E_o)$,

$N(k) = U\overline{B}/E_o k$

Table A1

Counting Rates for Cross Section Points

Point Number	θ'_{π^o}	k	F	C_x	C_{BTh}	C_{Pr}	C
1	60°	.594	28.6 ± 1.6	0.4 ± 0.3	.2 ± .2	.0	31.1 ± 1.8[a]
2	60°	.639	28.0 ± 1.2	0.5 ± 0.4	.2 ± .2	.0	28.5 ± 1.4[a]
3	60°	.692	40.0 ± 1.3	0.5 ± 0.4	.2 ± .2	.0	39.3 ± 1.4
4	60°	.730	45.3 ± 2.7	0.6 ± 0.4	.2 ± .2	.0	44.5 ± 2.7
5	60°	.733	48.1 ± 1.6	0.6 ± 0.4	.2 ± .2	.0	47.3 ± 1.7
6	60°	.790	40.8 ± 1.0	0.6 ± 0.3	.2 ± .2	.0	40.0 ± 1.1
7	60°	.837	32.2 ± 1.4	0.6 ± 0.4	.1 ± .1	.0	31.5 ± 1.5
8	60°	.888	23.1 ± 1.2	0.5 ± 0.4	.1 ± .1	.0	22.5 ± 1.3
9	60°	.936	21.2 ± 1.9	0.4 ± 0.4	.1 ± .1	.1 ± .1	20.6 ± 1.9
10	60°	.985	41.1 ± 1.4	11.3 ± 1.4	3.5 ± 1.2	.1 ± .1	26.2 ± 2.3
11	60°	.989	18.9 ± 1.3	5.6 ± 1.1	1.4 ± .4	.0	11.9 ± 1.8
12	60°	1.033	39.5 ± 1.2	10.6 ± 1.4	3.3 ± 1.2	.1 ± .1	25.5 ± 2.2
13	60°	1.082	34.6 ± 1.1	9.9 ± 1.5	3.1 ± 1.2	.1 ± .1	21.5 ± 2.2
14	60°	1.088	16.8 ± 0.5	5.0 ± 0.8	1.3 ± .4	.0	10.5 ± 1.0
15	60°	1.185	10.6 ± 0.5	4.5 ± 0.4	1.1 ± .4	.0	5.0 ± 0.8
16	90°	.595	118.3 ± 3.4	27.3 ± 2.9	2.7 ± 2.7	.7 ± .5	87.6 ± 5.3
17	90°	.644	115.7 ± 4.2	24.1 ± 2.7	2.6 ± 2.6	1.0 ± .8	88.0 ± 5.7
18	90°	.694	48.6 ± 1.6	6.1 ± 0.9	.7 ± .7	.0	41.8 ± 2.0
19	90°	.743	53.4 ± 1.7	5.2 ± 0.6	.7 ± .7	.0	47.5 ± 1.9
20	90°	.793	39.2 ± 1.6	4.5 ± 0.6	.6 ± .6	.0	34.1 ± 1.8
21	90°	.841	31.1 ± 1.2	3.9 ± 0.5	.6 ± .6	.0	26.6 ± 1.4
22	90°	.891	24.4 ± 0.8	3.4 ± 0.4	.6 ± .6	.0	20.4 ± 1.1
23	90°	.942	20.0 ± 0.7	3.0 ± 0.4	.5 ± .5	.0	16.5 ± 1.0
24	90°	.989	17.6 ± 0.6	2.6 ± 0.4	.5 ± .5	.0	14.5 ± 0.9
25	90°	1.039	15.6 ± 0.7	2.3 ± 0.3	.5 ± .5	.0	12.8 ± 0.9
26	90°	1.088	11.4 ± 0.5	1.9 ± 0.3	.4 ± .4	.0	9.1 ± 0.7
27	90°	1.091	13.9 ± 0.9	2.5 ± 0.5	.4 ± .4	.4 ± .3	10.6 ± 1.1
28	90°	1.137	8.8 ± 0.5	1.6 ± 0.3	.4 ± .4	.0	6.8 ± 0.7
29	90°	1.217	7.0 ± 0.5	1.2 ± 0.2	.4 ± .4	.1 ± .1	5.3 ± 0.7
30	120°	.595	44.6 ± 3.0[b]	8.6 ± 0.9	.8 ± .8	.0	35.2 ± 3.2
31	120°	.645	42.5 ± 1.9	6.9 ± 0.9	.7 ± .7	.5 ± .5	34.4 ± 2.3
32	120°	.694	46.0 ± 1.7	5.6 ± 0.9	.7 ± .7	.1 ± .1	39.6 ± 2.1
33	120°	.744	46.9 ± 1.4	4.7 ± 0.7	.7 ± .7	.1 ± .1	41.4 ± 1.7
34	120°	.793	42.4 ± 1.3	4.1 ± 0.7	.6 ± .6	.1 ± .1	37.6 ± 1.6
35	120°	.843	36.4 ± 1.2	3.6 ± 0.6	.6 ± .6	.1 ± .1	32.1 ± 1.5
36	120°	.892	31.5 ± 1.0	3.2 ± 0.6	.6 ± .6	.2 ± .2	27.5 ± 1.3
37	120°	.942	31.3 ± 1.0	2.9 ± 0.6	.5 ± .5	.2 ± .2	27.7 ± 1.3
38	120°	.991	31.7 ± 1.5	2.6 ± 0.5	.5 ± .5	.2 ± .2	28.4 ± 1.7
39	120°	1.041	28.9 ± 0.8	2.5 ± 0.6	.5 ± .5	.2 ± .2	25.7 ± 1.1
40	120°	1.090	22.4 ± 1.2	2.4 ± 0.8	.4 ± .4	.2 ± .2	19.4 ± 1.5

[a] Corrected for lead glass geometric inefficiency

[b] Obtained from pi pair extrapolation of E_o data

TABLE A2

CALCULATION OF DIFFERENTIAL CROSS SECTIONS FROM CORRECTED PROTON COUNTING RATE

PT	MAG	ANG	W	k	E_o	U	$\bar{B}$	N(k)	p_o	dp/dp_o	G	A	κ	C	ΔC	$\bar{\sigma}$	Δσ	PT
1	M	60	1.412	0.594	0.703	0.974	0.871	2.033	0.354	0.759	4.08	0.926	16.35	31.1	1.8	1.90	0.11	1
2	M	60	1.442	0.639	0.703	0.974	0.777	1.686	0.386	0.810	4.27	0.893	15.94	28.5	1.4	1.79	0.09	2
3	M	60	1.476	0.692	0.803	0.956	0.873	1.502	0.415	0.848	4.46	0.911	17.06	39.3	1.4	2.30	0.08	3
4	M	60	1.500	0.730	0.803	0.956	0.792	1.292	0.440	0.874	4.62	0.921	16.75	44.5	2.7	2.66	0.16	4
5	M	60	1.502	0.733	0.853	0.949	0.874	1.326	0.440	0.874	4.62	0.921	17.18	47.3	1.7	2.75	0.10	5
6	M	60	1.537	0.790	0.904	0.942	0.866	1.143	0.471	0.894	4.84	0.928	17.15	40.0	1.1	2.33	0.06	6
7	M	60	1.566	0.837	0.954	0.935	0.862	1.009	0.496	0.909	5.02	0.933	16.89	31.5	1.5	1.87	0.09	7
8	M	60	1.596	0.888	1.004	0.927	0.852	0.886	0.520	0.922	5.20	0.936	16.42	22.5	1.3	1.37	0.08	8
9	M	60	1.624	0.936	1.054	0.921	0.843	0.787	0.544	0.933	5.38	0.939	16.02	20.6	1.9	1.29	0.12	9
10	M	60	1.652	0.985	1.104	0.916	0.836	0.704	0.567	0.943	5.56	0.942	15.63	26.2	2.3	1.68	0.15	10
11	H	60	1.654	0.989	1.104	1.233	0.858	0.969	0.565	0.938	5.56	0.887	6.33	11.9	1.8	1.88	0.28	11
12	M	60	1.679	1.033	1.155	0.911	0.831	0.635	0.589	0.950	5.73	0.944	15.25	25.5	2.2	1.67	0.14	12
13	M	60	1.706	1.082	1.205	0.907	0.822	0.572	0.611	0.956	5.90	0.945	14.80	21.5	2.2	1.45	0.15	13
14	H	60	1.709	1.088	1.205	1.267	0.847	0.819	0.609	0.951	5.91	0.892	6.26	10.5	1.0	1.68	0.16	14
15	H	60	1.762	1.185	1.305	1.298	0.831	0.697	0.652	0.960	6.25	0.895	6.11	5.0	0.8	0.82	0.13	15
16	M	90	1.413	0.595	0.703	0.974	0.884	2.060	0.557	0.939	4.15	0.941	33.33	87.6	5.3	2.63	0.16	16
17	M	90	1.445	0.644	0.753	0.965	0.883	1.757	0.596	0.952	4.31	0.944	32.19	88.0	5.7	2.73	0.18	17
18	H	90	1.477	0.694	0.753	1.096	0.847	1.776	0.634	0.956	4.47	0.894	10.76	41.8	2.0	3.89	0.19	18
19	H	90	1.508	0.743	0.803	1.116	0.840	1.570	0.672	0.964	4.62	0.896	10.55	47.5	1.9	4.50	0.18	19
20	H	90	1.539	0.793	0.853	1.136	0.832	1.396	0.709	0.970	4.78	0.898	10.31	34.1	1.8	3.31	0.17	20
21	H	90	1.568	0.841	0.904	1.156	0.832	1.265	0.744	0.975	4.92	0.899	10.17	26.6	1.4	2.61	0.14	21
22	H	90	1.598	0.891	0.954	1.176	0.818	1.132	0.781	0.980	5.08	0.899	9.89	20.4	1.1	2.06	0.11	22
23	H	90	1.627	0.942	1.004	1.196	0.801	1.013	0.816	0.982	5.23	0.899	9.55	16.5	1.0	1.73	0.10	23
24	H	90	1.654	0.989	1.054	1.215	0.797	0.929	0.850	0.985	5.37	0.899	9.38	14.5	0.9	1.55	0.10	24
25	H	90	1.682	1.039	1.104	1.233	0.786	0.845	0.883	0.987	5.51	0.899	9.13	12.8	0.9	1.40	0.10	25
26	H	90	1.709	1.088	1.155	1.250	0.777	0.773	0.916	0.988	5.65	0.899	8.91	9.1	0.7	1.02	0.08	26
27	H	90	1.711	1.091	1.205	1.267	0.863	0.832	0.916	0.988	5.66	0.899	9.59	10.6	1.1	1.11	0.11	27
28	H	90	1.736	1.137	1.205	1.267	0.762	0.705	0.949	0.989	5.79	0.899	8.62	6.8	0.7	0.79	0.08	28
29	H	90	1.779	1.217	1.305	1.298	0.811	0.663	1.000	0.990	6.02	0.899	8.88	5.3	0.7	0.60	0.08	29
30	H	120	1.413	0.595	0.653	1.056	0.862	2.343	0.703	0.969	4.09	0.898	14.66	35.2	3.2	2.40	0.22	30
31	H	120	1.446	0.645	0.723	1.084	0.876	2.036	0.754	0.977	4.23	0.899	14.26	34.4	2.3	2.41	0.16	31
32	H	120	1.477	0.694	0.753	1.096	0.851	1.784	0.804	0.981	4.36	0.899	13.81	39.6	2.1	2.87	0.15	32
33	H	120	1.509	0.744	0.803	1.116	0.845	1.578	0.853	0.985	4.50	0.899	13.41	41.4	1.7	3.09	0.13	33
34	H	120	1.539	0.793	0.853	1.136	0.838	1.406	0.900	0.988	4.63	0.899	13.02	37.6	1.6	2.89	0.12	34
35	H	120	1.569	0.843	0.904	1.156	0.832	1.262	0.947	0.988	4.76	0.899	12.66	32.1	1.5	2.54	0.12	35
36	H	120	1.598	0.892	0.954	1.176	0.826	1.142	0.993	0.990	4.89	0.899	12.35	27.5	1.3	2.23	0.11	36
37	H	120	1.627	0.942	1.004	1.196	0.819	1.036	1.039	0.991	5.02	0.899	12.04	27.7	1.3	2.30	0.11	37
38	H	120	1.655	0.991	1.054	1.215	0.812	0.944	1.084	0.992	5.15	0.899	11.75	28.4	1.7	2.42	0.14	38
39	H	120	1.683	1.041	1.104	1.233	0.804	0.862	1.129	0.993	5.27	0.899	11.46	25.7	1.1	2.24	0.10	39
40	H	120	1.710	1.090	1.155	1.250	0.799	0.794	1.173	0.993	5.40	0.899	11.22	19.4	1.5	1.73	0.13	40

p_o = central momentum of spectrometer (Bev/c),

p = proton momentum at production (Bev/c)

$G = \left(\frac{\partial \Omega'}{\partial \Omega}\right)_k \left(\frac{\partial k}{\partial p}\right)_\theta$

A = correction for proton absorption and counter C3 inefficiency,

$\kappa = N_H \left(\frac{\Delta p}{p_o} \Delta \Omega\right) N(k)\, p_o \frac{\partial p}{\partial p_o} GA$ (cts/100 BIPS/μbarn)

where

$N_H = 3.04 \times 10^{23}$ effective free protons in target/cm^2

and $\frac{\Delta p_o}{p_o} \Delta \Omega$ = spectrometer constant

$= 2.61 \times 10^{-4}$ SR Medium Energy Position

$= .823 \times 10^{-4}$ SR High Energy Position,

C = corrected number of counts/100 BIPS (see table A1), and

$\bar{\sigma} = C/\kappa$ (μbarns/SR); the bar reflects the fact that these values are averages over energy because of the finite experimental resolution.

APPENDIX II

Agreement Between Runs

Several runs were made at each experimental point. For most of the points runs were taken on at least two separate occasions. This gave a consistency check on the equipment and on any possible drifts.

The fluctuations of the individual runs about the mean for each point were checked to determine whether they were consistent with those expected on a statistical basis. This was done by evaluating χ^2 for each run:

$$\chi^2 = \sum_{i=1}^{n} \left[\frac{C_i - \overline{C}}{\sigma_i} \right]^2$$

where C_i is the counting rate of the i^{th} run, $\overline{C}$ is the average counting rate of the n runs taken at the particular point, and

$$\sigma_i = \frac{C_i}{\sqrt{N_i}}$$

where N_i is the number of counts obtained during the i^{th} run.

For a given number of degrees of freedom (in this case n - 1) statistical tables can be used to give the probability (chi-squared probability) that the values of χ^2 be greater than the experimental value. This probability was evaluated for all the HE position points and for those ME position points with large fluctuations.

Similar calculations were performed for those points which had runs taken on separate occasions. The runs were separated into their natural groups and the averages of the individual groups compared with

the grand average for the point. Histograms of the distributions of the chi-squared probability for the HE position points are shown in Figure A1.

The histograms are consistent with the fluctuations of the runs and groups of runs being completely due to the statistical nature of the measurements. If anything, there are slightly fewer points with low probabilities than one might have expected; this is also true of the ME position points. No temporal drifts were observed.

Unfortunately, each position had two or three points with probabilities less than 1%. For some of these points enough data was taken on different occasions to allow one to pick out the bad runs. For the other points with low probabilities ($< 10\%$) the counting rate error flags were increased to reflect the large fluctuations.

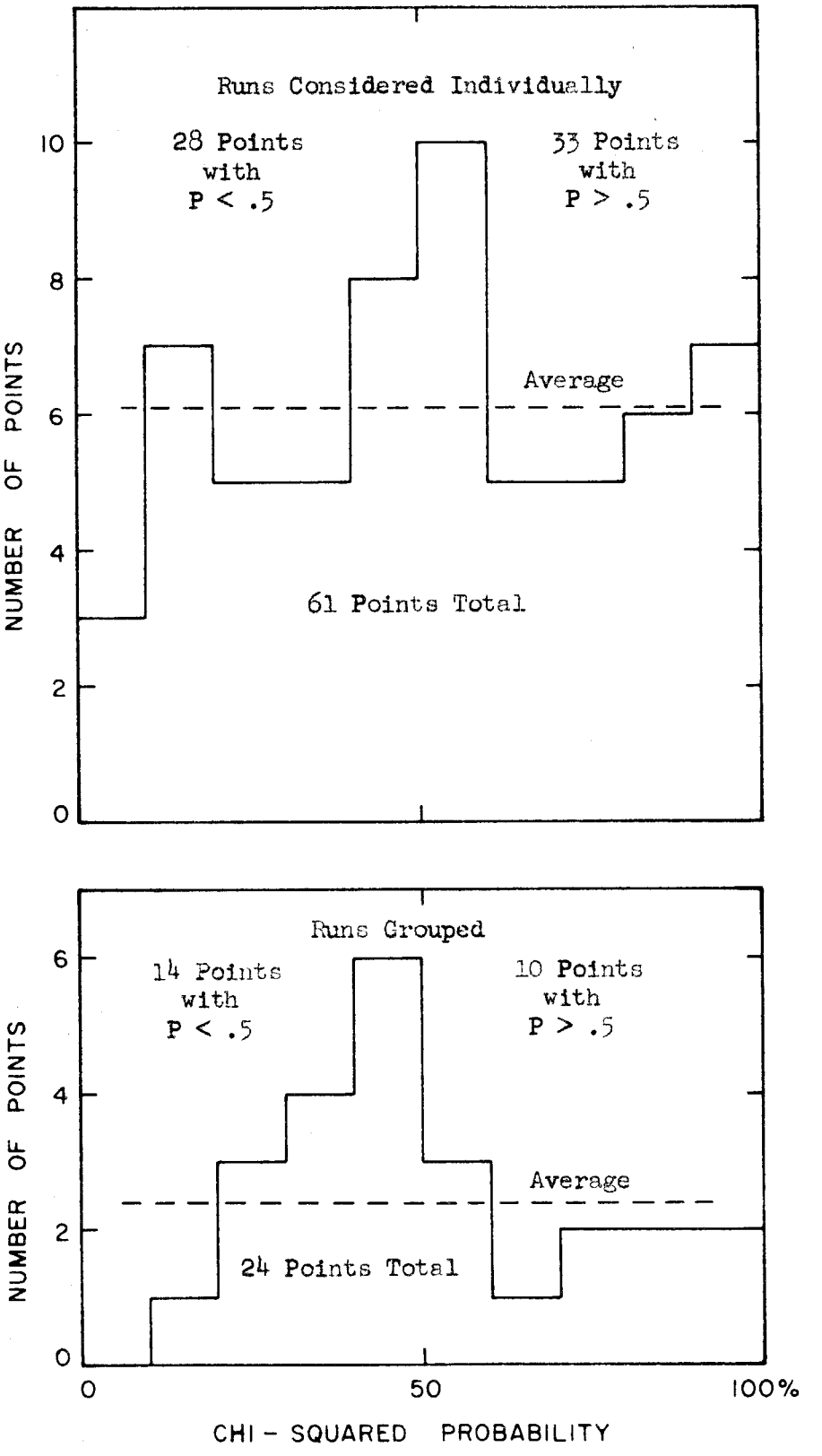

Histograms of the Chi-Squared Probability for the HE Position Runs

Figure A1

APPENDIX III

Empty Target Backgrounds

"Empty" target runs were taken with hydrogen gas instead of liquid in the target in order to determine the contributions to the counting rates made by the beam striking the mylar cup and other parts of the target structure. Such contributions come mainly from complex nuclei and presumably vary smoothly from point to point due to the smearing effect of the Fermi momentum of the nucleons. For this reason the runs were generally taken at every second or third point and the results interpolated for the other points.

There was still a small amount of hydrogen present in the target for these runs, both as gas and as a constituent of the Mylar. The rapid fluctuations of the contributions from the hydrogen can be extracted as follows: let

F and E = the full and empty target counting rates,

σ_f and σ_e = the effective number of gm/cm^2 of hydrogen in the beam for the two types of runs,

c_{H_2} = the counting rate from 1 gm/cm^2 hydrogen, and

C_x = the counting rate from the complex nuclei.

Then

$$F = \sigma_f \, c_{H_2} + C_x$$

$$E = \sigma_e \, c_{H_2} + C_x$$

which can be solved for C_x:

$$C_x = \frac{E - \frac{\sigma_e}{\sigma_f} F}{1 - \frac{\sigma_e}{\sigma_f}} .$$

For this experiment $\frac{\sigma_e}{\sigma_f} \sim 3\%$.

The hydrogen counting rate can be expressed as

$$c_{H_2} = \frac{F - C_x}{\sigma_f} .$$

The values of C_x so obtained were plotted, and smooth curves were drawn through them for each center of mass angle studied and for the points used for consistency checks. These curves were used to give values of C_x for the various points including those at which empty target runs were not taken. The values obtained for the cross section points are listed in Table A1.

In general it was found that the contributions from the hydrogen remaining in the "empty" target were not enough to cause large fluctuations, and results obtained by passing smooth curves through the values of E did not differ appreciably from those computed by the formalism above. There were two general exceptions to this: the proton plus γ-ray data for which the majority of empty target counts were from the residual hydrogen; and the photon energy consistency check curves (Appendix IV) in the region of the π^o step where the hydrogen rates are changing quite rapidly.

APPENDIX IV

Photon Energy Consistency Checks

These checks were made by taking runs with fixed spectrometer angle and momentum and variable E_o. The position of the step in the counting rate due to single π^o photoproduction served to test the consistency between the photon energy determined by the magnet settings, E_o determined by integrating the magnetic field of the synchrotron, and the shape of the photon spectrum near the endpoint obtained by Boyden (1). The runs also gave a rough check on the resolution width.

If we ignore Compton scattering (presumably only a few per cent) and keep E_o low enough to avoid pi pair production, then $C(E_o)$, the counting rate from hydrogen (corrected for the wide angle scattering contamination) obtained at a particular magnet setting with bremsstrahlung end point E_o, obeys the following proportionality:

$$C(E_o) \propto \int_o^{E_o} R(k)\sigma(k,\theta')N(k)dk$$

where

$R(k)$ = the relative efficiency of the spectrometer to detect a recoil proton produced by π^o production by a photon of energy k (see Appendix IX),

$N(k)$ = the energy density of photons, and

$\sigma(k,\theta')$ = the center of mass differential cross section for π^o photoproduction at energy k.

Using preliminary results for $\sigma(k,\theta')$, the integral was evaluated for the various values of E_o used at each spectrometer setting; a statistically best value for the constant of proportionality was obtained for

the experimental points at each setting. Other curves were similarly obtained under the assumption that the magnet settings were in error such that the effective value of the photon energy was Δ more than the nominal value; several values of Δ were tried. In each case a value for χ^2 was obtained, and from these a best value for Δ was found. The experimental points and their best fits are shown in Figures A2a-d; for convenience they have been normalized to give $C(E_o) = 1$ at the highest E_o experimental point. The resolution widths calculated for the two settings at which several values of E_o were run appear to agree well with the experimental widths.

From these fits one can obtain a weighted average for Δ :

$$\overline{\Delta} = - .007 \pm .002 \text{ Bev.}$$

The sign corresponds to the magnet being set to a lower value of k (lower momentum or smaller angle) than the nominally accepted value; or to the true value of E_o being higher than that given by the magnetic field integrator; or to the photon spectrum having a sharper cutoff near E_o than obtained by Boyden.

Since the data were so sparse that detailed variations of Δ with angle and energy could not be determined, it was assumed that Δ was proportional to k with a proportionality constant independent of θ' :

$$\Delta = \alpha k .$$

The best value for α is

$$\alpha = - .008 \pm .003$$

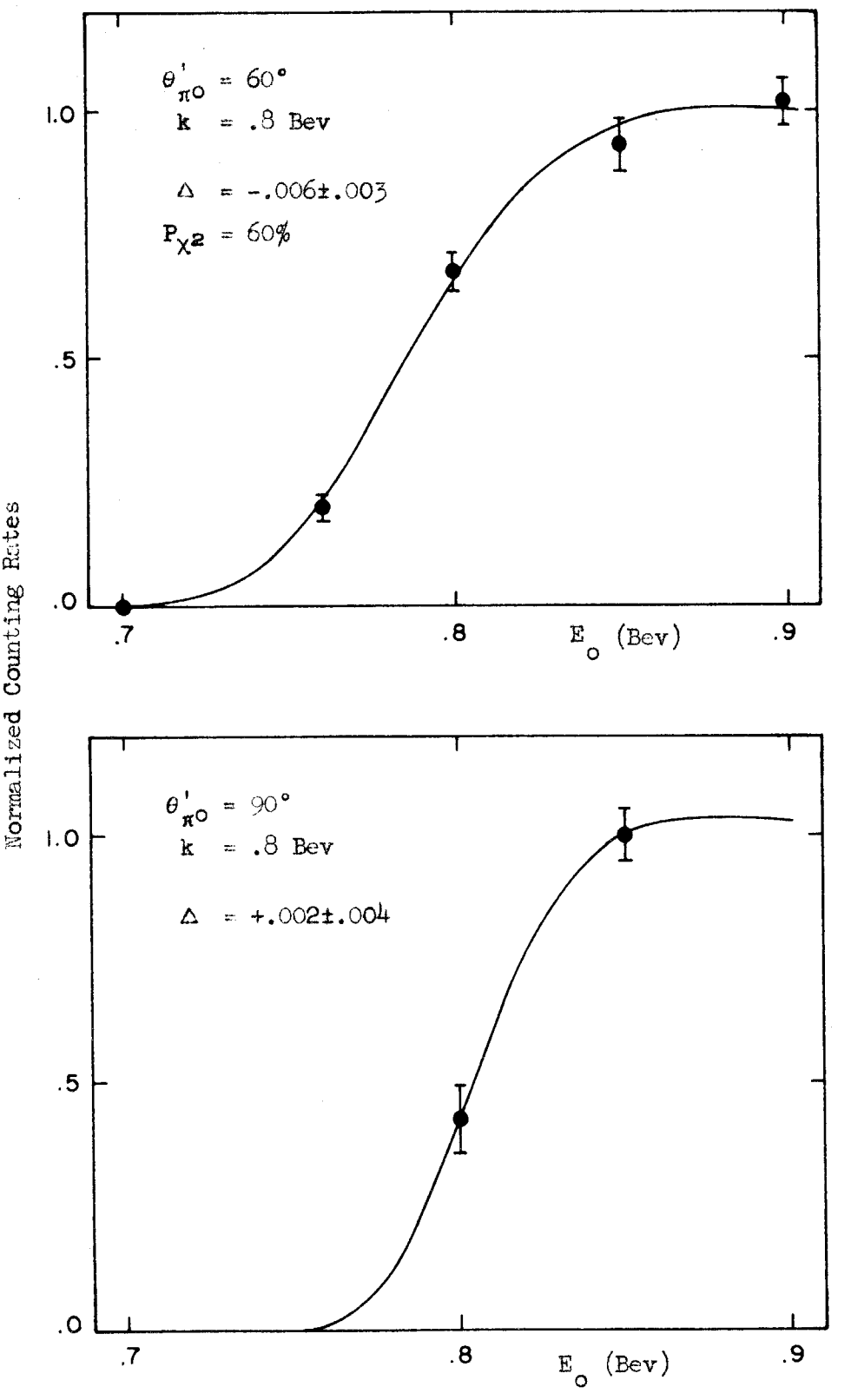

Photon Energy Consistency Check Results

Figure A2 a,b

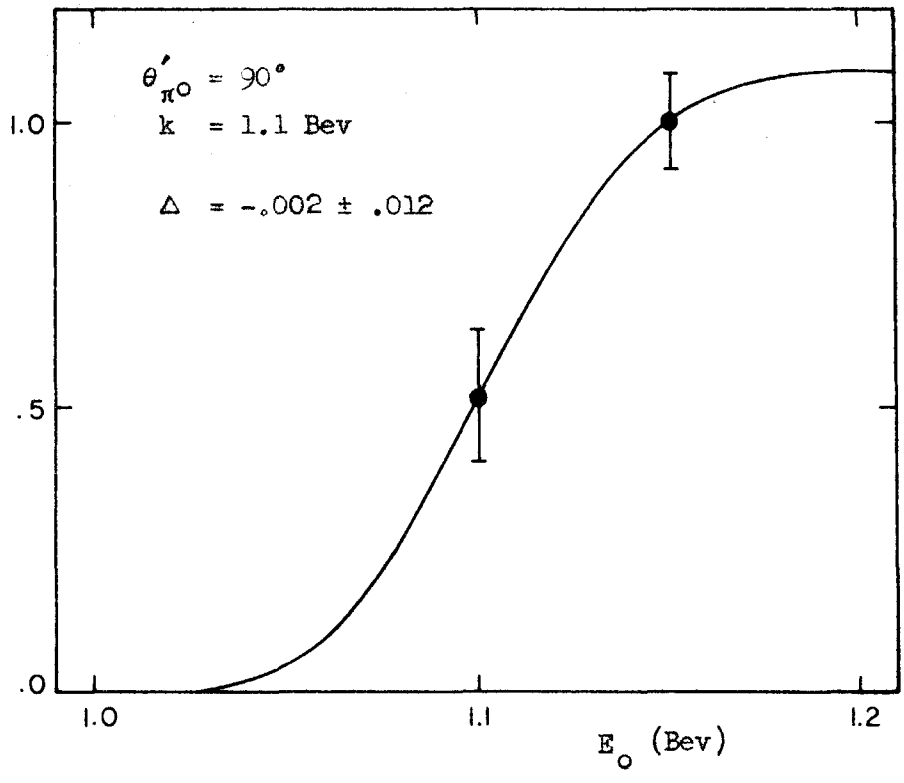

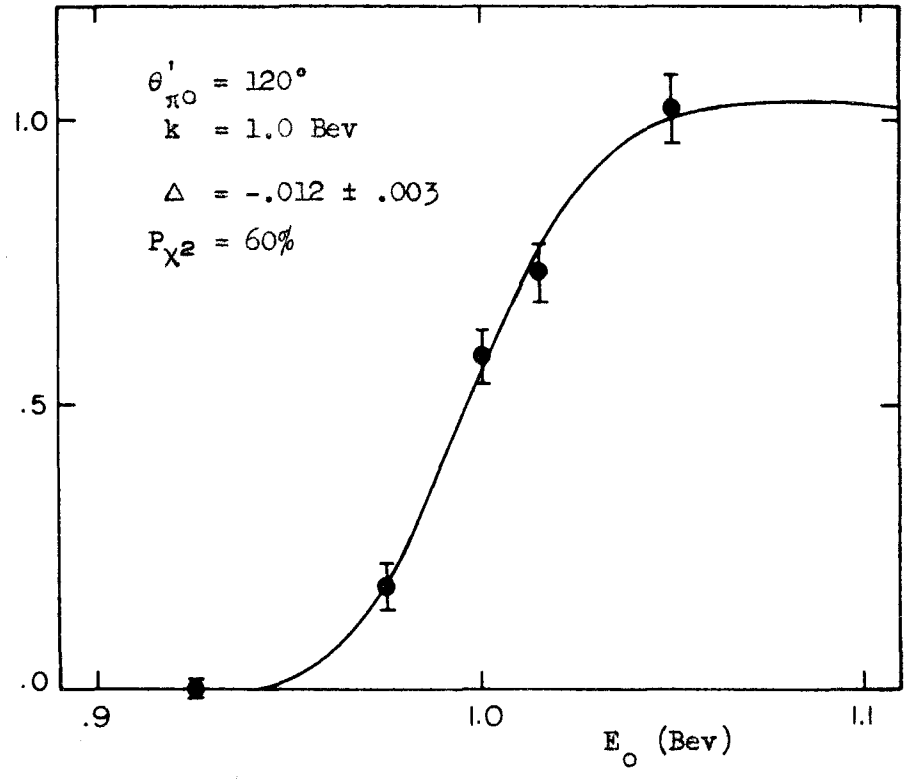

Photon Energy Consistency Check Results

Figure A2 c,d

where the error has been increased by a factor of 1.5 to take into account the large spread in individual Δ values (P_{χ^2} = 12% using the statistical errors).

A similar check was made by Dixon (26) who looked at positive pions with the spectrometer in the medium energy position. His results indicated no discrepancy, but the calculations assumed a sharp cutoff in the photon spectrum at E_o instead of the more rounded one found by Boyden. A rough estimate of the calculated response of Dixon's system using Boyden's spectrum indicates that

$$\Delta_{\tilde{\text{Dixon}}} - .010 \pm .004 \text{ Bev}$$

Since the source or sources of the discrepancy are not known, the difference was split between k and E_o; i.e., for the analysis of the experiment the following values were used:

$$k = .996 \times k_{\text{nominal}}$$

$$E_o = 1.004 \times E_{o_{\text{nominal}}}$$

APPENDIX V

Absorption Measurements and Corrections

Measurements were made to determine the fraction of protons passing through the spectrometer system which are lost as the result of nuclear interactions. Protons which interact in one of the rear counters may still be recorded as a proton, since one or more of the charged secondary particles may pass through the remaining counters. Very few of the protons interacting early in the system, e.g., in counter A1, will have secondaries which can give a proton signature. Table A3 lists the material through which the protons pass in going from the target to counter C3.

The absorption by the rear counters was studied by not requiring counter C3 in the proton definition. The fraction of protons not accompanied by a C3 pulse was then obtained as a function of the CH absorber thickness placed between counters C2 and C3. The slope of this function gave the fraction of protons lost per unit absorber thickness; its absolute value was used to extract the inefficiency of counter C3 due to geometry or other effects.

The rear counter absorption results are shown in Figure A3a. The point labeled Ch was obtained by observing the counting rate with and without the lucite Cherenkov counter in the counter box (C3 required; the Cherenkov counter not used electronically). The curve is proportional to the fraction of protons undergoing nuclear interactions as computed from the hydrogen cross sections given by MacGregor, et al. (38) and from the carbon cross sections given by H. de Carvalho (39). The constant

Table A3

Material Through Which the Protons Pass from the Target Center to Counter C3

Description		Elements	Thickness (gm/cm^2) ME	Thickness (gm/cm^2) HE	Thickness (radiation lengths[a]) ME	Thickness (radiation lengths[a]) HE
target	liq. hydrogen	H	.23[b]	.25[b]	.003	.003
	mylar	H,C,O	.02	.02	0	0
	heat shield	Cu	.07	.07	.005	.005
	outer shield	Al	.43	.43	.018	.018
air (target to Al)		N,O	.16	.30	.004	.008
counter Al		CH	.68	.68	.015	.015
air (Al to C3)		N,O	.30	.44		
C1 and C2	plastic	CH	3.16	3.16		
	Al wrappings	Al	.14	.14		
Lucite Cherenkov Counter	plastic	$C_5H_8O_2$	(not used)	4.45		
	Al wrappings	Al		.05		

[a]Calculated using the formula given by Rossi (37) which includes screening effects.

[b]Average value as determined by resolution calculations (see Appendix IX).

Figure A3a: Proton Absorption in CH in the Rear Counter Box

The curve is .47 times the fraction of protons undergoing nuclear interactions.

M - ME position

H - HE position

Ch- HE position, obtained by taking runs with and without the lucite Cherenkov counter in place.

Figure A3b: Proton Absorption in CH in Front of the Magnet

The curve shows the fraction of protons undergoing nuclear interactions.

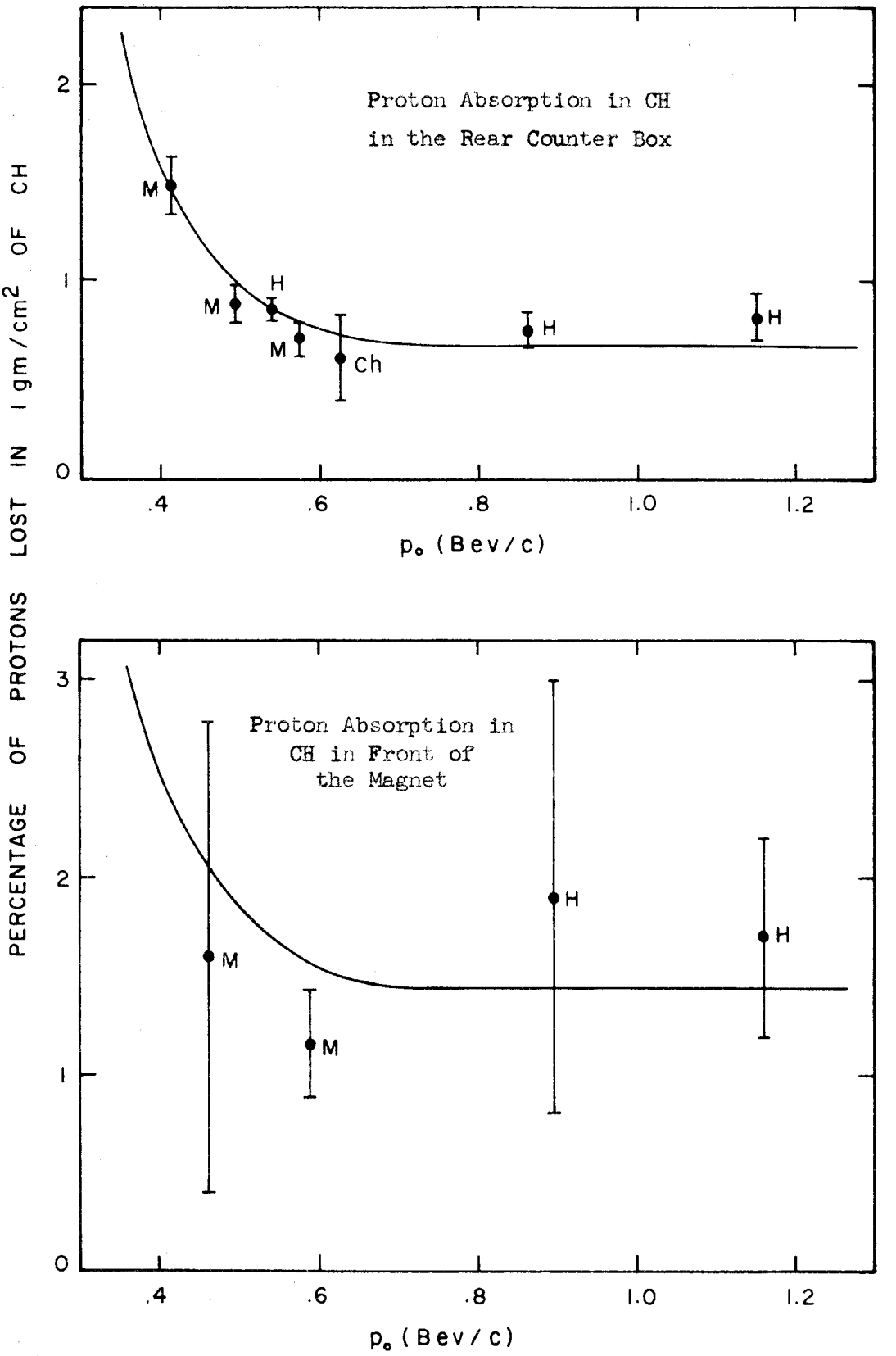
Proton Absorption in CH
in the Rear Counter Box
PERCENTAGE OF PROTONS LOST IN 1 gm/cm² OF CH
M
M
H
M
Ch
H
H
0
1
2
.4
.6
.8
1.0
1.2
p₀ (Bev/c)
Proton Absorption in
CH in Front of
the Magnet
PERCENTAGE OF PROTONS LOST IN 1 gm/cm² OF CH
M
M
H
H
0
1
2
3
.4
.6
.8
1.0
1.2
p₀ (Bev/c)

Figure A3

of proportionality which best fits the data is .47; i.e., a little more than half of the protons undergoing nuclear interactions produced secondaries which gave a large, photon-like pulse in C3. The curve fits the experimental data quite well, indicating that the fraction of interactions producing acceptable secondaries is independent of momentum to within the statistical accuracy of the measurements. For the lack of a better guide, this curve was used for the C1, C2 and lucite Cherenkov counter absorption corrections; it was assumed that all protons interacting in C3 produced an acceptable pulse.

The C3 inefficiencies obtained for the two positions are:

$$\lambda_{ME} = .5 \pm .2\% ,$$

$$\lambda_{HE} = 2.5 \pm .7\% .$$

The large HE position inefficiency is mainly a geometric effect; the C3 counter is not quite long enough to catch all the particles which are otherwise accepted by the system. This inefficiency must be taken into account because the value of the spectrometer solid angle used in the cross section calculation is based on measurements made with C2 as the limiting counter.

The absorption of protons by material in front of the target was studied by observing the counting rates with and without CH absorbers placed in the proton path near counter A1. The magnetic field of the spectrometer was lowered for the runs taken with the absorbers to compensate for the proton energy loss in passing through the absorbers. If we let N(p) be the momentum density of protons produced in the target within the solid angle of the spectrometer, A be the

fraction of protons not absorbed, and p_o be the central momentum of the magnet:

$$C = AN(p)\,\Delta p$$

$$\approx AN(p)\,\frac{dp}{dp_o}\,p_o\,\frac{\Delta p_o}{p_o}$$

where $\frac{\Delta p_o}{p_o}$ is the spectrometer acceptance constant. For the lower momentum points the factor $\frac{dp}{dp_o}\,p_o$ becomes quite important, changing with absorber thickness as rapidly as A. The results are shown in Figure A3b. Because they were obtained by subtracting large numbers, the results have large errors in spite of long running with a thick carbon target. The curve shows the percentage of protons which undergo nuclear interactions per unit thickness of CH. Under the assumption that all of the protons undergoing nuclear interactions are lost, the chi-squared probability of the experimental points is 70%. This assumption was used to compute the correction for absorption by all of the material in the proton path with the exception of the rear counters.

A Monte Carlo program was written by J. Kilner to determine if multiple scattering contributes to the proton losses. It was found that the scattering out of the system is compensated by the scattering into the system. Thus a correction is not needed in the cross section calculations; the effect does spread the photon resolution (see Appendix IX), however, having an indirect effect on the cross section measurement.

The effects of nuclear absorption in the various parts of the system have been combined with the C3 inefficiency to give the factor A,

the fraction of protons not lost. Table A2 in Appendix I lists the values of A used for the various points; the values range from .89 to .95. At the lowest momentum point C3 was not required; for this point absorption in C2 and the inefficiency of C3 were not included in A.

APPENDIX VI

Lucite Cherenkov Efficiency and Use in Eliminating Pions and Electrons

If we let e_π^+ be the efficiency for a pion to give a "+" (6 channel coincidence circuit output plus Cherenkov) count, N_+ be the number of "+" counts, N_p be the number of protons which have passed through the system, etc., then

$$N_+ = e_\pi^+ N_\pi + e_p^+ N_p$$

$$N_- = e_\pi^- N_\pi + e_p^- N_p ,$$

which can be solved to give

$$N_p = \frac{e_\pi^+ N_- - e_\pi^- N_+}{e_\pi^+ e_p^- - e_p^+ e_\pi^-}$$

$$N_\pi = \frac{e_p^- N_+ - e_p^+ N_-}{e_\pi^+ e_p^- - e_p^+ e_\pi^-}$$

Ideally

$$e_\pi^+ + e_\pi^- = 1$$

$$e_p^+ + e_p^- = 1 ,$$

but the electronics occasionally recorded a single particle as both a "+" and "-" count and the two sums were slightly greater than unity. Figure A4 shows e_p^+ and e_π^- as a function of momentum for the 35V. bias which was used during most of the experiment. Also shown is an indication of the effect of the discrimination bias level on the efficiencies. The

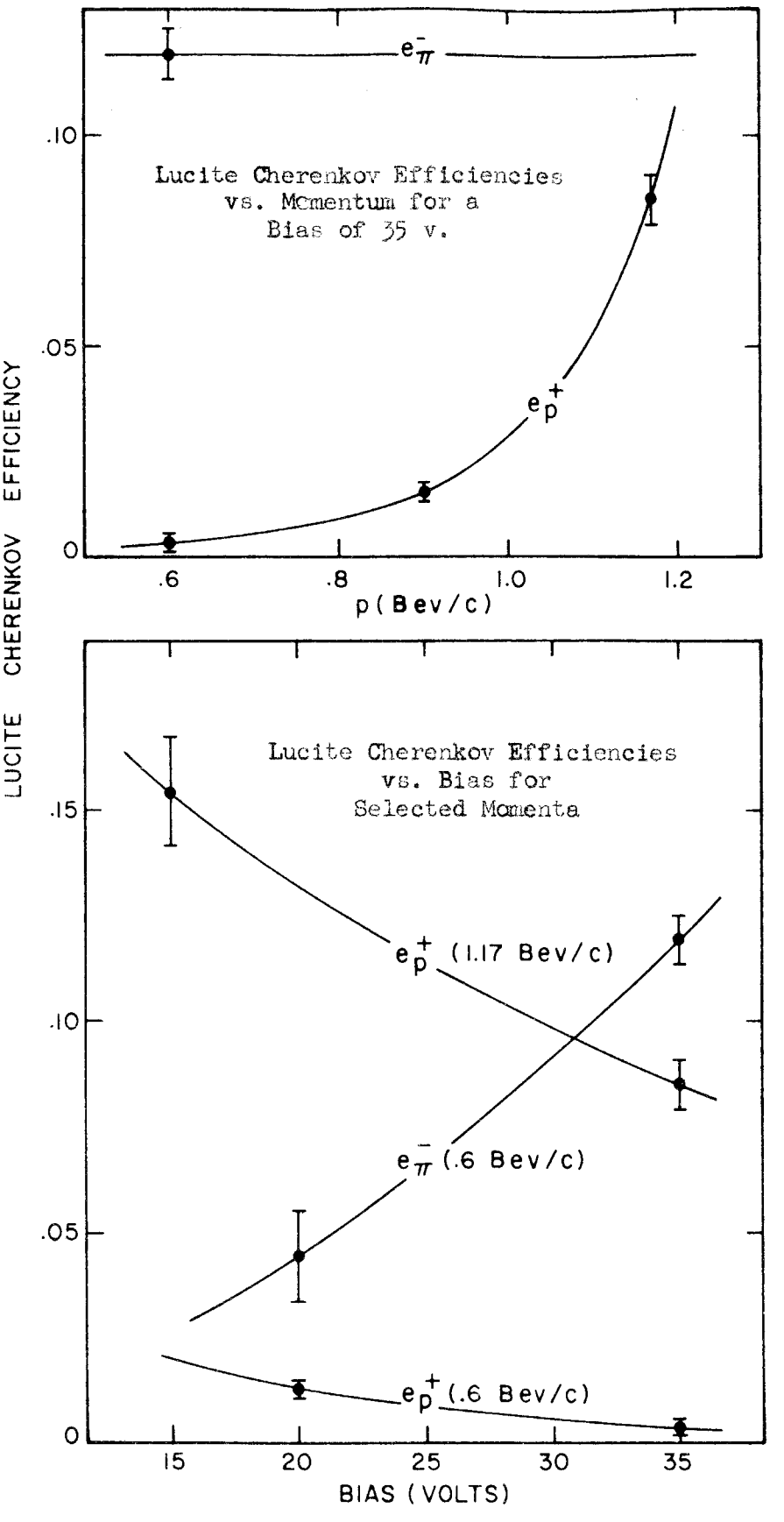
LUCITE CHERENKOV EFFICIENCY
Lucite Cherenkov Efficiencies
vs. Momentum for a
Bias of 35 v.
e^-_π
e^+_p
.10
.05
0
.6
.8
1.0
1.2
p(Bev/c)
Lucite Cherenkov Efficiencies
vs. Bias for
Selected Momenta
e^+_p (1.17 Bev/c)
e^-_π (.6 Bev/c)
e^+_p (.6 Bev/c)
.15
.10
.05
0
15
20
25
30
35
BIAS (VOLTS)

Figure A4

Cherenkov counter gain was checked against the bias several times during the experiment and the small drifts were compensated by varying the amplifier gain.

As expected for the points with momenta < .9 Bev/c, the lucite Cherenkov counter indicated that very few pions escaped rejection by the combined time of flight and pulse height criteria. The few "+" counts which were obtained were about the number expected from the proton Cherenkov efficiency. Since these counts were statistically distributed, N_π as determined from the above formalism, had a statistical distribution about an average value close to zero and was frequently less than zero. For this reason it was assumed that all the pions were rejected by the other criteria for these runs.

At higher momenta ($\gtrsim$ .9 Bev/c) the formalism developed above was used to give N_p. Even for the highest momentum runs N_π was generally found to be small as expected on the basis of kinematic considerations (see Appendix XII) combined with the partial elimination of pions by the other criteria. At worst the number of pions not eliminated by the time of flight and pulse height information were only a few per cent of the number of protons. In a few instances in which the Cherenkov counter system was malfunctioning, N_π was taken to be zero.

There were two instances in which electrons were important. The first, and more serious, was caused by the magnet just behind the first scrapper sweeping large numbers of electrons produced in a one inch carbon target out of the beam and toward the spectrometer system. A lead wall was erected near the magnet entrance to shield Al from this flux. At certain magnet angles the electrons from the sweeping magnet,

while not being able to hit Al directly, were able to strike the copper coils close to Al and create showers causing high Al counting rates. An appreciable number also found their way to the counters in the rear despite large amounts of lead shielding. Judging from the C1:C2:C3 coincidence rate a large number of these passed through all the rear counters including the lucite Cherenkov counter. The high counting rates caused false coincidences in the time of flight circuit which combined with electrons passing through the four rear counters gave large numbers of "+" counts. The concrete blocks were then placed as shown in Figure 1, and the counting rates returned to normal.

Although the runs with high "+" counting rates were not used in the cross section determinations, they were examined to determine whether many of the accidentals also appeared in the "-" channel, giving an apparent increase in the proton counting rate. If such were the case, considerable care would be required to determine how much, if any, of this contamination was present in the runs which were used.

The runs with many accidentals were compared to those taken with the same spectrometer settings which had a negligible number. For runs taken with liquid hydrogen it was found that

$$\frac{\Delta C_p}{\Delta C_\pi} = -.02 \pm .26;$$

for empty target runs the ratio was

$$\frac{\Delta C_p}{\Delta C_\pi} = -.06 \pm .04$$

where C_p and C_π were computed from the "+" and "-" counting rates by the formalism described earlier and the Δ refers to the difference between

the runs with and without accidentals. This would indicate that there were few, if any, proton-like accidentals and that the Cherenkov counter can be used to eliminate the few accidentals which may be present in those runs used to measure the cross sections (at these momenta both pions and electrons have velocities close to unity, and the Cherenkov efficiencies should be the same).

The second source of electrons was the scrapper directly in front of the liquid hydrogen target, which for a short period was inadvertently placed so that one edge grazed the beam and produced large numbers of electrons which passed through the target. A few of these electrons scattered in the target and passed through the spectrometer system. For all but the very high momentum runs they were eliminated along with the pions by the time of flight and pulse height criteria. The few high momentum runs made at this time had large numbers of "+" counts (about 30% of the protons) and were not used.

APPENDIX VII

Pi Pair Calculations and Corrections

Estimates of the contamination of the proton counting rates by the processes

$$\gamma + p \longrightarrow \begin{matrix} \pi^o + \pi^o + p \\ \pi^+ + \pi^- + p \end{matrix}$$

were obtained by taking data with E_o raised to values greater than normally used.

As the bremsstrahlung end point E_o, is raised from below threshold for single π^o production, the counting rate undergoes a rapid increase as E_o passes through the energy region in which the spectrometer has a large probability for detecting the recoil protons from single π^o production. This fast rise or step was studied in Appendix IV in connection with consistency checks of the photon energy. Above the fast rise the counting rate (cts/equivalent quanta) from single π^o production (and the lower energy phenomena such as Compton scattering) levels out and becomes constant. As E_o is raised further, photons become available with sufficient energy to produce two pions and a recoil proton which can be detected by the spectrometer system. The counting rate thus begins to rise again, although slowly at first because of the limited amount of phase space available to the pions.

The counting rates above the single pion step were fit with two terms. The first was a constant corresponding to single π^o production, Compton scattering, etc., while the second was proportional to the

counting rate computed with the statistical model for charged pi pair production. If pi pairs were really produced statistically (i.e., isotropically in the c.m. system with no isobar effects), one could obtain the pi pair contribution to the counting rate from the total pi pair cross section. This could not be done for many reasons, however: not only are the pi pairs produced anistropically with isobar effects, but the total neutral pi pair cross section is not known. The statistical model was thus used only to give the energy dependence of the pi pair contribution. The constant of proportionality, η , for this term was adjusted to fit the data. This constant takes into account the deviation from isotropy, the isobar effects, and the neutral contribution; it will be used later in this appendix to give an estimate of the neutral pair contribution.

The statistical charged pi pair term was computed by folding the spectrometer resolution with the invarient phase space formula (derived later in this appendix) for pi pair production:

$$\frac{d^2\sigma}{dpd\Omega} = H(k)\,\frac{p^2}{E}\sqrt{1 - \frac{4m^2}{\mathcal{m}^2}}$$

where

$H(k)$ is an invarient related to the square of a matrix element; under phase space assumptions it depends only on k,

p,E, and Ω refer to the proton in any system,

$\mathcal{m}$ is the effective mass of the two pi system, and

m is the pion mass.

$H(k)$ depends on the total charged pi pair cross section for photons of energy k. The total cross sections of Chasan, et al. (22) for charged

pairs were used below 1.0 Bev, and their data were extrapolated for $k > 1.0$ Bev.

The experimental counting rates are shown in Figure A5 for the two points at which many values of E_o were run. Because of the uncertainties involved in considering pair production over such large energy ranges, some fits were made using only the results of the lowest E_o runs. (These uncertainties have many sources: the total cross sections; the contributions from many pi production; and the deviations from a statistical distribution which may vary considerably with energy as shown by Chasan, et al.) The fits are also shown in Figure A5; none of them are very good and some are quite poor. The results are given in Table A4 for the two points considered in Figure A5; also tabulated are the results obtained at two other points, each of which was run with only two values of E_o. There is some ambiguity to the measurements in that the fits using different numbers of points indicate different pair contributions, and for this reason the results are not as well determined as one might have hoped.

Since only a few measurements were made of a possibly rapidly changing number, large errors had to be assigned to the values used in the analysis. The calculated pi pair contributions to the cross section points are listed in Table A1.

The statistical model proton counting rate from charged pi pairs was calculated in much the same way as was that for single pi production in Section IV:

$$C_{stat} = N_H \left(\frac{\Delta p_o}{p_o} \Delta \Omega \right) \frac{dp}{dp_o} p_o A \frac{p^2}{E} \iint dp d\theta R(p) R(\theta) \int_{k_{threshold}}^{E_o} dk \frac{B}{k} H \left[1 - \frac{4m^2}{m^2} \right]^{\frac{1}{2}}$$

Figure A5. Pi Pair Measurements and Fits

The points were obtained experimentally by fixing the spectrometer to observe recoil protons from single π^o production by a photon of energy k at a pion center of mass angle θ'_{π^o}. The error flags represent the statistical uncertainty of the points. The curves for each spectrometer setting are two parameter fits to the n points with lowest values of E_o. The first parameter is the constant which takes into account the contributions from single π^o production, Compton scattering, etc. The second parameter is the constant of proportionality multiplying the contribution expected on a statistical basis from charged pair production.

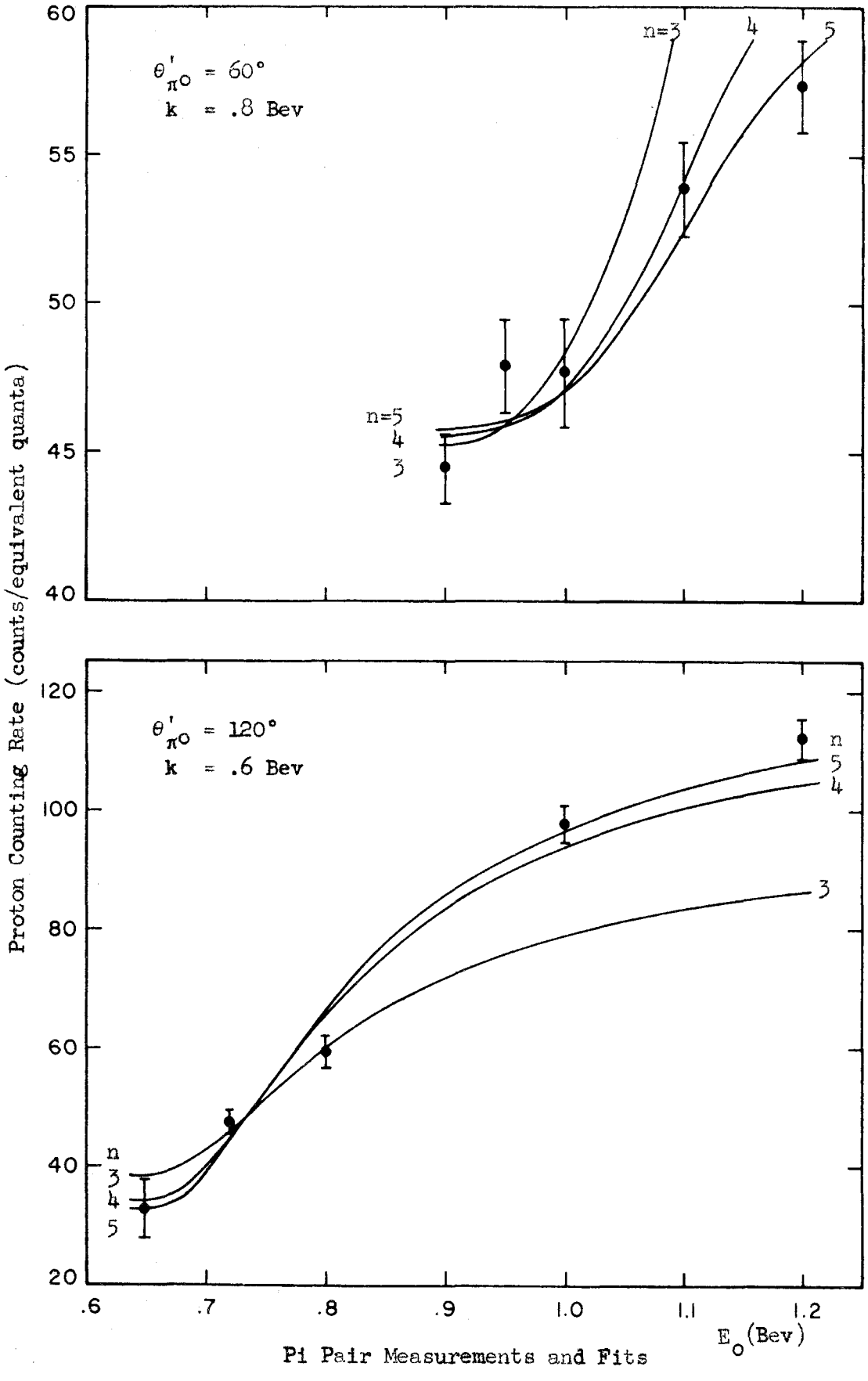

Pi Pair Measurements and Fits

Figure A5

Table A4

Pi Pair Fitting Results

θ'_{π^o}	k	n	C_o	η	P_{χ^2}
60°	.790 Bev	3	45.3 ± 1.0	5.9 ± 4.3	.14
		4	45.6 ± .9	3.2 ± .8	.27
		5	45.8 ± .8	2.5 ± .4	.26
90°	.743	2	48.2 ± 1.9	.9 ± .5	-
90°	1.088	2	9.3 ± .7	3.3 ± 3.2	-
120°	.595	3	38.6 ± 3.0	.6 ± .2	.16
		4	34.4 ± 2.4	.9 ± .1	.02
		5	33.1 ± 2.3	1.0 ± .1	.02

where

n = number of E_o values used for the fit,

C_o = constant corresponding to single π^o production, etc.,

η = pi pair proportionality constant giving the ratio between the observed number of pairs and the number of charged pairs expected on a statistical basis, and

P_{χ^2} = chi-squared probability of the fit to the results at n values of E_o.

Values Used in the Analysis

θ'_{π^o}	η
60°	2.9 ± 1.5
90°	1.0 ± .8
120°	.8 ± .8

where $R(p)$ and $R(\theta)$ are the normalized spectrometer responses in momentum and angle (see Appendix IX); the factor U/E_o has been omitted since we are considering counts per equivalent quanta.

The observed pi pair counting rate differs from the statistical rate by a factor η:

$$C_{pairs} = \eta C_{stat.}$$

This factor can be separated into three factors

$$\eta = \eta_\theta \eta_p (1 + a)$$

where η_θ and η_p take into account the angular and momentum deviations of the charged pion pair differential cross sections from those of the statistical model and a takes into account the additional contribution from neutral pair production. The factors η_θ and η_p can be obtained from the distributions given by Chasan, et al., which are, unfortunately, poorly determined. The remaining factor is also poorly determined. Vette and Worlock each evaluated a by running two points at more than one value of E_o in a manner similar to that described earlier in this appendix. Vette concluded that $a = 0$, while Worlock took $a = 1$; the large difference in their values for a may be due to η_θ and η_p being different at the points used by the two experiments.

Using values of η_θ and η_p interpolated from the Chasan data, values of a were calculated for the points at which pair measurements were made in this experiment. The results are summarized in Table A5.

Table A5

Pi Pair Results Interpreted in Terms of the Neutral Pair Factor "a"

θ'_{π^o}	k	η	$\eta_\theta \eta_p$	a
60°	.790	2.9 ± .7	1.9 ± .7	.5 ± .7
90°	.743	.9 ± .5	1.3 ± .5	- .3 ± .5
90°	1.087	3.3 ± 3.2	1.0 ± .4	2.3 ± 3.6
120°	.595	.8 ± .2	.41 ± .15	1.0 ± .9
60°	.790			.3 ± .7*
				$\bar{a}$ = .2 ± .4

*Obtained from measurements using the photon detection equipment

The number of charged pions contributing to the proton plus converted γ-ray counting rate for the k = .8 Bev, θ'_{π^o} = 60° point was measured experimentally at E_o = 1.2 Bev. The pulse heights in counter 1A were examined in detail. It was found that 83% of the single charged particles gave pulse heights less than 1.5 times minimum ionizing and that only 8% of the electron showers initiated by a π^o decay photon gave such a small pulse. The fraction of small pulses less than 1.5 times minimum ionizing with E_o = 1.2 Bev was found to be 18%, giving the number of charged particles as 13 ± 3% of the total proton plus converted γ-ray counting rate for E_o = 1.2 which was

$$C_{1.2} = 22.0 \pm .9 \text{ cts/100 BIPS.}$$

Subtracting the charged particles and converting to counts/equivalent quanta (a factor of 1.32) gave

$$C^{o}_{1.2} = 25.2 \pm 1.3 \text{ cts/e.q.}$$

We can compare this with the counting rate at $E_o = .9$ (pairs kinematically forbidden):

$$C_{.9} = 24.2 \pm 2.2 \text{ cts/e.q.}$$

The difference can be interpreted as contributions from neutral pair production:

$$C_{\substack{\text{neutral} \\ \text{pairs}}} = 1.0 \pm 2.5 \text{ cts/e.q.}$$

or

$$\frac{\text{neutral pairs}}{\text{charged pairs}} = a = .3 \pm .7.$$

The invarient phase space formula used to estimate the pi pair contamination will now be derived. The differential cross section for protons is obtained by integrating over the meson variables (40):

$$\frac{d^2\sigma}{dpd\Omega}\, dpd\Omega = \frac{2\pi}{|v_1 - v_2| E_1 E_2} \int_{\substack{\text{over} \\ \text{meson} \\ \text{variables}}} |\mathcal{L}|^2 \, (2\pi)^4 \delta^{(4)}\left(\sum_{in} p - \sum_{out} p\right) \prod_{out} 2\pi\delta(p_i^2 - m_i^2) \frac{d^4 p_i}{(2\pi)^4}$$

(subscripts 1 and 2 refer to the incoming photon and proton, a and b to the outgoing mesons). The denominator is an invarient and is most easily evaluated in the lab:

$$|v_1 - v_2| \, E_1 E_2 = cMk.$$

The quantity $\mathcal{L}$ is a matrix element which does not depend on the outgoing particle parameters if we assume the particles to be statistically distributed. Integrating over the delta functions and ignoring constants gives

$$\frac{d^2\sigma}{dpd\Omega}\, dpd\Omega = \frac{|\mathcal{L}|^2}{k}\frac{p^2}{E}\, dpd\Omega \int \frac{p_a^{\,2}}{E_a E_b}\left|\frac{\partial\, \Omega_a}{\partial\, E_T}\right|_{\substack{\vec{p},p_a \\ \text{constant}}} dp_a$$

where

$$E_T = E + E_a + E_b \ .$$

If we let $\mathcal{P}$ and $\mathcal{E}$ be the momentum and energy of the two pi system,

$$E_b^{\,2} = p_b^{\,2} + m^2 = (\vec{\mathcal{P}} - \vec{p}_a)^2 + m^2 = \mathcal{P}^2 - 2\mathcal{P}p_a\cos\theta_a + p_a^{\,2} + m^2$$

where the polar axis has been taken in the direction of $\vec{\mathcal{P}}$. Since $\vec{p}$ and p_a are held constant for the evaluation of $\frac{\partial\Omega_a}{\partial E_T}$, $\mathcal{P}$ is also constant (by momentum conservation) and also

$$dE_T = dE_b \ .$$

The quantity dE_T can be evaluated from the equation above:

$$dE_T = -\frac{\mathcal{P}p_a}{E_b}\, d\cos\theta_a$$

$$= -\frac{1}{2\pi}\frac{\mathcal{P}p_a}{E_b}\, d\Omega_a \ .$$

Thus we are left with

$$\frac{d^2\sigma}{dpd\Omega} = \frac{|\mathcal{L}|^2}{k}\frac{p^2}{E}\frac{1}{\mathcal{P}}\int \frac{p_a dp_a}{E_a}$$

$$= \frac{|\mathcal{L}|^2}{k}\frac{p^2}{E}\frac{1}{\mathcal{P}}\,(E_{a+} - E_{a-})$$

where E_{a+} and E_{a-} are the maximum and minimum total energies available to meson a.

This difference can be expressed as

$$E_{a+} - E_{a-} = \mathcal{P}\left[1 - \frac{4m^2}{\mathcal{M}^2}\right]^{\frac{1}{2}}$$

where m is the pion mass and $\mathcal{M}$ is the effective mass of the two pi system (see Appendix XII for formulas giving $\mathcal{M}$). If we define

$$H(k) = \frac{|\mathcal{L}|^2}{k},$$

the equation used for the fitting is obtained. (Note: due to the invarient nature of the calculation, the proton parameters may be evaluated in any one system.)

Vette (11) and Worlock (14) used a slightly different formula, one which was not invarient; it does not have the energy denominators of the calculation described above (giving a different normalization to the matrix element). The dependence on the proton parameters is the same in the center of mass system as for the invarient calculations except for the addition of a slowly varying factor:

$$E' \left[3\mathcal{E}^2 - \mathcal{P}^2\left(1 - \frac{4m^2}{\mathcal{M}^2}\right)\right]$$

(Note: Vette's equation 12, p. 55 of his thesis (11) has the wrong sign in front of the fractional term under the square root).

If the total cross section is known, H(k) may be determined by integrating over the proton parameters; the integration is most easily done in the center of mass (primed) system:

$$\sigma_T = 4\pi H(k) \int_0^{p'_+} \left[1 - \frac{4m^2}{m^2}\right]^{\frac{1}{2}} \frac{p'^2}{E'} \, dp'$$

$$= 4\pi H(k) \int_M^{E'_+} \left[1 - \frac{4m^2}{m^2}\right]^{\frac{1}{2}} p' \, dE' \, .$$

This integration was done numerically for several different photon energies, and values for H(k) were obtained using a smooth curve drawn through the total charged pair cross section points of Chasan, et al. (22).

APPENDIX VIII

Below Threshold Background and Wide Angle Nuclear Scattering

A comparison of the proton plus lead glass Cherenkov counter rates with the proton only rates showed a distinct discrepancy; the proton only rates from hydrogen were about 15% higher than expected on a basis of the proton plus lead glass rates. The difference, C_{BTh}, between the rates (corrected for the Cherenkov geometric efficiency) is shown in Figure A6a for the cross section points. The number of extra protons appeared to be independent of E_o (fig. A6b) for the runs taken with the spectrometer set to look at the recoil protons from π^o photoproduction at $\theta'_{\pi^o} = 60°$ and k = .8 Bev. The error flags on the points in Figure A6 reflect the counting statistics; the fact that the two counting rates involved are not statistically independent was taken into account.

It is interesting to note that C_{BTh} did not drop at the E_o = .7 Bev point. This fact precludes the simple hypothesis that these protons are recoils associated with the photoproduction of a light particle since even protons from Compton scattering were largely excluded at this energy. The mass spectrometer test of the liquid hydrogen indicated that the protons could not be coming from interactions of the beam with contamination in the hydrogen.

For a few of the points at which the lead glass counter was not used, runs were taken with low values of E_o to give estimates of this effect. The results are shown in Table A6. The 60°, 1.1 Bev value is

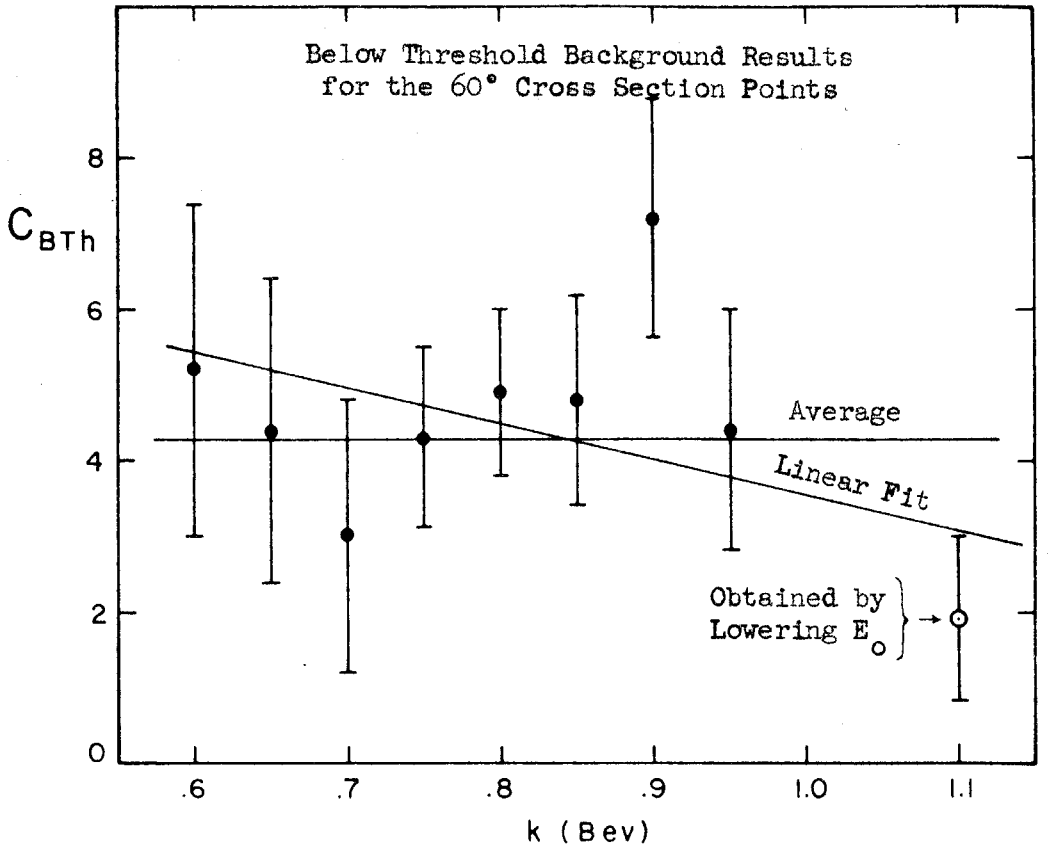
Below Threshold Background Results
for the 60° Cross Section Points
C_{BTh}
8
6
4
2
0
Average
Linear Fit
Obtained by
Lowering E_o
.6
.7
.8
.9
1.0
1.1
k (Bev)

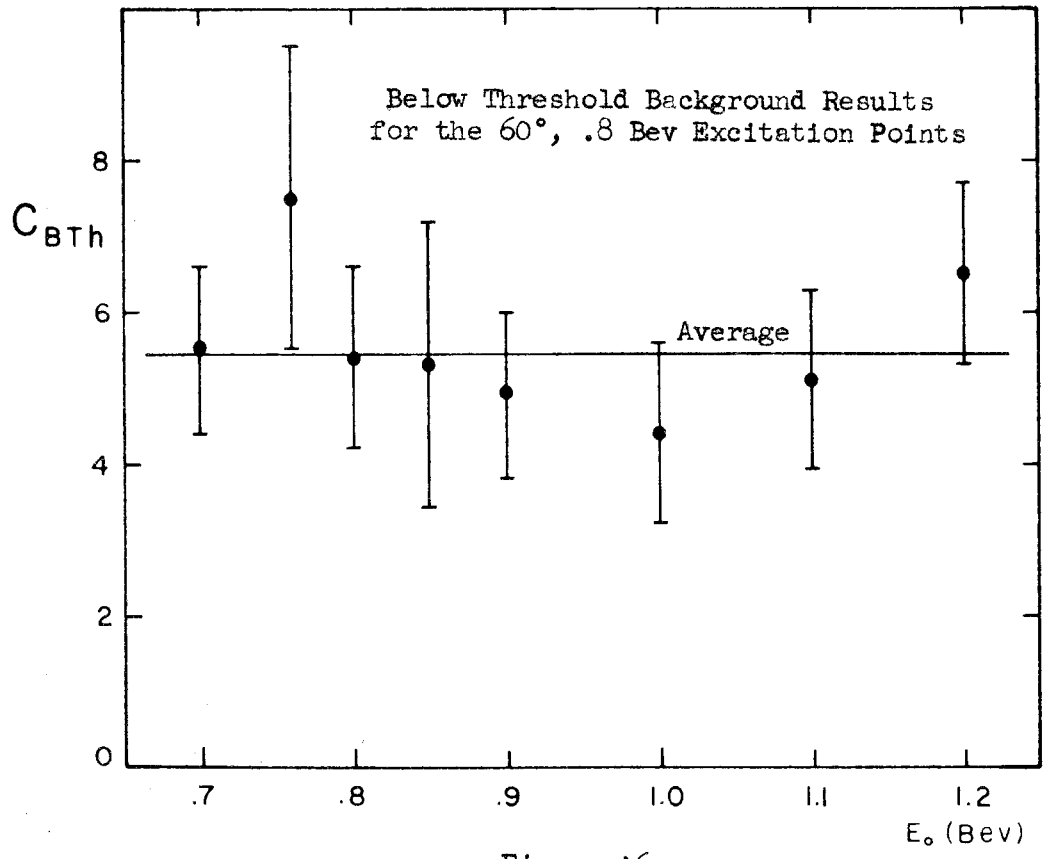
Below Threshold Background Results
for the 60°, .8 Bev Excitation Points
C_{BTh}
8
6
4
2
0
Average
.7
.8
.9
1.0
1.1
1.2
E_o (Bev)

Figure A6

Table A6

Below Threshold Background Results Obtained by Lowering E_o

Magnet Position	θ'_{π^o}	k	E_o	C_{BTh}
M	60°	1.10 Bev	.95 Bev	1.9 ± 1.1 cts/100 BIPS
H	90°	.90	.80	1.1 ± 1.1
H	90°	1.15	1.05	.4 ± .4
H	120°	1.00	.925	.5 ± .5

shown in Figure A6a as the open circle. Also shown in the figures are lines indicating the average values. Figure A6a shows the least squares linear fit to the points in that figure; this fit has a chi-squared probability of 45%.

For those points taken with the lead glass counter, the proton plus lead glass counter rates were used to obtain cross sections. For the remainder of the 60° points the linear fit discussed above was used to correct the proton counting rates. The experimental data at the other angles are rather meager and statistically inaccurate. The linear 60° fit was multiplied by constants at each of the other two angles; these constants were chosen so that the experimentally obtained values of C_{BTh} at the particular angle were fit as best as possible; this was then used as the correction with an assigned error of 100%. The corrections used at each point are shown in Table A1; at 90° and 120° they were typically 2 or 3% of the π^o counting rate.

Presumably this background is the result of wide-angle nuclear scattering which somehow depends on the presence of hydrogen in the

target (otherwise the empty target runs would cancel it out). The hydrogen dependence can come from two different types of processes: 1) the hydrogen can scatter protons and neutrons (the neutrons produce recoil protons), and 2) it can produce high momentum protons which then scatter in the target or from the edges of the lead slit placed next to the target.

Two specific processes were studied in detail; in both of these processes high energy protons undergo elastic nuclear scattering with the protons of the liquid hydrogen. The cross sections for such scattering are known experimentally (38): the total cross section goes from 55 mb at .3 Bev/c incident proton momentum down to 25 mb at .6 Bev/c, above which it is flat; the scattering is essentially isotropic in the center of mass system. Since the probability that a .6 Bev proton undergoes nuclear scattering while traversing 7.6 cm (the target diameter) of liquid hydrogen is only .8%, a relatively large flux of protons must be available in order to account for the background in this manner.

First, recoil protons from π^{o} photoproduction were considered. It was hoped that the kinematics would be such that some of the protons produced in large numbers at the first resonance could scatter into the spectrometer. Unfortunately, the kinematics are such that at best only the tail of the resonance can contribute. Figure A7 shows contours of the photon energy required to give a recoil proton at angles θ and ϕ with sufficient momentum to scatter into the spectrometer system.

Secondly, protons produced in the mylar cup were considered. To give an estimate of the number of such protons, the values for C_x obtained with the empty target runs were fitted to a function of the form

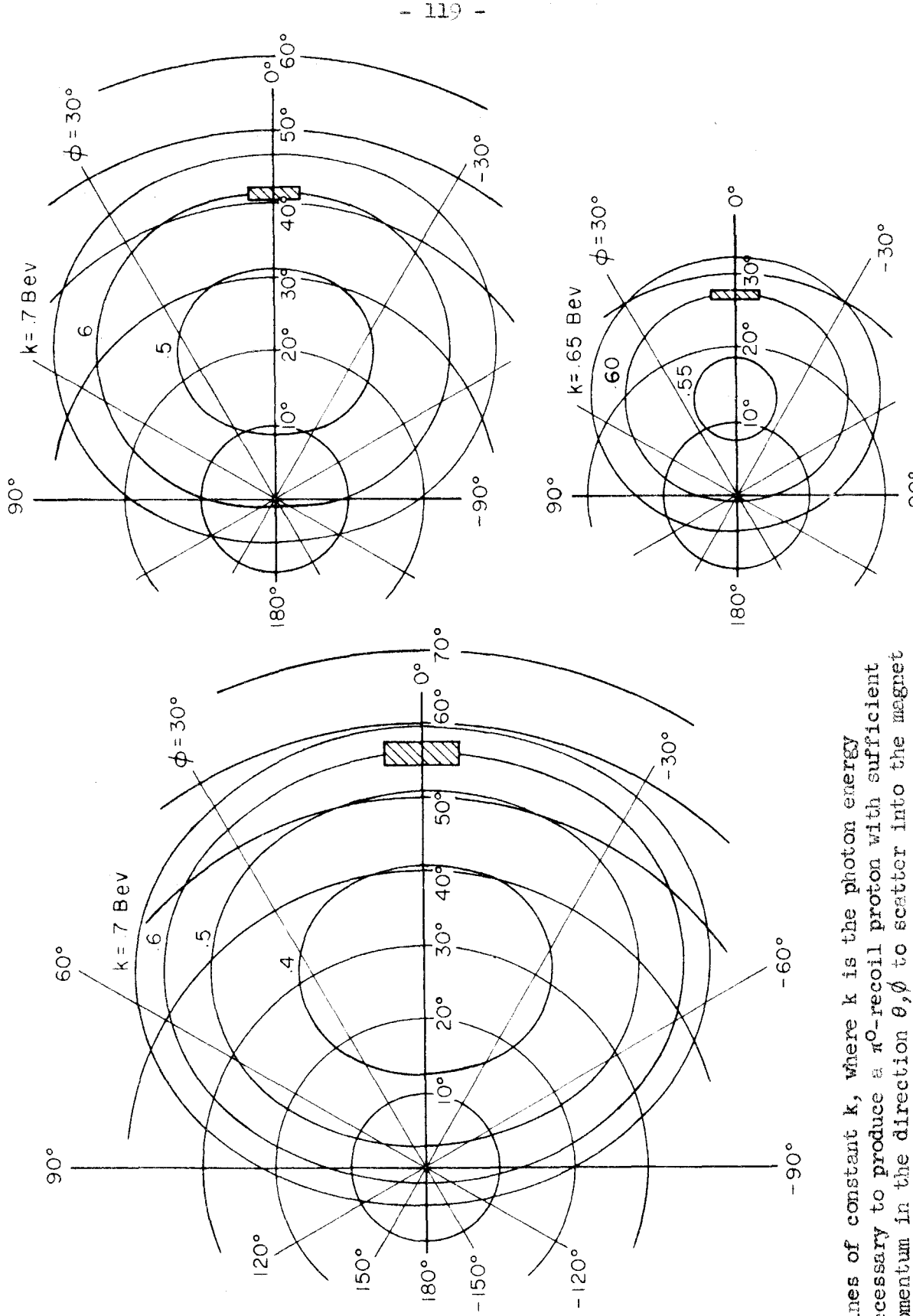

Lines of constant k, where k is the photon energy necessary to produce a π^0-recoil proton with sufficient momentum in the direction θ, ϕ to scatter into the magnet

Figure A7

$$\frac{d^2C_x}{dpd\Omega} = \frac{U}{E_o}\, cp^a\left(\frac{k}{E_o}\right)^b$$

where a, b, and c are linear functions of θ. As with the first process, not enough protons were available for scattering. Together the two processes gave only 5 to 10% of the number observed.

Neutrons can similarly be produced by pion photoproduction and by beam interactions in the mylar cup. Although only one of the two outgoing particles from n-p scattering is a proton, the contributions are presumably about the same as those just considered because the π^+ photoproduction cross sections at these energies are larger than those for π^o production.

The probability for nuclear scattering of protons in the 1/16" outer aluminum shield of the target is .6%. Since such scatterings occur 18 centimeters from the target center, appreciable sideways displacement from the magnet center plane can take place, and unless the particles incident to the scattering are within about 20° (in the horizontal direction) of the magnet angle, they cannot pass through the magnet system. Because of this geometric effect the contribution is at best a few per cent of that observed; this still leaves about 80% of the effect to be explained.

Possibly there are enough protons (about one proton in 10^5 photons) traveling with the beam which scatter in the target and cause the effect. This hypothesis is not self-consistent, however, in that about four times as many protons are needed to explain the effect at $\theta'_{\pi^o} = 60°$ as for the other angles.

The last hypothesis is that high momentum protons which were produced in the hydrogen scattered from the heavy metal parts of the target or from the lead slits placed next to the target. The scattering of protons from the slit edges was examined experimentally. This was done by blocking up the slit in such a manner that protons could get through the magnet only by scattering from the edge of the slit closest to the beam. Counting rates were compared with and without this side of the slit. It was found that $-.3 \pm 1.9\%$ of the particles normally passing through the system were scattered from this edge. This is consistent with no scattering; at most the poor statistics of the experiment provide an uncertainty of 2% which might have scattered from the slits. It would thus seem that this hypothesis is also unable to explain the large background at the $\theta'_{\pi^o} = 60^\circ$ points.

The main source of these unwanted protons thus remains a mystery which will have to be solved if further work on π^o photoproduction is to be done at the forward pion angles by observing only the recoil proton.

APPENDIX IX

Resolution Calculations

The angular and momentum resolutions of the target-spectrometer system were calculated for several of the experimental points. These resolutions were then used to calculate the incident photon energy resolution and the amounts of contamination from competing processes, e.g., protons from pi pair production. The decay photon detection scheme used during the early part of the experiment did not have much influence on the incident photon energy resolution.

The factors determining the resolutions can be split into three general groups: 1) the finite size of the beam-target interaction volume, 2) slowing and scattering, and 3) the finite spectrometer resolutions. The relative effect of these factors varies from point to point; in particular, slowing and scattering are important only for the low momentum points.

In order to demonstrate the method of calculation and to give an idea of the relative importance of the factors, the calculations for a particular point will be given in detail. The point chosen is that for which the central values of the magnetic spectrometer were set to correspond to k = .800 Bev and $\theta'_{\pi^o} = 60°$ for single π^o photoproduction.

A coordinate system was set up with the origin at the target center (y = 0 at the beam center), z in the direction of the beam, y in the vertical direction, and x horizontally to the right when looking into the beam. The beam collimation system limited the interaction volume to

$$-2.25 \leq x \leq 1.85 \text{ cm}$$

$$-2.85 \leq y \leq 2.05 \text{ cm} .$$

The position of the beam center varied horizontally with the bremsstrahlung end point energy from x = 1.04 cm at .7 Bev to x = - .17 cm at 1.3 Bev. For the particular point in question the center was at x = .64 cm.

The spacial distribution d_r of the beam (E_o = .9 Bev) which was used for the calculations is that of Figure 2a. The dashed curve in Figure A8a is a cut of the beam distribution along the x-axis. (This distribution and the others shown in Figures A8a-m have been arbitrarily normalized to give a maximum value of unity.) The distribution was averaged in the y direction and renormalized to give the distribution d_x. A second coordinate system was set up with the same origin but with the horizontal axis t perpendicular to the central ray of the magnet (positive to right when looking from magnet to target). The interaction density d_t was obtained by integrating over d_x and is shown in Figure A8b. A second interaction density was also obtained, d_s, where s is the distance which must be traveled through hydrogen by a proton going in the direction of the magnet; it is shown in Figure A8c.

Figure A8d shows the angular resolution which would be obtained if the only spreading were due to the finite beam-target interaction volume; this resolution was obtained from d_t. When it was folded with the angular acceptance of the magnet (dashed curve, fig. A8e) the solid line of Figure A8e was obtained. The relatively low momentum (.486 Bev/c) of the protons led to appreciable multiple scattering in the target material,

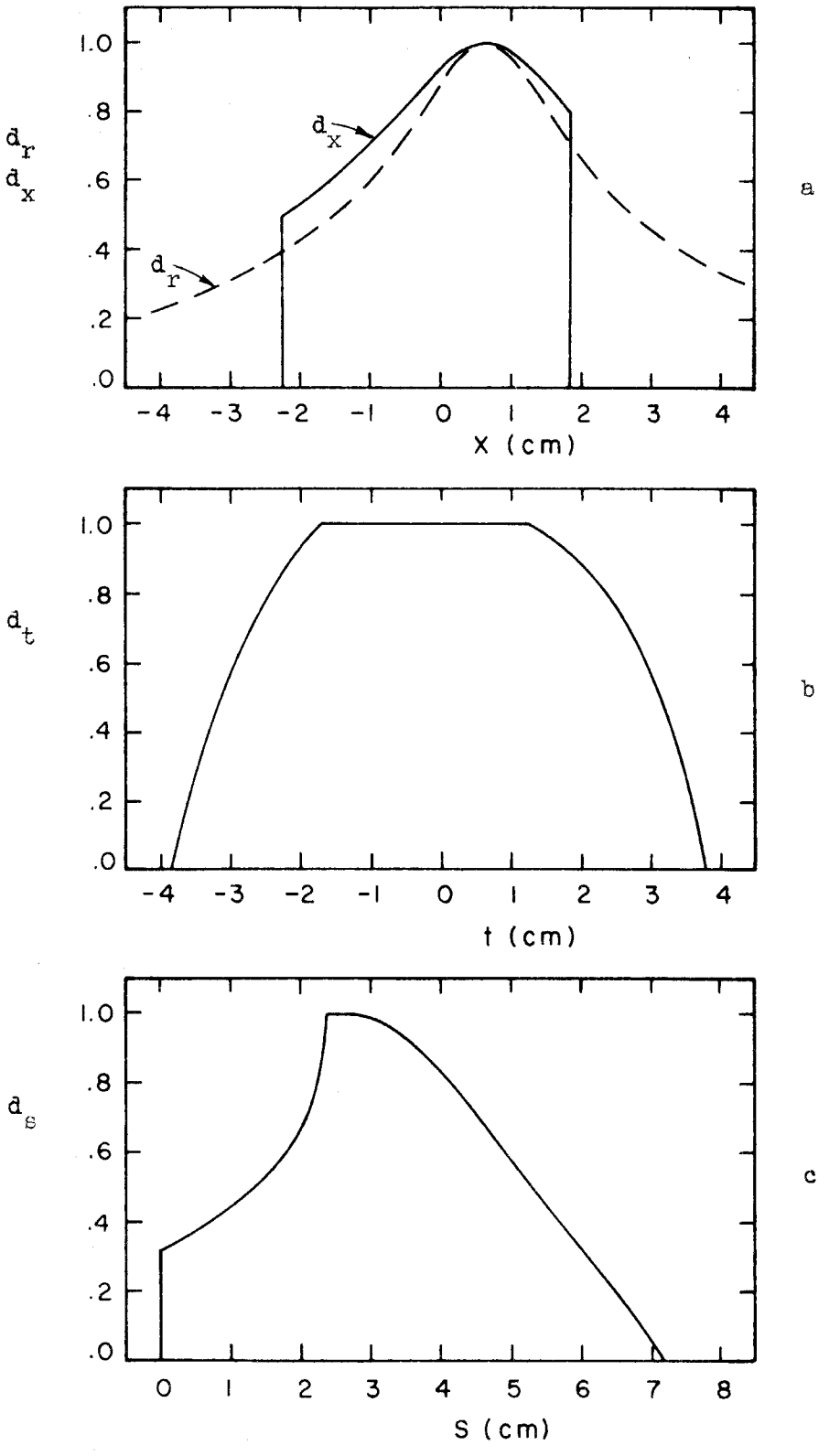

Resolution Calculation

Figure A8 a,b,c

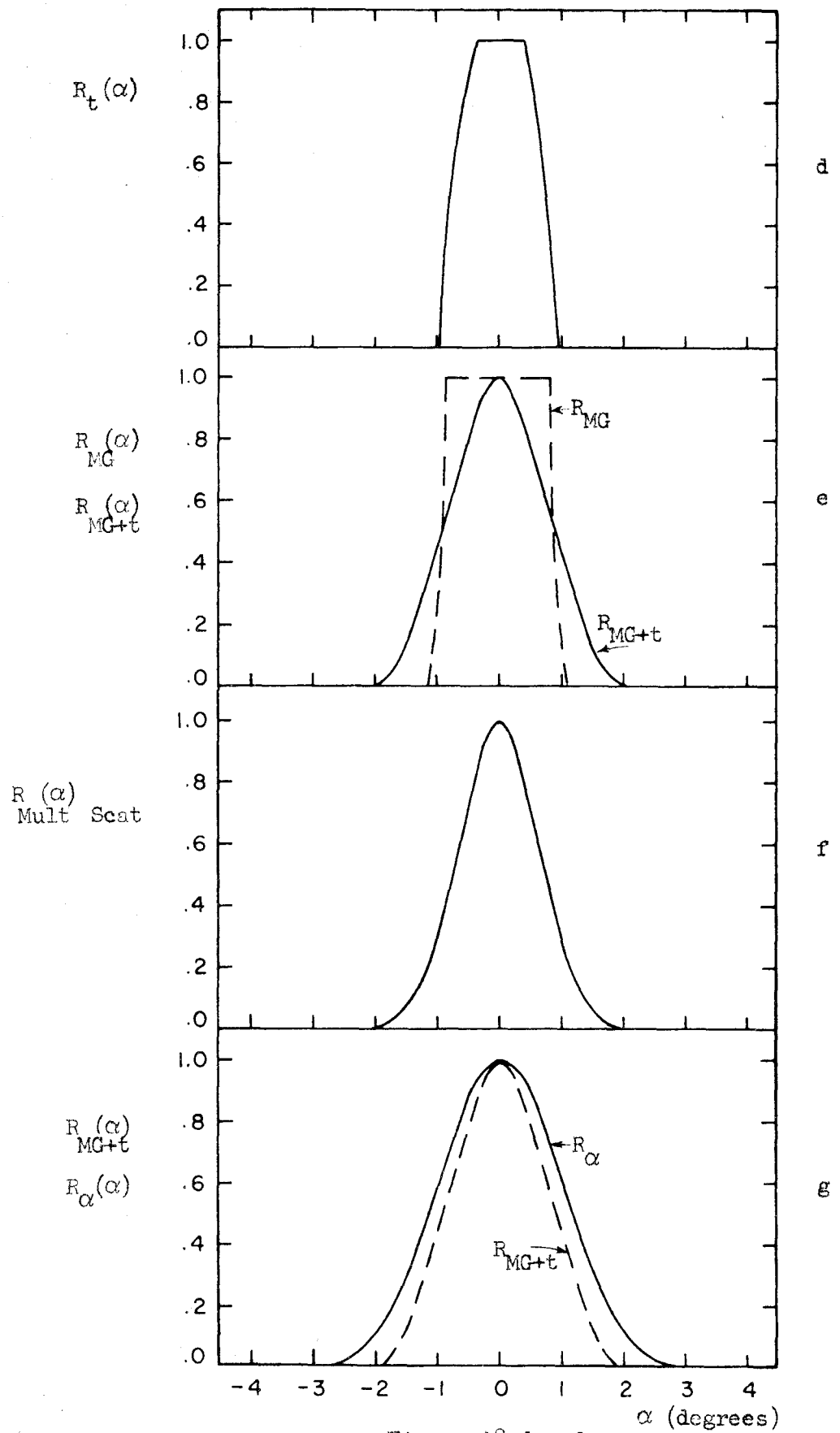

Figure A8 d,e,f,g

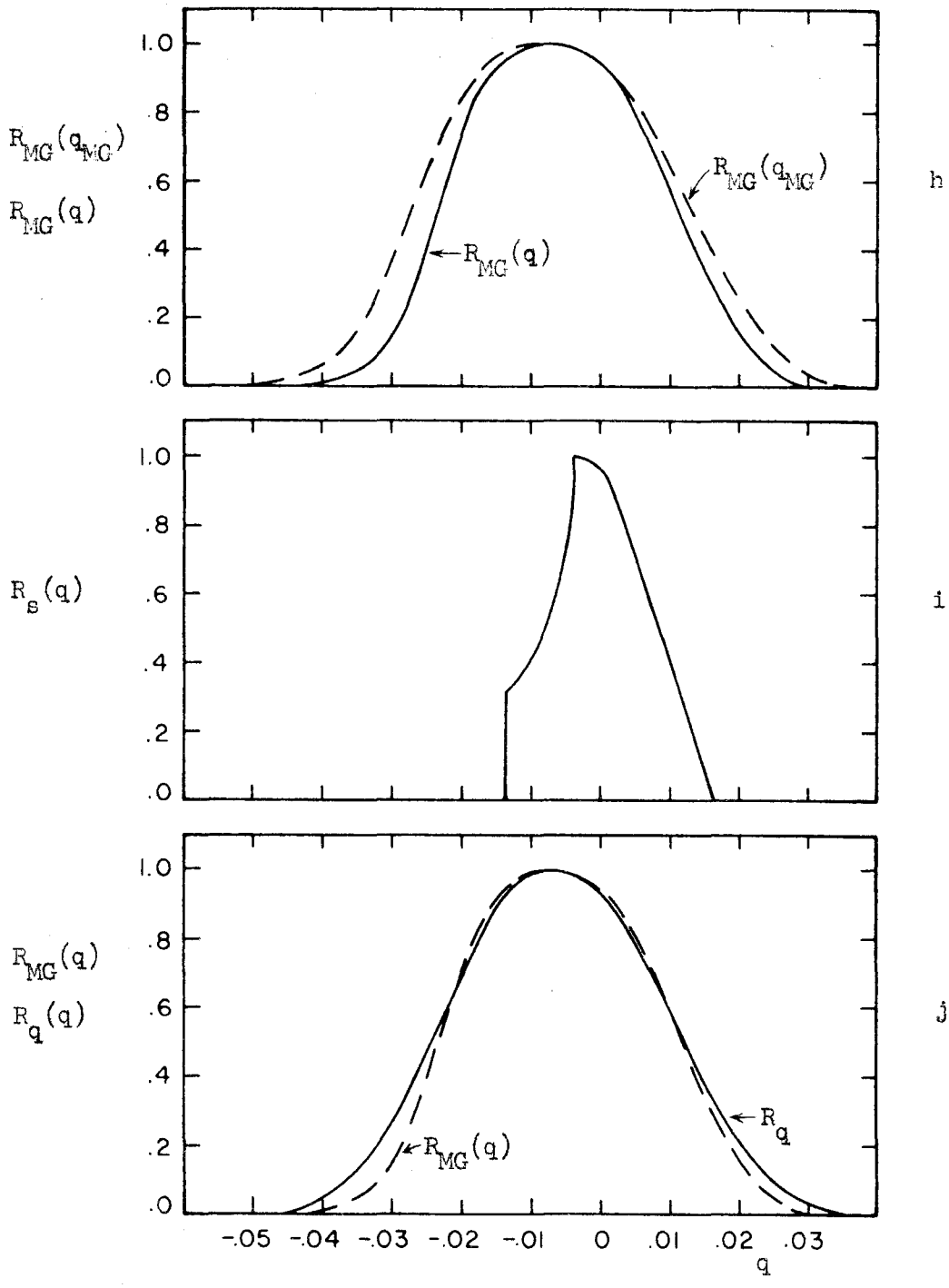

Resolution Calculation

Figure A8 h,i,j

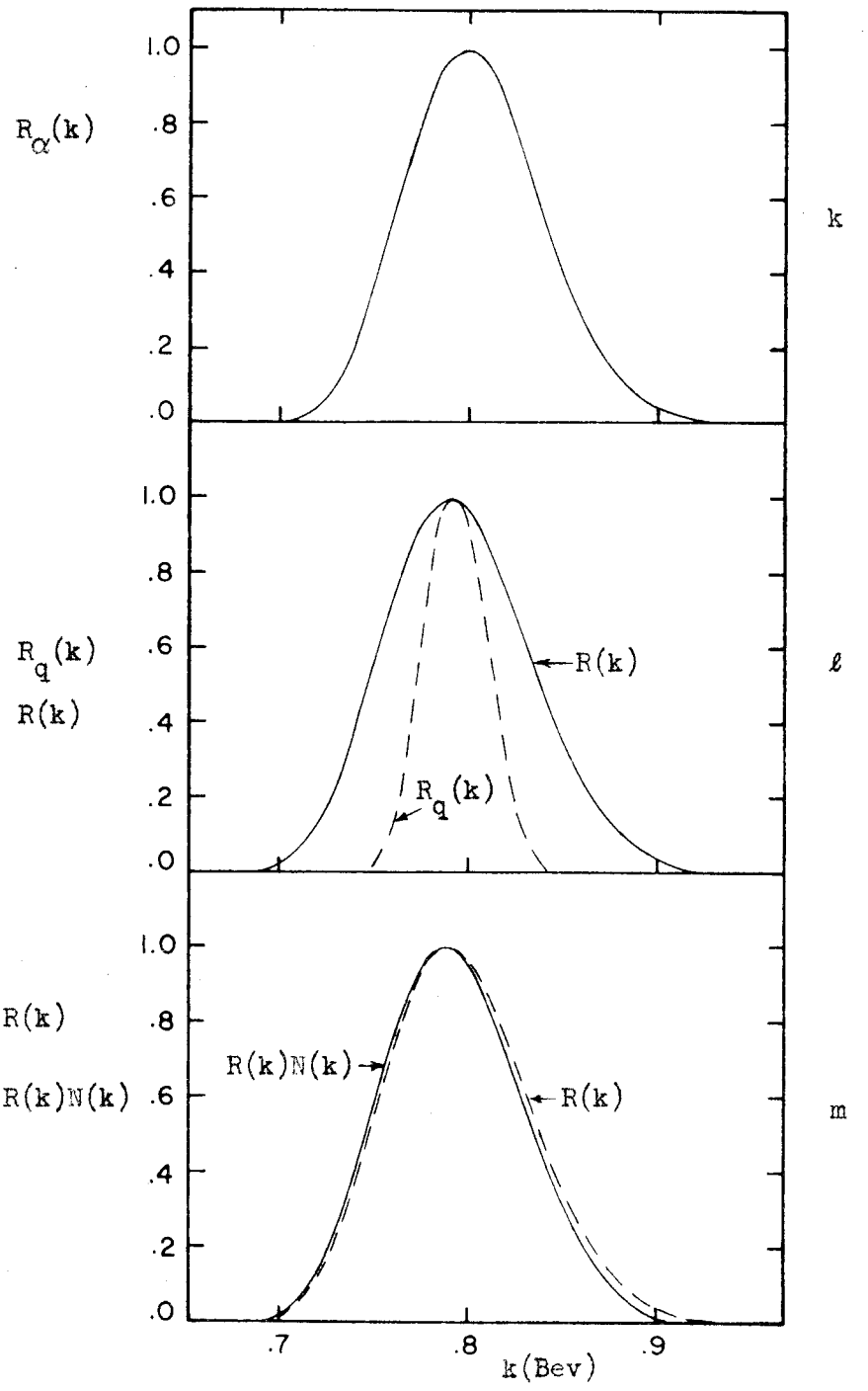

Resolution Calculation

Figure A8 k,ℓ,m

air path, and counter A1 (total effective path length of .028 radiation lengths; see Table A3 for the radiation length of each contributor). This multiple scattering gave a Gaussian spread with $\sigma = .63°$ which was folded with the magnet-target resolution to give R_α, the total angular resolution of the system (solid line, fig. A8g). The multiple scattering increased the full width at half maximum from 1.85° to 2.33°.

The momentum resolution of the magnet-target system was obtained by a Monte Carlo computer program coded by J. Kilner which ignored the effects of slowing in the target; this resolution is plotted in Figure A8h as a function of $p_{MG} = (p_{MG} - p_o)/p_o$ where p_o is the momentum corresponding the central ray of the magnetic spectrometer and p_{MG} is the proton momentum at the center of the magnet. The solid line in the figure is the same resolution plotted as a function of $q = (p - p_o^s)/p_o^s$:

$$q \approx \frac{p_o}{p_o^s} \frac{dp_o^s}{dp_o} q_{MG} \approx .85\ q_{MG}$$

where p is the proton momentum extrapolated back to the target center and p_o^s is the momentum at the target center of a proton which has momentum p_o by the time it gets to the center of the magnet. Even if the magnet had perfect momentum resolution, there would be a spread in the momentum-at-production accepted by the magnet because of the different path lengths of the protons in the hydrogen. This spread is shown in Figure A8i (plotted as a function of q) and is obtained from d_s. The total momentum resolution R_q, is plotted as the solid line in Figure A8j.

R_α is plotted in terms of incident photon energy in Figure A8k. R_q is similarly plotted as the dashed curve in Figure A8ℓ; the two combined give the solid curve of that figure. This curve must be weighted

by the photon spectrum which is proportional to $B(k,E_o)/k$. The photon resolution of R_k thus obtained is shown as the solid curve in Figure A8m; the unweighted resolution is also shown for comparison. The principle effect of the weighting is to shift the median photon energy downward by ~ 3 Mev.

The relative amount of spreading of the photon resolution by the angular and momentum distributions varied with angle. The finite angular acceptance played an important role at $\theta'_{\pi o} = 60°$, but became less important with increasing angle; at 120° it contributed very little to the photon energy resolution width. The spread in photon energy corresponding to the momentum resolution alone did not change appreciably with angle. The rectangles of Figure A10 indicate the angular and momentum acceptance widths, from which the contributions to the photon width may be obtained in an approximate manner.

APPENDIX X

Resonance Shapes Used to Fit the Data

In Section V fits are made to the data assuming that the amplitude for single π^o photoproduction consists of only a few terms. Most of these terms are assumed to exhibit a resonance behavior, but there is insufficient data for a phase shift analysis. For this reason a model had to be used.

The one chosen is that developed by Feshbach, et al. (34). For a single level they take

$$\sigma \alpha \frac{1}{k'^2} \frac{\Gamma_\gamma \Gamma_{scat}}{(W - W_r)^2 + \Gamma^2_{scat}}$$

where we interpret the quantities in a relativistic fashion as:

k' = c.m. photon energy,

W = total center of mass energy

W_r = resonant energy,

Γ_γ = partial width for $\pi^o + p \rightarrow \gamma + p$

Γ_{scat} = partial width for $\pi^o + p \rightarrow \pi^o + p$, and

it has been assumed that $\Gamma_{scat} \gg \Gamma_\gamma$.

The widths can be expressed as

$$\Gamma_{scat} = \frac{g_{scat}{}^x}{|v_\ell(\alpha x)|^2}$$

$$\Gamma_\gamma = \frac{g_\gamma}{|v_{\ell'}(\alpha y)|^2}$$

where

g_{scat} and g_γ are constants,

α = a dimensionless constant characterizing the πN interaction distance (taken to be .88),

x = c.m. pion momentum in units of its rest mass,

y = c.m. photon momentum in units of the pion rest mass,

ℓ = $(\pi^o p)$ orbital angular momentum,

ℓ' = photon total angular momentum or multipole order,*

$|v_\ell|^2$ = angular momentum barrier penetration factor.

The lowest order barrier penetration factors are

$$|v_o(x)|^2 = 1$$

$$|v_1(x)|^2 = (1 + x^2)/x^2,$$

$$|v_2(x)|^2 = (9 + 3x^2 + x^4)/x^4,$$

$$|v_3(x)|^2 = (225 + 45x^2 + 6x^4 + x^6)/x^6.$$

Once the orbital angular momenta are known there are three parameters for each resonance which may be adjusted to fit the data: 1) W_r which gives the resonance position; 2) g_{scat} which is proportional to the resonance width; and 3) g_γ which can be adjusted to give the appropriate strength of the resonance.

---

*Actually the photon orbital angular momentum should have been used. For magnetic transition this is just the multipole order; but for electric transitions the partial photon wave for a particular multipole is composed of two terms, one with orbital angular momentum $\ell'-1$ and the other with $\ell'+1$. For the electric transitions studied (second and third resonances) this approximation is not serious since the resonance shapes do not depend strongly on the particular model used at these high energies.

The phase of the amplitude corresponding to a resonant term is obtained in the usual manner:

$$\tan \delta = \frac{\Gamma_{scat}}{W_r - W} .$$

Gell-Mann and Watson (7) have used this type of formula to fit the single π^o photoproduction total cross section in the region of the first resonance ($\ell = \ell' = 1$). As can be seen from Figure 13, the main deviation from the simple Breit-Wigner curve is the behavior of the tails. At low energies the cross section goes to zero at threshold in the manner expected, while at high energies there is a rather long tail; this results in a skewing of the curve toward high energies. As can be seen in Figure 11 the skewing of the second and third resonances is much less pronounced, and using a simple Breit-Wigner formula for these terms would probably not have made a noticeable difference in the fits.

APPENDIX XI

Beam Monitoring

The beam monitors used during this experiment were devices which collected ions produced by the beam and gave a charge proportional to the amount of beam. They were calibrated with a Wilson quantameter (24) by R. Gomez. This instrument was designed to give an output proportional to the total energy u in the beam independent of E_o. Wilson calculates the charge collected by the quantameter to be

$$q = u_{Bev} \Big/ \left[4.79 \times 10^{15} \frac{150}{t} \frac{2.73}{p/T} \frac{\rho_{Cu}}{8.91} \right] \text{ coulombs}$$

where t is the average plate separation in cm, p/T is the gas pressure in mm of Hg/absolute temperature, and ρ_{Cu} is the density of the copper plates in gm/cm^3. The space between the 1 cm thick copper plates is filled with a 92.5% argon and 7.5% CO_2 mixture. For the Caltech quantameter

$$t = .1492 \text{ cm} ,$$

and

$$\rho_{Cu} = 8.88 \text{ gm/cm}^3 ,$$

giving

$$q = \frac{(p/T)_{Quantameter}}{13.10 \times 10^{15}} u_{Bev} \text{ coulombs} .$$

Wilson estimates that such an instrument should have an absolute accuracy of 3%.

The beam monitor (also known as the Beam Catcher or BC) could not be calibrated against the quantameter (Q) directly because both

devices destroy the beam. Instead they were each compared to a third ionization chamber (the Air Chamber or AC shown in fig. 1) which did not destroy the beam, but which was subject to drifts. To eliminate the effects of these drifts BC and Q were compared to AC alternately several times. The charge outputs were integrated and for convenience converted to units of BIPS. An average value of the ratio R was obtained from the alternating runs:

$$R = \frac{BIPS_{AC}/BIPS_{BC}}{BIPS_{AC}/BIPS_{Q}} .$$

The values of R for the individual pairs of runs generally fluctuated by 1% or less. A second quantity was defined as

$$S = \frac{(p/T)_{BC}}{(p/T)_{Q}}$$

The various relations can be combined to give

$$U_o = M \frac{13.10 \times 10^{15}}{(p/T)_o} RS \text{ Bev/100 BIPS}$$

where $(p/T)_o$ refers to a standard pressure (mm of Hg) and temperature (^oK) of the beam monitor and M is the integrator constant:

$$M = .2106 \times 10^{-4} \text{ coulombs/100 BIPS} .$$

For different values of the beam monitor pressure and temperature

$$U = U_o \frac{(p/T)_o}{(p/t)} .$$

During the experiment three different beam monitors were used; they were known as: Chamber III; 1Cu - 1"; and Cu-Air. The first of these was a closed system and the ratio p/T was not dependent on the

transient laboratory conditions; it was found, however, that a slow leakage of gas out of the chamber resulted in a gradual decrease of this ratio by about .3% during its use in the experiment. The average value $p/T = 2.54 \frac{\text{mm of Hg}}{^{o}K}$ was used for the analysis. The other two monitors were open to the atmosphere and thus sensitive to the laboratory conditions. While these monitors were in use, the laboratory pressure and temperature were recorded frequently. It was found that the fluctuations of p/T had an rms deviation of $\frac{1}{2}\%$ centered about $2.48 \frac{\text{mm of Hg}}{^{o}K}$. Since these variations were small compared with the systematic errors, the average value was taken. Because only the average values of p/T are used for the chambers, we take $U = U_o$.

Unlike the quantameter, the beam monitor outputs were not independent of E_o; values of RS were obtained for several values of E_o, and smooth curves were drawn through the measured values. Values of U were obtained from these curves; typical results are shown in Table A7.

During the period in which Chamber III was in use, a thick carbon target was frequently placed directly in front of the chamber by another experiment. This reduced the output of the chamber by several per cent, and the number of BIPS recorded by the monitor equipment had to be multiplied by the factor ρ_{carbon} shown in Table A7 for those runs during which the carbon target was in place. This correction varied from 6% at $E_o = 1.2$ to 12% at $E_o = .7$.

For convenience all counting rates obtained in the medium energy position were standardized to Chamber III (without the carbon) BIPS and those of the high energy position to Cu-Air BIPS.

Table A7

Beam Monitor Constants

Beam Monitor	p/T	U	
Chamber III	2.54 $\frac{\text{mm of Hg}}{^{o}K}$	1.09×10^{11} RS	Bev/100 BIPS
1 Cu - 1"	2.48	1.11×10^{11} RS	
Cu-Air	2.48	1.11×10^{11} RS	

$M = .2106 \times 10^{-4}$ coulombs/100 BIPS

E_o Bev	$U_{\text{Chamber III}}$ Bev/100 BIPS	$U_{\text{1 Cu-1"}}$ Bev/100 BIPS	$U_{\text{Cu-air}}$ Bev/100 BIPS	ρ_{carbon}
.7	$.974 \times 10^{11}$	1.080×10^{11}	1.076×10^{11}	1.124
.8	.956	1.124	1.116	1.111
.9	.942	1.164	1.156	1.098
1.0	.927	1.202	1.196	1.086
1.1	.916	1.235	1.233	1.073
1.2	.907	1.265	1.267	1.061
1.3	.898	1.293	1.298	1.049

APPENDIX XII

Photoproduction Kinematics

Consider a photon of laboratory energy k incident on a proton of mass M at rest in the laboratory. The center of mass total energy W and photon energy k' can be expressed as

$$W = (M^2 + 2kM)^{\frac{1}{2}}$$

$$k' = \frac{M}{W} k$$

($c = 1$). The velocity β_{cm} and related quantity $\gamma_{cm} = (1 - \beta_{cm}^2)^{-\frac{1}{2}}$ of the center of mass system in the laboratory system are given by

$$\beta_{cm} = \frac{k}{k + M}$$

$$\gamma_{cm} = \frac{k + M}{W} .$$

The same center of mass total energy is obtained for a photon incident on a proton as for a particle of mass m and kinetic energy T incident on a proton if

$$k = T + m(1 + \frac{m}{2M}) .$$

For charged pions this becomes

$$k = T + .150 \text{ Bev} ,$$

a useful expression for relating photoproduction and pi-nucleon scattering.

For the reaction

$$\gamma + p \rightarrow \sum_{i=1}^{n} (\text{particle})_i + p \ ,$$

we can consider the n particles in the summation to have an effective mass $\mathcal{m}$ given by

$$\mathcal{m} = \left[(\sum_i^n E_i)^2 - (\sum_i^n \vec{p}_i)^2 \right]^{\frac{1}{2}}$$

where E_i, $\vec{p}_i$ refer to the i^{th} particle.

The center of mass momentum of the outgoing proton satisfies the relation

$$q = \frac{1}{2W}\left[W^2 - (M + \mathcal{m})^2\right]^{\frac{1}{2}}\left[W^2 - (M - \mathcal{m})^2\right]^{\frac{1}{2}}$$

For single pion photoproduction q is, of course, also the center of mass pion momentum:

$$q = \frac{1}{2W}\left[W^2 - (M + m)^2\right]^{\frac{1}{2}}\left[W^2 - (M - m)^2\right]^{\frac{1}{2}}.$$

The quantities, k, k', and q are plotted as a function of W for single π^o photoproduction from protons in Figure A9.

The center of mass total energy E' of the recoil proton can be expressed as

$$E' = \frac{1}{W}[k(E - p\cos\theta) + ME] \ .$$

The effective mass of the other outgoing particles can be obtained by either of the equations:

$$\mathcal{m} = \left[W^2 - 2E'W + M^2\right]^{\frac{1}{2}}$$

$$\mathcal{m} = \sqrt{2}\left[k(p\cos\theta - T) - MT\right]^{\frac{1}{2}}$$

where p, E and T all refer to the recoil proton in the laboratory system. The last equation can be solved for k:

$$k = \frac{MT + \frac{1}{2}\mathcal{M}^2}{p\cos\theta - T} .$$

For fixed proton laboratory kinematics and varying $\mathcal{M}$, k is seen to be a constant plus a term proportional to $\mathcal{M}^2$. Thus for small $\mathcal{M}$ the kinematics do not differ appreciably from those of Compton scattering ($\mathcal{M} = 0$). In Figure A10a lines of constant k are shown on a plot of p vs. θ for $\gamma + p \rightarrow \pi^o + p$; Figure A10b is similar, but for T_π vs. θ_π. In Figure A11 the kinematics for $\mathcal{M} = 0$ and 2m are compared with those for $\mathcal{M} = m$. Figure A12 compares the kinematics of the charged products of the reactions $\gamma + p \rightarrow \begin{cases} \pi^o + \underline{p} \\ \underline{\pi}^+ + n \end{cases}$.

The rectangles give an indication of the angular and momentum acceptance of the target-spectrometer system.

The laboratory and center of mass angles of any particle can be related by

$$\cos\theta' = \frac{\beta\cos\theta - \beta_{cm}}{\left[(1 - \beta_{cm}\beta\cos\theta)^2 - (1 - \beta_{cm}^2)(1 - \beta^2)\right]^{\frac{1}{2}}}$$

or

$$\cos\theta = \frac{\beta'\cos\theta' + \beta_{cm}}{\left[(1 + \beta_{cm}\beta'\cos\theta')^2 - (1 - \beta_{cm}^2)(1 - \beta'^2)\right]^{\frac{1}{2}}}$$

where β and β' are the particle velocities in the lab. and c.m. systems and θ and θ' are the lab. and c.m. angles between the direction of the particle and the direction of the c.m. system in the lab. system.

Two quantities which are needed for the conversion of counting rates to cross sections may be obtained by differentiating the equations above:

$$\left(\frac{\partial k}{\partial p}\right)_\theta = \frac{M\beta + k(\beta - \cos\theta)}{p\cos\theta - T}$$

$$\left(\frac{\partial \Omega'}{\partial \Omega}\right)_k = \frac{\beta^2(1 - \beta_{cm}^2)}{(\beta - \beta_{cm}\cos\theta)\left[(1 - \beta_{cm}\beta\cos\theta)^2 - (1 - \beta_{cm}^2)(1 - \beta^2)\right]^{\frac{1}{2}}} .$$

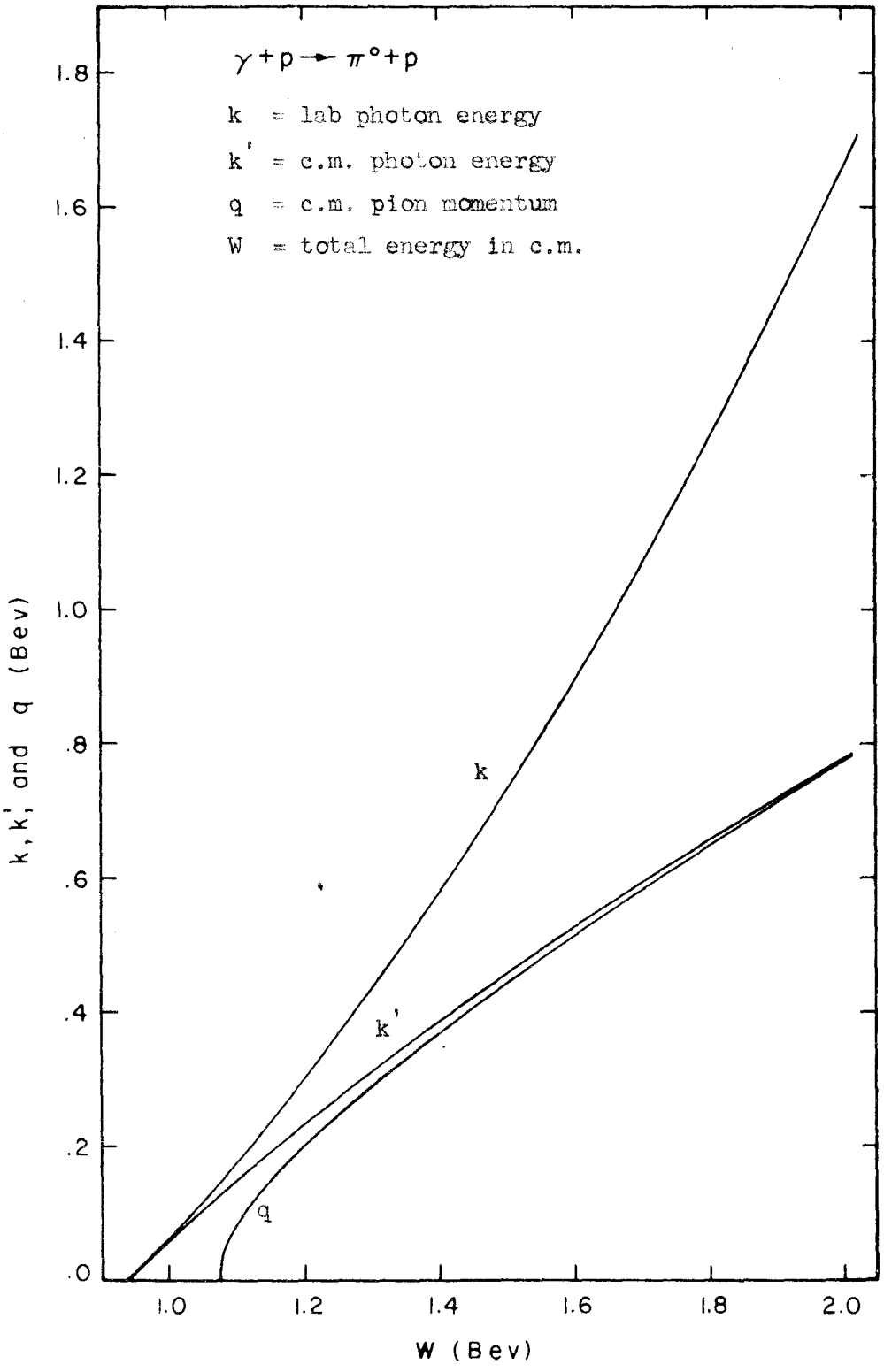
γ + p → π° + p
k = lab photon energy
k' = c.m. photon energy
q = c.m. pion momentum
W = total energy in c.m.
k
k'
q
k, k', and q (Bev)
W (Bev)
0
.2
.4
.6
.8
1.0
1.2
1.4
1.6
1.8
2.0

Figure A9

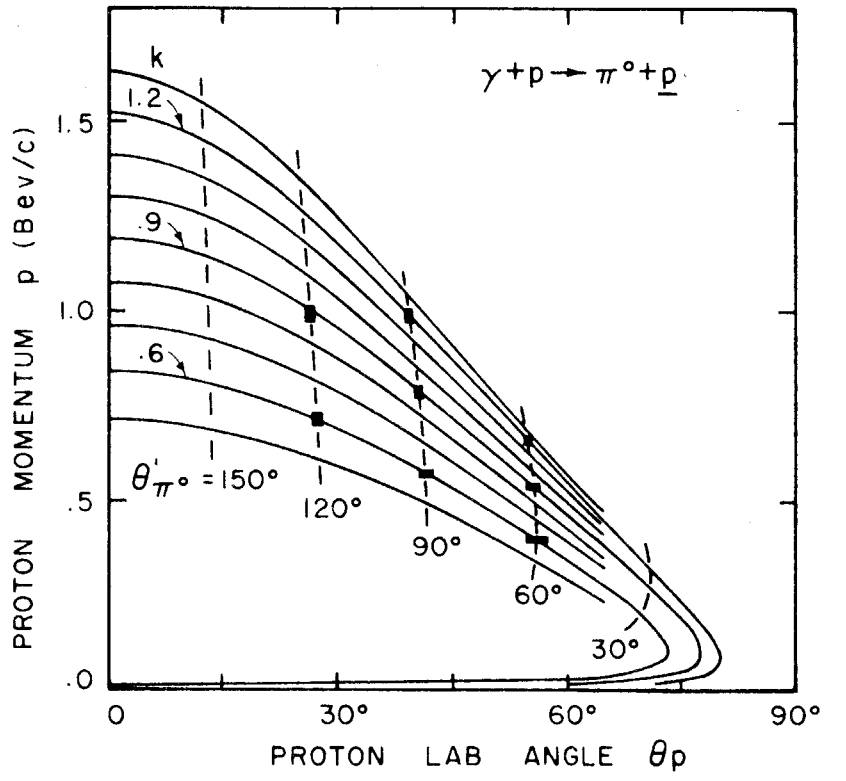

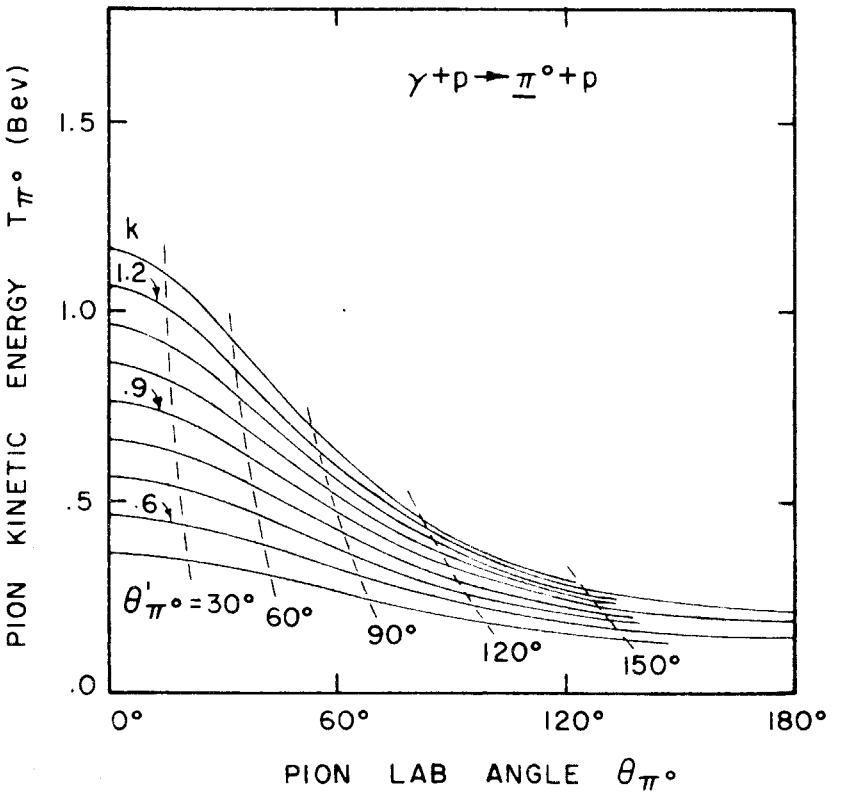

Single π^{o} Photoproduction Kinematics

Figure A10

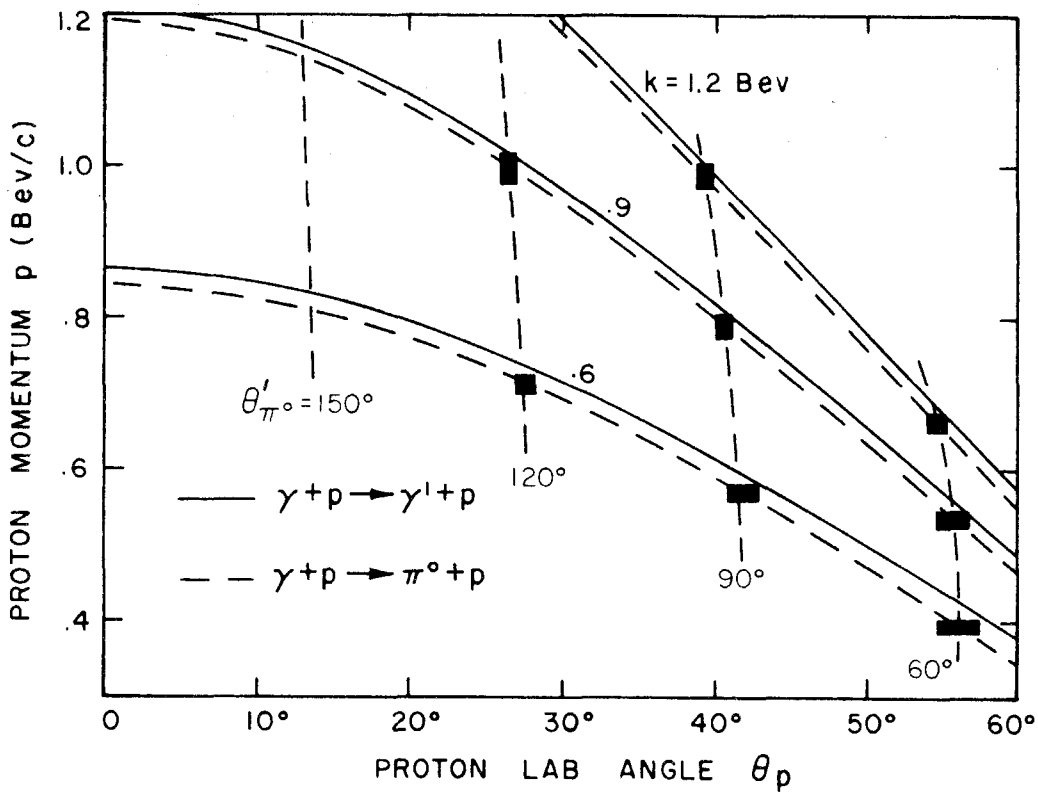

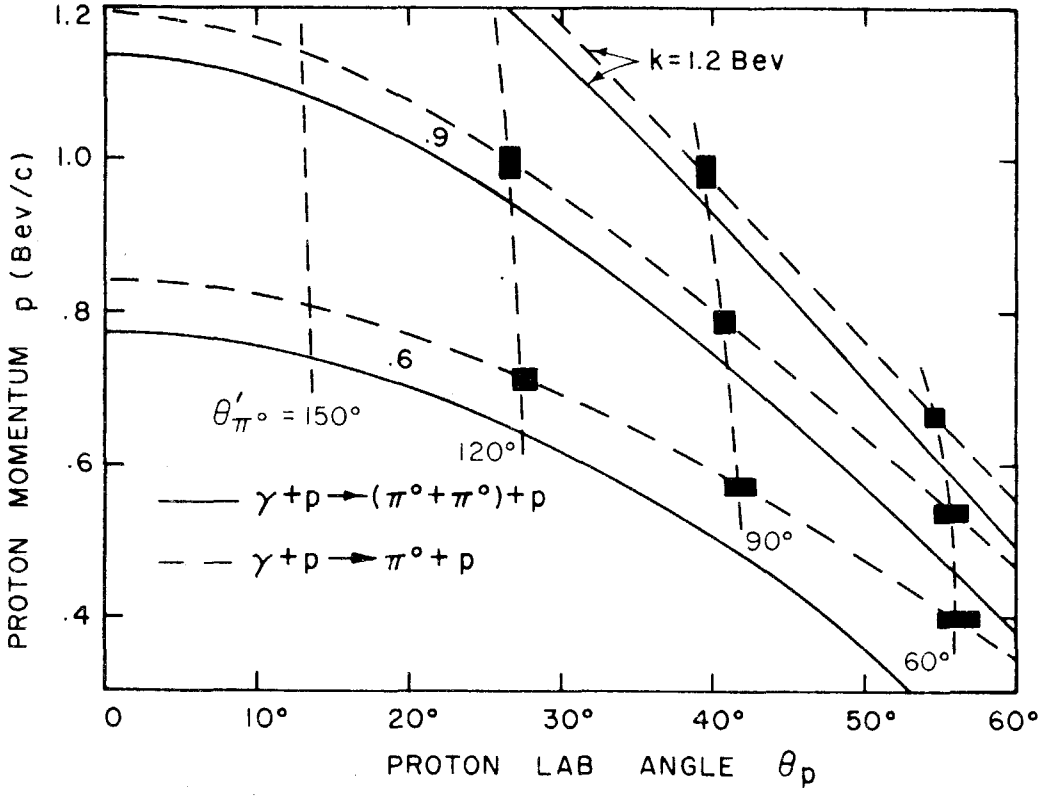

Contamination Kinematics

Figure A11

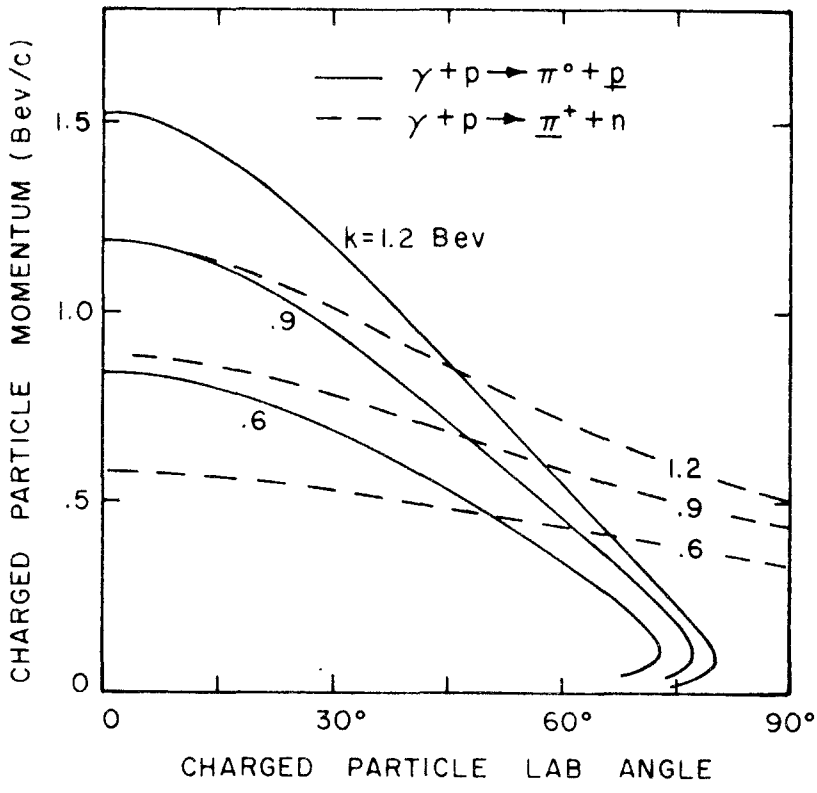

Comparison of Photoproduction Charged Particle Kinematics

Figure A12

APPENDIX XIII

Positions of the Total Cross Section Peaks

Virtual particle exchange terms, such as the pion pole term in π^+ photoproduction and the ω pole term in π^o photoproduction, contain both $I = 1/2$ and $3/2$ amplitudes and all angular momentum states. These terms can thus interfere with a resonance state, even producing interference effects in the total cross section. Because of this, the terms can shift the position of a resonant peak in the total cross section.

In order to study the effects of such terms we make the approximation that the resonances can be described by simple Breit-Wigner curves; i.e., the amplitude corresponding to the resonance describes a circle in the complex plane with radius r and center at $re^{i\frac{\pi}{2}}$ (see fig. A13):

$$A_o = r\sin\delta e^{i\delta} ,$$

$$\tan\delta = \frac{\Gamma/2}{W_r - W} .$$

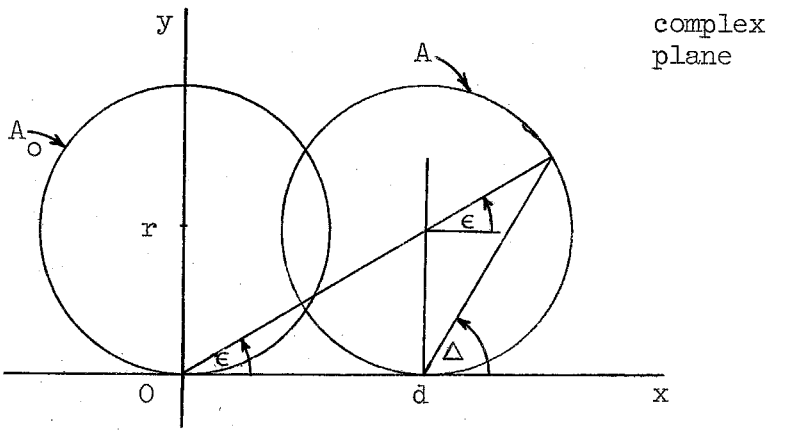

Figure A13

The addition of the exchange term shifts this amplitude horizontally (the exchange terms are real) by an amount depending on the amplitude for particle exchange to proceed with the quantum numbers of the resonance. We take this displacement to be d (positive to the right):

$$A = r\sin\delta\, e^{i\delta} + d \ .$$

The maximum of A occurs for

$$\tan \epsilon = \frac{r}{d} \ ,$$

corresponding to

$$\Delta = \frac{\pi}{4} + \frac{\epsilon}{2}$$

where ϵ and Δ are defined in Figure A13.

For small displacements we make the following approximation:

$$\Delta = \frac{\pi}{2} - \frac{d}{2r} \ ,$$

$$\tan \Delta = \frac{2r}{d} \ .$$

Under this approximation we obtain

$$W_r - W_{peak} = \frac{\Gamma d}{4r} \ .$$

Thus for small displacements the position of the peak shifts by an amount proportional to the displacement. As the displacement increases, W_{peak} asymptotically approaches $W_r \pm \Gamma/2$ (depending whether the displacement is to the left or right). If we assume the resonances to have the form described in Appendix X, then the resonant amplitudes no longer trace out

circles in the complex plane. For our purposes, however, we can consider the amplitude trajectories in the resonant energy regions to be circles with centers displaced from the imaginary axis.

This type of analysis has been carefully done by Wetherell (41) for the pion exchange term interfering with the first and second resonances. He assumed that π^o photoproduction is not affected by the pion exchange term and thus has peaks in the total cross section at the same energies as the pi-nucleon scattering peaks. That part of the π^+ amplitude with the resonant quantum numbers was taken to be the sum of two terms, the first proportional to the resonant scattering amplitude and the second being the component of the exchange term with the resonant quantum numbers. Using this model Wetherell obtained values for the energy shift of the π^+ photoproduction total cross section peaks which agree rather well with experiment.

Watson (42) has pointed out, however, that at low energies (below the threshold for pi pair production) a photoproduction element of the S-matrix can be shown on the basis of unitarity and time reversal to have the same phase as the pi-nucleon elastic scattering S-matrix element having the same set of quantum numbers (neglecting terms of order e^2). Thus in photoproduction it is the resonant term plus the contribution from the particle exchange term that has the scattering phase. If we consider the effects of the pion exchange term on a $I = 1/2$ resonance, then

$$M_o = -\sqrt{\frac{1}{3}}\,\rho e^{i\delta} + \sqrt{\frac{2}{3}}\,R_3$$

$$M_+ = \sqrt{\frac{2}{3}}\,\rho e^{i\delta} + \sqrt{\frac{1}{3}}\,R_3$$

where

M_o, M_+ are the matrix elements for photoproducing a π^o or π^+ with the j,l, and π (parity) of the resonant state,

$\rho e^{i\delta}$ is the total amplitude for photoproduction in an $I = 1/2$, j,l, and π state, and

R_3 is that part of the pion exchange term with $I = 3/2$, j,l and π.

An $I = 3/2$ resonance is treated in a similar manner. Note that both π^o and π^+ production are affected by the pion exchange term.* The position of the pi-nucleon cross section peak is predicted to be between those for π^+ and π^o photoproduction since the Clebsch-Gordon coefficients for both $I = 1/2$ and $3/2$ resonances are such that the exchange term enters with different relative signs in the two photoproduction amplitudes. The separation of the π^+ peak from the π^o peak calculated with this model is the same as predicted by the model of Wetherell (provided the linear approximations are valid).

---

*One may wonder why the pion exchange term should affect π^o production. When an analysis of the matrix elements is made in terms of states of definite angular momentum, isotopic spin, etc., as one does in constructing the S-matrix, the pion exchange term contributes to both the $I = 1/2$ and $3/2$ amplitudes. For π^o production the $I = 1/2$ contribution from the exchange term has the same magnitude as the $I = 3/2$ contribution, but with opposite sign; thus when the $1/2$ amplitude is added to the $3/2$ amplitude these contributions cancel and the pion exchange term does not contribute to π^o production. The Watson theorem gives the phase of the S-matrix photoproduction element with the resonant quantum numbers; this element includes that part of the pion exchange term having the resonant quantum numbers, including isotopic spin. The other isotopic spin contribution is left dangling, and it is this term which is shown explicitly above.

For the first resonance the Gell-Mann and Watson fit was used to give $\rho e^{i\delta}$; for the second and third resonances the Peierls fit was used to give the resonance widths and strengths. A program coded by J. Kilner was used to obtain the components of the virtual particle exchange terms (the ω coupling constants were obtained from R. Talman's analysis (2)). It was assumed for the calculation that the resonance states have the quantum numbers predicted by Peierls and the relative signs assumed in Section VC for the Peierls fit (chosen to give the π^o recoil proton polarization in the observed direction). The results, calculated by the linear approximation with Watson's theorem, are compared in Table 9 (Section VF) with the observed values. The energy differences between the π^+ and π^o photoproduction peaks calculated for the pion exchange term are in good agreement with the differences observed experimentally. The calculated energy differences between the π^o photoproduction peaks and the π^-p scattering peaks are considerably larger than those observed experimentally for the second and third resonances. Perhaps this is an effect of multiple pion production which was assumed to be negligible in the proof of Watson's theorem. The energy shift calculated for the ω exchange term is down an order of magnitude from that calculated for pion exchange and is in the opposite direction. Other terms, e.g., the Born nucleon pole terms may also be important, but since their role is not fully understood (in particular, they don't appear to be important in π^o photoproduction), the energy shifts caused by these terms were not calculated.

The good agreement obtained for the energy differences between the π^o and π^+ peaks is probably only fortuitous. Not only have we not

considered other terms such as the nucleon Born terms and the ρ exchange term, but we have assumed the peaks to be simple resonances, which in the case of the two higher resonances is quite dubious (36).

REFERENCES

1. J. H. Boyden, Ph.D. Thesis, California Institute of Technology (1961); R. L. Walker, Proc. 1960 High Energy Physics Conf. at Rochester, 17 (1960).

2. Talman, Clinesmith, Gomez, and Tollestrup, Phys. Rev. Letters 9, 177 (1962); R. M. Talman, Ph.D. Thesis, California Institute of Technology (1963).

3. McDonald, Peterson, and Corson, Phys. Rev. 107, 577 (1957); this article refers to earlier π^0 data.

4. R. L. Walker, Teasdale, Peterson, and Vette, Phys. Rev. 99, 210 (1955); this article refers to earlier π^+ data.

5. Lindenbaum, and Yuan, Phys. Rev. 100, 306 (1955).

6. Ashkin, Blaser, Feiner, and Stern, Phys. Rev. 101, 1149 (1956).

7. M. Gell-Mann and K. M. Watson, Ann. Rev. Nuclear Sci. 4, 219 (1954).

8. Chew, Goldberger, Low, and Nambu, Phys. Rev. 106, 1337 and 1345 (1957).

9. Brisson, Detoef, Falk-Vairant, van Rossum, Valladas, and L. C. L. Yuan, Phys. Rev. Letters 3, 561 (1959); Nuovo Cimento 19, 210 (1961).

10. Longo, Helland, Hess, Moyer, and Perez-Mendez, Phys. Rev. Letters 3, 568 (1959); Devlin, Barish, Hess, Perez-Mendez, and Solomon, Phys. Rev. Letters 4, 242 (1960); Devlin, Moyer, and Perez-Mendez, UCRL-9548 (1961).

11. J. I. Vette, Phys. Rev. 111, 622 (1958); Ph.D. Thesis, California Institute of Technology (1958).

12. DeWire, Jackson, and Littauer, Phys. Rev. 110, 1208 (1958); Phys. Rev. 119, 1381 (1960).

13. P. C. Stein and K. C. Rogers, Phys. Rev. 110, 1209 (1958).

14. R. M. Worlock, Phys. Rev. 117, 537 (1960).

15. K. Berkelman and J. A. Waggoner, Phys. Rev. 117, 1364 (1960); this article summarizes much of the earlier π^0 data.

16. G. Cortellessa and A. Reale, Nuovo Cimento 18, 1265 (1960); Sci. Repts. Ist. Super. Sanità 1, 73 (1961); Estratto dai Rendiconti dell'Istituto Superiore di Sanità 23, 1177 (1960).

17. Deutsch, Mencuccini, Querzoli, Salvini, Silvertrini, and Stiening, Proc. of the Aix-en-Provence Conf. 1, 9 (1961).

18. R. F. Peierls, Phys. Rev. 118, 325 (1960).

19. Maloy, Salandin, Manfredini, Peterson, Friedman, and Kendall, Phys. Rev. 122, 1338 (1961).

20. Peter Carruthers, Phys. Rev. Letters 4, 303 (1960).

21. M. Bloch and M. Sands, Phys. Rev. 113, 305 (1959).

22. Chasan, Cocconi, Cocconi, Schectman, and White, Phys. Rev. 119, 811 (1960).

23. J. H. Boyden, Private communication.

24. R. R. Wilson, Nuclear Instr. 1, 101 (1957).

25. P. L. Donoho, "A Magnetic Spectrometer for Analysis of Particles," California Institute of Technology (unpublished).

26. F. P. Dixon, Ph.D. Thesis, California Institute of Technology (1960).

27. C. Peck, Private communication.

28. Ruderman, Gomez, and Tollestrup, CTSL Report 31, California Institute of Technology (1962), unpublished.

29. Brody, Wetherell, and Walker, Phys. Rev. 119, 1710 (1960); H. M. Brody, Ph.D. Thesis, California Institute of Technology (1959).

30. Davies, Bethe, and Maximon, Phys. Rev. 93, 788 (1954).

31. DeWire, Feldman, Highland, and Littauer, Phys. Rev. 124, 909 (1961).

32. Cortellessa, Reale, and Salvadori, Estratto dai Rendiconti dell'Istituto Superiore di Sanità 23, 1177 (1960).

33. K. Berkelman, Istituto Superiore di Sanità Report ISS 61/13 (1961).

34. Feshbach, Peaslee, and Weisskopf, Phys. Rev. 71, 145 (1947).

35. Baum, Robinson, Criegee, and McKinley, Bull. Am. Ph. Soc. 7, 468 (1962).

36. Helland, Devlin, Hagge, Longo, Moyer, and Wood, Bull. Am. Ph. Soc. 7, 468 (1962); private communication from J. Helland.

37. Bruno Rossi, High Energy Particles, Prentice Hall, Englewood Cliffs, N. J., 54 (1952).

38. MacGregor, Moravcsik, and Stapp, Ann. Rev. Nuclear Sci. 10, 291 (1960).

39. H. G. de Carvalho, Phys. Rev. 96, 398 (1954).

40. R. P. Feynman, Theory of Fundamental Processes, W. A. Benjamin, New York, 73 (1961).

41. A. M. Wetherell, Phys. Rev. 115, 1722 (1959).

42. K. M. Watson, Phys. Rev. 95, 228 (1954).